FEMTOSECOND LASER NANOMACHINING AND APPLICATIONS TO MICRO/NANOFLUIDICS FOR SINGLE CELL ANALYSIS

by

Sanghyun Lee

A dissertation submitted in partial fulfillment
of the requirements for the degree of
Doctor of Philosophy
(Mechanical Engineering)
in The University of Michigan
2008

Doctoral Committee:

Associate Professor Alan J. Hunt, Co-Chair
Associate Professor Edgar Meyhöfer, Co-Chair
Professor Steven L. Ceccio
Associate Professor Joseph L. Bull

ACKNOWLEDGEMENTS

I really appreciate the scholastic guidance and support of my research adviser, Professor Alan J. Hunt. I have worked for him as a GSRA since becoming involved with the femtosecond laser nanomachining project. Prof. Hunt was actually my co-adviser when I began working on the project, and became my primary adviser after my first adviser, Dr. E. F. Hasselbrink, left our department. Prof. Hunt is logically strict yet generous in taking care of his students, which has no doubt allowed me to remain focused on my research, leading me to the best results. Throughout the years I have learned his scholastic manner, which has no doubt helped me solve mysterious phenomena I have encountered in my research. I appreciate everything he has done for me.

In 2004 I was developing a thermal modulator – a core component in 2-dimensional gas chromatography (2DGC) that connects two orthogonal separation mechanisms. However my previous adviser, Dr. Hasselbrink, thought that the 2DGC project was just a summer project and I needed another project for my Ph.D. dissertation. I appreciate Dr. Hasselbrink for getting me started on this research.

Professor Edgar Meyhöfer, who is my one of two chair examiners, also helped me with his keen scholastic eyesight. I appreciate him for all of his guidance and advice.

I thank IMRA and Intralase Corp. for use of their lasers. This work was supported by a grant from IMRA Corp. and NIH R21 EB006098-01.

TABLE OF CONTENTS

LIST OF FIGURES

LIST OF TABLES

LIST OF APPENDICES

LIST OF ABBREVIATIONS

AAGR	Average annual growth rate
AR	Aspect ratio (=length/diameter)
BERA	Bioelectric recognition assays
CCDB	**C**urrent controlled dielectric breakdown
CE	Capillary electrophoresis
CGC	Capillary gas chromatography
CGE	Capillary gel electrophoresis
CIEF	Capillary isoelectric focusing
CIPT	Capillary isotachophoresis
CPA	Chirped pulse amplification
CZE	Capillary zone electrophoresis
DEP	Dielectrophoresis
DNA	Deoxyribonucleic acid
EK	Electrokinetic (e.g., EK pump)
EKC	Electrokinetic chromatography
ELISA	Enzyme-linked immunosorbent assay
EOF	Electroosmotic flow
EWOD	Electrowetting-on-dielectric
fl	Femtoliter (=10^{-15}l)
fs	Femtosecond (=10^{-15}s)
HCS	High-content screening
HPLC	High performance liquid chromatography
HTS	High-throughput screening
ICF	Inertial confinement fusion
IEF	Isoelectric focusing
ITP	Isotachophoresis

KTP	Potassium titanyl phosphate
LIC	Lab in a cell
LOC	Lab on a chip
MECC	Micellar electrokinetic capillary chromatography
MEKC	Micellar electrokinetic chromatography
MIME	Molecular identification through membrane engineering
MPI	Multi-photon ionization
MSSL	Multiple scanning of straight line
NCL	Normalized capillary length (=length/diameter)
OCI	Optics in critical intensity
PDF	Pressure driven flow
PDMS	Polydimethylsiloxane
pI	Isoelectric point
PRR	Pulse repetition rate
RNA	Ribonucleic acid
SEM	Scanning electron microscopy
SOC	System-on-chip
SSSL	Single scanning of straight line
TEC	Thermo-electric cooler
WGW	Water-Gas-Water
μTAS	Micro Total Analysis Systems

CHAPTER I

INTRODUCTION

1. Microfluidics technologies

Since microfluidics emerged in the 1990s, the technology has rapidly expanded into intrinsic multidisciplinary interests intersecting fluid dynamics, physics, chemistry, biology and micro-technology. Microfluidic investigations, which have traditionally focused on developing isolated modules, are now transitioning toward integration of these isolated modules into more complex stand-alone systems known as lab-on-a-chip (LOC), micro-total-analysis-systems (μTAS), or system-on-chip (SOC). These integrated systems are not only supposed to be reliable, but also reconfigurable and scalable. Recent developments in dielectrophoresis (DEP) and electrowetting-on-dielectric (EWOD) devices [1-5] are paving the way toward droplet-based digital microfluidics, which will likely accelerate system integration with highly reconfigurable and scalable characteristics [6].

These recent innovations reflect the fast growing market for microfluidic technologies. At an average annual growth rate (AAGR) of 14.1%, the global market for microfluidic technologies is expected to grow into a 6 billion-dollar industry over the next five years. Inkjet printing, which is the slowest-growing application, is by far the largest current application of microfluidics, accounting for nearly three-quarters of the total market. However, the markets for drug-discovery, point-of-care applications, and high-throughput screening, which are the fastest-growing applications, are expected to surpass over 40% of the market, whereas the inkjet printing segment is expected to reduce to about 50% of the market by 2011. The market for proteomics, genomics, and chemical analysis and synthesis is also expected to grow fast, contributing to the high AAGR of microfluidics [7-9].

On-chip full system integration will ultimately require 3-dimensional configurations and downscaling to the nanoscale regime for high-density complex

geometries. Also, for more complete integration, configuring hybrid systems based on continuous-flow microfluidics and digital microfluidics will be another important issue facing microfluidic development. Mixing and transport by droplet-based digital microfluidics can maximize reconfigurability and scalability of the system, but separations based on continuous-flow microfluidics should be integrated into the system to realize the two major functions of stand-alone systems: mixing and separation.

Fabrication techniques based on lithography-etch-bond processes are by far the most widely used methods in microfluidics technologies and are very advantageous in mass production of 2-dimensional, microscale configurations. However, lithography-based technologies struggle to achieve 3-dimensional configurations, nanoscale geometries, and integration of continuous-flow and digital microfluidic modules into a system.

Therefore, a complementary fabrication tool for 3-dimensional configurations and nanoscale fabrication is increasingly requested for microfluidics to achieve the ultimate integration tasks for system development. Optical machining based on femtosecond laser pulses is quickly emerging as the most promising fabrication tool.

2. Optical machining by femtosecond laser pulses

2.1. Characteristics of femtosecond lasers

A femtosecond laser is an ultrafast laser emitting optical pulses with a duration well below one picosecond (with 1ps = 10^{-12}s), i.e. in the domain of femtoseconds (with 1fs = 10^{-15}s). The generation of such short pulses is achieved with the technique of mode locking [10-12]. Methods for producing mode-locking in a laser may be classified as either an active method [13] using an external signal to induce modulation of the intra-cavity light, or a passive method [14, 15] using self-modulation of the light via saturable absorbers.

Pulse durations less than approximately 100fs are too short to be directly measured using optoelectronic techniques (i.e. photodiodes), and so indirect methods such as autocorrelation, frequency-resolved optical gating [16], spectral phase interferometry for direct electric field reconstruction [17], or multi-photon intra-pulse interference phase scan [18] are used.

According to the mode-locking theory, the duration of the pulses is mainly determined by the gain medium (gain bandwidth) of the laser and the size of the cavity (frequency separation). For example, a titanium-doped sapphire (Ti:Sapphire) solid-state laser, which has 128THz gain bandwidth, can have about 4fs theoretical minimum pulse duration in a 30cm cavity, whereas a typical helium-neon (HeNe) gas laser, which has 1.5GHz gain bandwidth, can have about 300ps pulse duration in the same cavity. So, selecting the proper laser medium is most critical.

Passively mode-locked solid state bulk lasers can emit high quality ultrashort pulses with typical durations between 30fs and 30ps; Ti:Sapphire lasers are even suitable for pulse durations below 10fs. Various diode-pumped lasers, e.g. based on neodymium-doped or ytterbium-doped gain media, operate in this regime, with typical average output powers between about 100mW and 1W. The pulse repetition rate (PRR) is in most cases between 50 MHz and 500 MHz, although there are low repetition rate versions with a few megahertz to a few kilohertz for higher pulse energies, and also miniature lasers with a PRR on the order of tens of gigahertz.

2.2. Application fields of femtosecond lasers

The application fields of femtosecond lasers can be classified in four segments: femtochemistry, nuclear fusion (inertial confinement fusion: ICF), nonlinear optics, and femtosecond laser machining. While Rudolph A. Marcus (Nobel Laureate in Chemistry, 1992) had contributed to the theory of electron transfer reactions in chemical systems, Ahmed H. Zewail (Nobel Laureate in Chemistry, 1999) solidified femtochemistry using femtosecond spectroscopy and took the 1999 Nobel Prize in Chemistry for showing that, using rapid laser techniques, it is possible to see how atoms in a molecule move during a chemical reaction. In femtosecond spectroscopy, an ultrafast laser injects two pulses; the first is a powerful pump pulse that strikes the molecule and excites it to a higher energy state, and the second is a weaker probe pulse allowing the detection of short-lived intermediate molecules. This method is also particularly useful in biochemistry, where it is used to analyze details of protein folding and function.

In the field of nuclear fusion, the ignition laser was one of the most important developments for utilizing the ICF for electric power sources. With ultrahigh-power laser sources, the fuel pallet in an ICF system experiences compression and heating, which completes the ignition process. Femtosecond lasers are the key feature in the newly developed fast ignition technology, which intends to decouple the compression and heating phases for the implosion. Femtosecond lasers complete the heating process, whereas compression is performed via conventional high power lasers. If successful, the fast ignition approach could dramatically lower the total amount of energy needed to be delivered to the target, yet the predicted fusion gains are nevertheless even higher than the previous single phase technology. Also, femtosecond lasers are used in nonlinear optics, such as second-harmonic generation, parametric down-conversion, optical parametric oscillators, and generation of terahertz radiation.

Most importantly, femtosecond lasers have huge potential in the field of micro/nanomachining. The ultrashort laser pulse properties achieve an unprecedented degree of control in sculpting the desired micro/nanostructures internal to the materials without collateral damage to the surroundings. When laser energy is deposited at a time scale much shorter than both the heat transport (micro- to nanoseconds) and the electron-phonon coupling (nano- to picoseconds), the light-matter interaction process is essentially

frozen in time, minimizing collateral damage to the surroundings. Also, because the machining process is not dependent on the linear absorption at the laser wavelength, virtually any dielectrics, metals, and mechanically hard materials can be machined by the same laser beam.

The strong dependence of the optically-induced dielectric breakdown on the pulse duration has been studied by the Bloembergen group. They found that for laser-pulse durations down to 10ps, the damage-threshold fluence scales with $T^{1/2}$, where T is the pulse duration [19]. They also proposed the avalanche ionization theory with multiphoton ionization (MPI) electron seeding mechanism.

Thereafter, more precise experiments for the influence of the pulse duration on the damage threshold for advanced femtosecond laser systems found that the damage threshold shifts from stochastic to deterministic [20] and the shot-to-shot variability is strongly attenuated. Therefore precise, deterministic, and reproducible optical machining is achieved [21, 22].

2.3. Distinguishable features of femtosecond laser machining

When a transparent material is machined by femtosecond laser pulses, a true 3-dimensional configuration is achieved. Recently, there has been significant progress in fabricating 3-dimensional subsurface geometries in glass using optical ablation by femtosecond laser pulses [21-31]. Unlike conventional lithography-etch-bond processes and nanoscale fabrication techniques such as nanoimprint lithography [32], optical machining is a 3-dimensional process, which eliminates the need to stack and bond layers to form 3-dimensional structures. Moreover, tightly focused femtosecond laser pulses achieve far-field nanoablations [21, 22], and water-assisted femtosecond laser nanomachining achieves 3-dimensional fabrication of surface and subsurface nanoscale features outside of a cleanroom [29-31]. Therefore femtosecond laser machining can be very easily combined with conventional lithography-etch-bond processes.

It is also advantageous that glass can be used as a target material. Glass is the standard for a wide variety of analytical applications due to its relative inertness, ability to withstand high pressures and organic solvents, hydrophilicity, low adsorption, and long history of well-characterized surface derivatization chemistries. However, due to the

considerable difficulty associated with producing multilayer all-glass microdevices with reasonable device yield, soft lithography using polydimethylsiloxane (PDMS) and other polymeric materials [33] has been widely adapted as a substrate for the microfluidic device. Unfortunately the limitations of PDMS (limited solvent resistance, leaching, protein adsorption, inability to contain high pressures) still prevent adaptation to a variety of desirable analytical applications.

The ability to configure 3-dimensional features from the micron- to submicron-scale has huge potential to impact many fields, including micro/nanofluidics, pharmaceuticals, chemical engineering and biotechnologies. In these fields, manipulating submicroliter volume fluids is of great importance for analyses of chemicals, proteins, peptides, polysaccharides, DNA, and cells.

Many micro/nanofluidic modules that have been very difficult to fabricate based on the lithography format can now be fabricated and integrated into mass-producible single layer microfluidic formats. Pre-etched single layer glass substrates can be reconfigured into 3-dimensional devices by simply connecting them with jumpers or with 3-dimensional modules. 3-dimensional micro/nanofluidic modules, such as submicron-scale separation columns, fast diffusion mixers, surface tension valves, nano-sensors, and electrokinetic pumps can be developed based on fs-laser machining technology.

The ability to reconfigure 2-dimensional single layer formats into 3-dimensional complex devices can be best exploited in the development of microscale assays. Most assay formats currently used the medical and pharmaceutical fields are too complex to realize with 2-dimensional single layer formats. Thus, fs-laser-machining combined with current lithography technologies is highly expected to realize the complex micro-assay technologies.

Surface nanomachining, whose feature sizes reduce to smaller than 100nm [21, 22], can be applied to various applications such as nanoimprint mold fabrication. Additionally, because there are almost no material restrictions, very strong and long-lasting molds can be rapidly prototyped at a reasonable price.

Submicron-scale subsurface feature sizes [29-31] have especially huge potential in biotechnologies. Compared with the average cell size and volume (10μm and 1pl), 3-dimensional submicron-scale capillaries can impact almost every technology in single

cell analysis and lab-in-a-cell (LIC) technologies: 1) cell characterization: electrical (patch clamping, electrical resistance measurements), mechanical (external pressure vs. changes of ion channels and signaling molecules), and biochemical (intracellular sensing); 2) internal and external cell communication: electroporation and nanoneedle; 3) liquid control: submicron-scale electrokinetic (EK) pump; 4) cell manipulation, isolation and immobilization: surface tension valve; and 5) single cell proteomics: nanocapillary electrophoresis (nCE).

3. A gallery of features made with femtosecond optical nanomachining

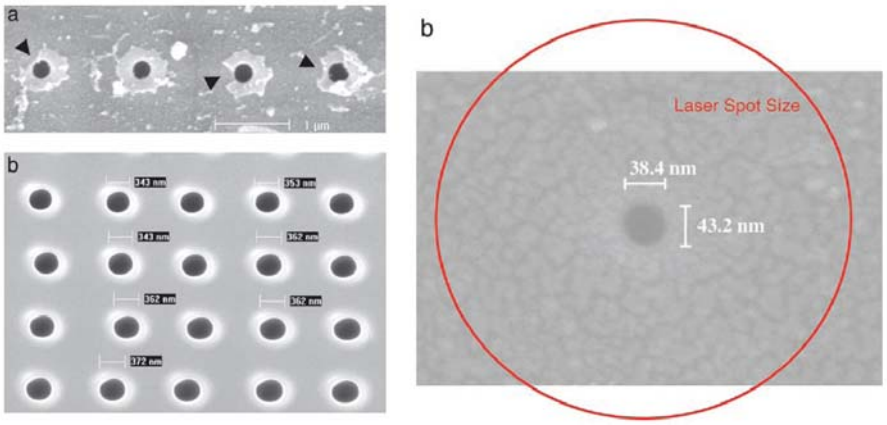

Fig. I. 1. Surface nanofeatures; when tightly focused fs laser pulses are operated at the OCI (optics at critical intensity) regime, far field nanomachining can be achieved with great reproducibility and precision down to about 40nm of the surface feature size [21].

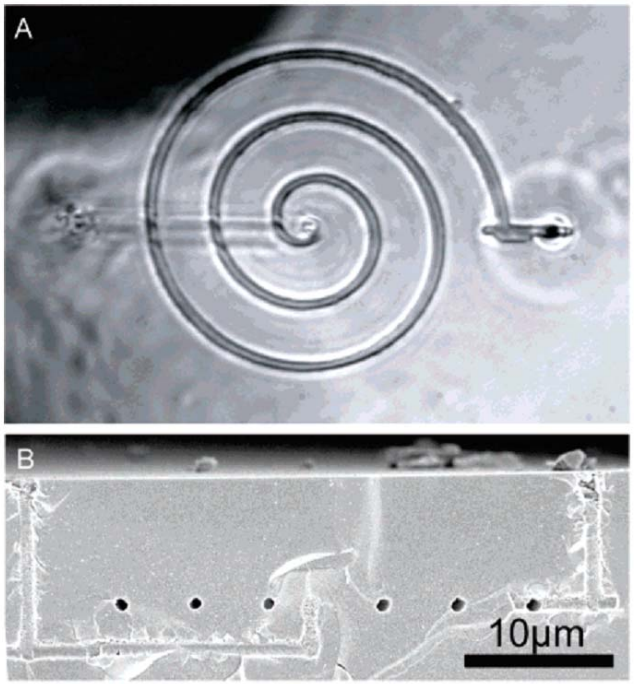

Fig. I. 2. Spiral channel in glass; subsurface fs-laser-machining configures 3-dimensional subsurface features without any limitation, which has huge potential in developing 3-dimensional micro/nanofluidic units and configurations that have been impossible to achieve with current planar lithography-based fabrication processes [29].

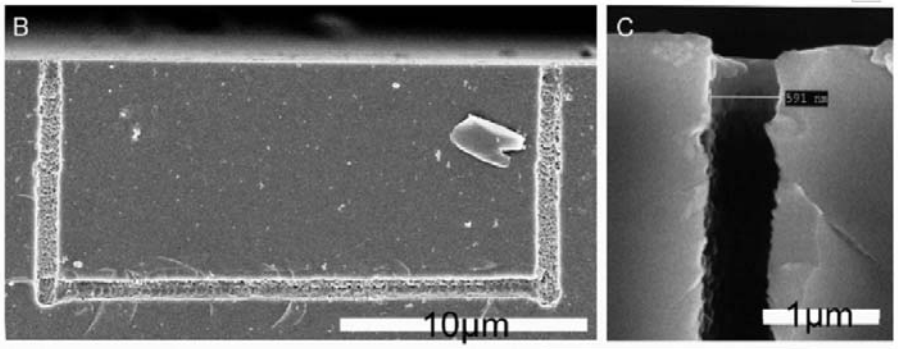

Fig. I. 3. Jumper channel; fs-laser-machining can be easily combined with current planar lithography-based microfluidic fabrication processes, achieving the reconfiguration of 2-dimensional single layer planar formats to 3-dimensional complex formats. Jumper channel is the basic and core unit to connect 2-dimensional channels in 3-dimensional ways, simplifying the device layouts and preventing any unwanted channel crossings [29].

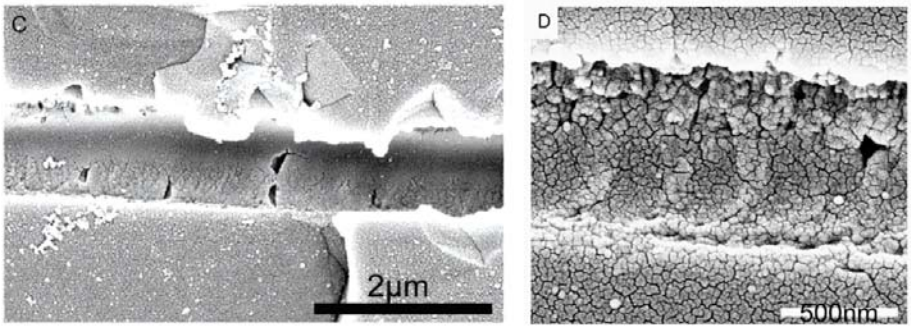

Fig. I. 4. Surface roughness; the roughness of the fs laser nanomachined surfaces is in general very smooth. Compared with the submicron-scale bore size, the surface roughness is less than 10% [29].

CHAPTER II

EXPERIMENTAL CHARACTERIZATION OF GLASS NANOMACHINING

1. Introduction

The light-matter interaction based on non-linear optical interaction is the major ablation mechanism by which fs-laser-machining causes permanent damage to the target material. This process primarily depends on several laser parameters, such as pulse duration, pulse energy, and pulse repetition rate (PRR), and control parameters such as feed-rates (machining speed). Secondary parameters are more diverse and tend to be case-dependent, yet affect the machining efficiency, effectiveness, and quality as much as the primary parameters; for example, the presence of water includes hydrodynamic and interfacial parameters such as pressure, temperature, surface tension, and the composition of gases dissolved in water (affecting acoustic transmission, refer to chapter III).

To compare machining ability in parametric ways, two fundamental concepts are defined: the machining efficiency and the effectiveness. Machining efficiency measures the actual subtraction volume per pulse in comparison with the ideally achievable maximum. Thus, the machining efficiency is defined as the actual subtraction volume per pulse divided by the effective volume of laser focused where ablation occurs. This dimensionless parameter measures subtraction efficiency based on energy input. Machining effectiveness, on the other hand, considers "machining-rate", measuring the subtraction volume per unit time [m^3/s]. The effectiveness will increase with increased power input. However, although the actual and the maximum subtraction volume can be all increased, the efficiency doesn't necessarily increase with increased power input.

The machining performance of surface features can be simply related to machining parameters. However, those of subsurface geometries, such as capillaries and channels, fail to find any simple relationships with machining parameters. The secondary parameters arising especially from the presence of water cause more complicated

relationships between the primary parameters and machining performance.

Among the laser parameters, the PRR shows the most unpredictable results; higher power input via higher PRR decrease machining effectiveness. This is because the water-assisted machining can suffer from consequent dehydration of the ablation site, which can dramatically decrease machining performance.

These complicated relationships among the primary and the secondary parameters should be understood quantitatively to maximize machining performance. In addition, a physical model for the dehydration problem helps find other possible strategies to further optimize material properties, such as surface tension of water and surface roughness of the machined capillary.

In chapter II, with detailed description of overall experiments performed in this dissertation, parametric studies find the effects of primary parameters on machining performance based on two different methods of ‘single scanning of a straight lines’ (SSSL) and ‘multiple scanning of a straight lines’ (MSSL).

The secondary parameters due to the presence of water, such as pressure, temperature, and gas composition of the nano-bubble, are further discussed in chapter III through theoretical and experimental approaches.

2. Parametric studies

2.1. Mechanism of debris extrusion process

Similar to mechanical drilling methods using physical drill bits, optical machining also requires favorable debris extrusion so as to continue drilling as deep as possible. Mechanical drilling methods use spiral grooves at the side walls of drill bits to extrude debris as the drilling progresses deep into the material.

Optical laser machining, which has no mechanical contact with the material, can suffer from debris accumulation, resulting in early termination of machining. This problem has been substantially improved by introducing liquids which wash out the machining debris through the circulation driven by bubble expansion. Since liquid assisted optical machining was addressed several years ago, diverse liquids have been tested to assist machining and water has been proved to be a very effective liquid in debris extrusion.

With the presence of water, a hydrodynamic process, the water circulation becomes important; bubble expansion drives the water circulation, extruding the machining debris out of the channel.

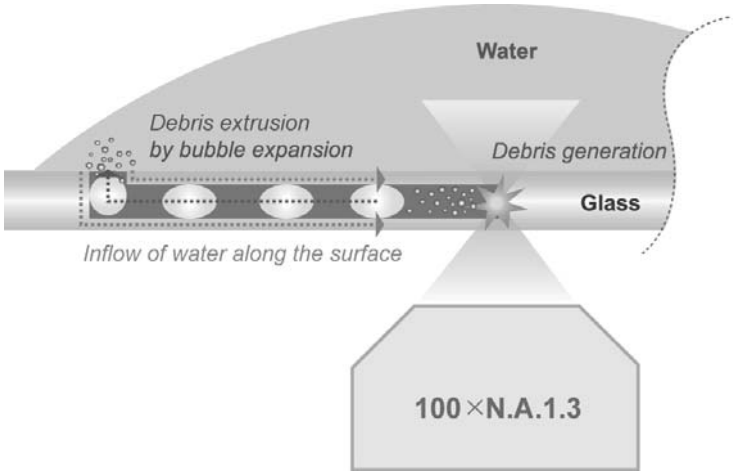

Fig. II. 1. Inflow of water along the channel and outflow by bubble expansion constitute channel circulation; refer to the appendix 1 for the detailed experimental setup

As shown in Fig. II. 1, the debris extrusion process basically relies on water which entrains machining debris at the ablation site and is extruded out of the channel

through the water circulation driven by the bubble expansion. While the bubble expansion extrudes water entraining machining debris out of the channel, strong capillary force of nanocapillaries continuously draws clean water deep into the ablation site. Thus, these two hydrodynamic forces constitute the water circulation along the nanocapillary during machining.

Sound water circulation during machining is a key to promoting the debris extrusion process. In order to maintain sound water circulation the two hydrodynamic forces should be well-balanced. While capillary force is not practically controllable, bubble generation and expansion are closely related to the laser power input. Thus, appropriate laser pulse controls in terms of pulse energy and PRR should be parametrically elucidated.

A relation for the debris extrusion rate, $\dot{\gamma}$ [kg/s], can be established as equation (1); the debris extrusion rate is determined by the water circulation, Q [m^3/s], which is proportional to pressure difference (ΔP: by bubble expansion) [N/m^2] divided by the resistance to the circulation (R_{cir} [Ns/m^5]).

$$\dot{\gamma} \propto Q = \frac{\Delta P}{R_{cir}} \tag{1}$$

Theoretical approaches to evaluate these parameters are practically limited due to the phenomenal complexity. Thus, experimental data based on parametric studies should be established to understand the water circulation processes and to finely tune the laser machining parameters for sound debris extrusion.

2.2. Laser back-scanning for effective debris extrusion in long channel machining

Better water circulation can be promoted through laser focus motion controls, such as laser back-scanning. When the overall length of the channel is relatively short, the bubble expansion at the ablation site (dead end of the channel) can fully circulate the water through the entire channel. However, as the channel length increases, water circulation becomes increasingly difficult, slowing down the debris extrusion rate. So, especially for long channel machining, periodic full back-scanning of the focused laser along the machined channel performs residual debris extrusion; thus, sound water circulation can be restored.

Phenomenally, the laser back-scanning seems to physically push the water plug in front of the laser focus. As shown in Fig. II. 2, the water plug in front of the laser focus is actually pushed by the laser focus out of the channel. This optical pushing mechanism is thought to be based on the pressure that is generated when the thin water film on the wall is vaporized by the laser focus. When the laser focus directly contacts the water plug, instantaneous pressure will build up, further pushing the water plug. Thus, the water plug in front of the laser focus can be optically pushed.

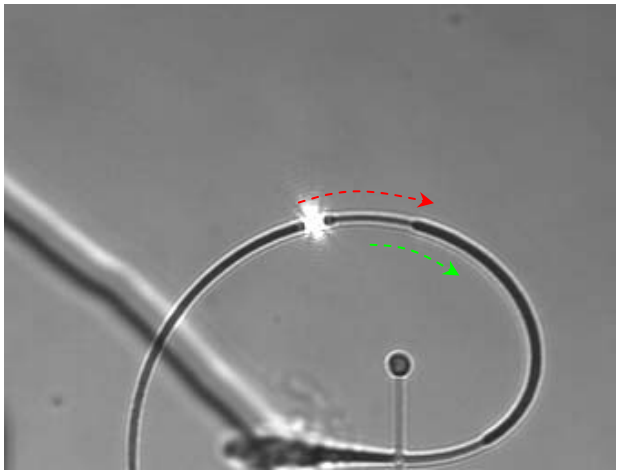

Fig. II. 2. Laser back-scanning pushing water plug out of the channel

This laser back-scanning is very effective to sweep out the residual debris, which is very difficult to extrude only by the bubble expansion at the ablation site. And periodical full back-scanning of the focused laser significantly improves water circulation; otherwise the machining will terminate earlier.

A well-established machining process based on periodic full back-scanning, repetitive local-scanning, and adaptive feed-rate control can maintain very sound machining until the first acoustic node emerges.

2.3. Test geometry for parametric studies

In order to perform parametric research, simple and fundamental test geometry should first be defined. In this dissertation, a rectilinear capillary is chosen for the test geometry, which should be the simplest and the most fundamental geometry. To initiate these test geometries, relatively larger cylinders having 5μm diameters are machined first,

where one cylinder initiates two rectilinear capillaries as shown in Fig. II. 3. Thus, one test set having 10 cylinders can test 20 capillaries. In the parametric research, each cylinder was assigned different feed-rates from 5 to 50μm/s, with 10 different feed-rates tested in each test set.

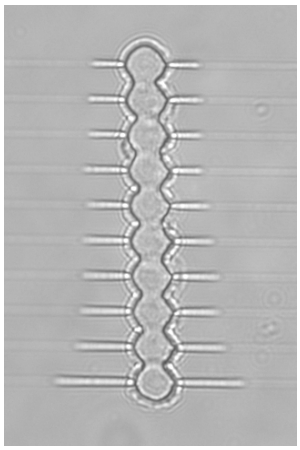

Fig. II. 3. One set of test geometry for parametric performance measure

The measurements of machining performance are performed based on this test geometry through two different machining patterns.

The first pattern is single scanning of a straight line (SSSL), which scans a sole straight line from the center cylinder towards the outside direction until the machining terminates. The other pattern is multiple scanning of a straight line (MSSL), which applies SSSL multiple times until target length of a straight capillary is achieved.

The decision of the valid length of capillaries relies on the optically acquired intensity levels. As shown in Fig. II. 3 the valid length of the machining capillary can be determined from graphical information. In this dissertation, the mean intensity level of the capillary is used to determine the spatial interface location between glass and capillary.

2.4. Calculation of machining efficiency and effectiveness

The machining efficiency can be calculated by two steps; first, the total subtraction volume is divided by the total number of pulses which is the actual subtraction volume per pulse. This value is then divided by the effective volume of laser focus where optical ablation occurs, which is the maximum subtraction volume of one pulse. The final unit of machining efficiency is dimensionless.

Calculating the machining effectiveness is done in two steps. First, the total subtraction volume is measured, and then divided by the machining time. As shown in the dimension, the machining effectiveness is the volume subtraction rate [$\mu m^3/s$].

In addition, another definition assessing the machining effectiveness of a subsurface long capillary can be defined by the maximum normalized capillary length (NCL=length/diameter; also called aspect ratio, AR). The direct optical machining of a subsurface capillary is intrinsically limited in increasing NCL because debris extrusion becomes increasingly difficult as it goes deeper and deeper. So, the NCL is another dimensionless parameter used in measuring the machining effectiveness of long subsurface capillaries. The NCL is studied in detail in chapter III.

3. Results of performance measurements

3.1. Effect of pulse energy: SSSL method

As shown in Fig. II. 4, the machining performance (measured as machined length) increases nearly proportionally with pulse energy. However, because higher pulse energy creates larger channel diameters, the channels NCL does not considerably increase thereby reducing improvements in the machining effectiveness.

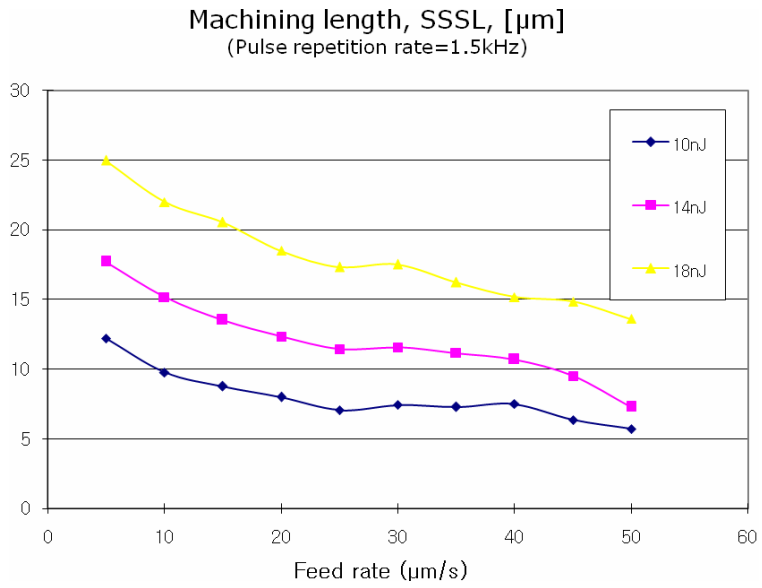

Fig. II. 4. Machining length vs. pulse energy

The machining efficiency and effectiveness based on pulse energy are separately illustrated in Fig. II. 5 and Fig. II. 6. As expected, increasing pulse energy clearly improves machining efficiency and effectiveness. Compared with the PRR and feed-rate, the pulse energy is limited to control, giving less freedom to optimize the machining performances with pulse energies. In addition, the feature size and surface condition also change according to the pulse energy, further limiting this parameter.

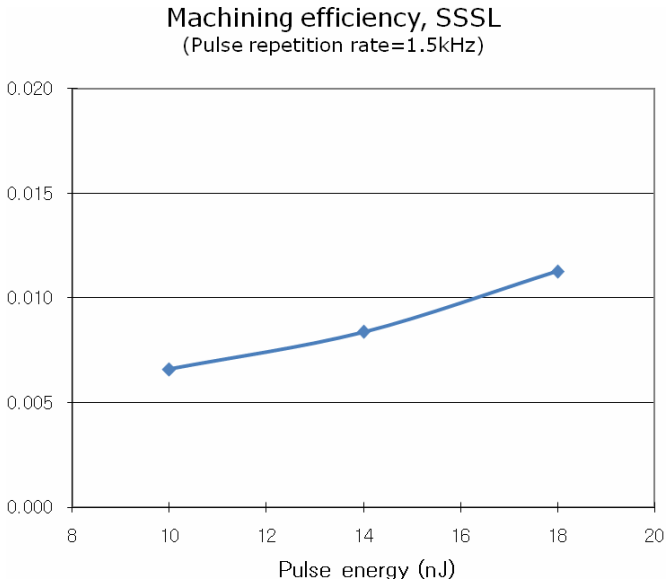

Fig. II. 5. Machining efficiency vs. pulse energy

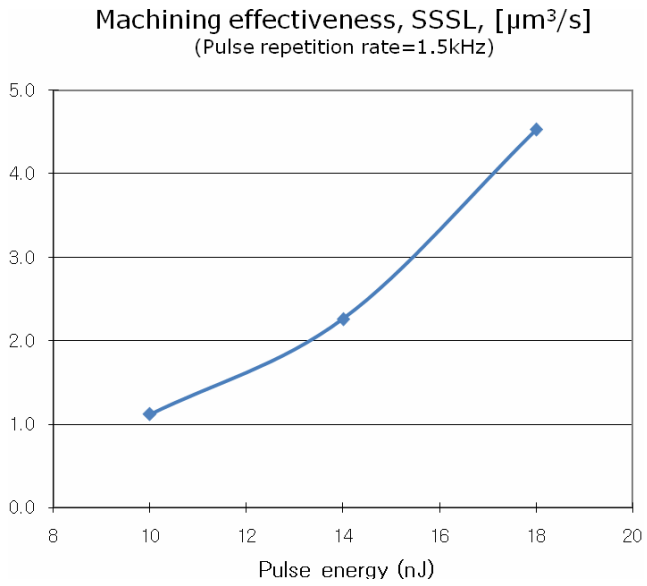

Fig. II. 6. Machining effectiveness vs. pulse energy

3.2. Effect of PRR: SSSL method

The femtosecond laser system used in this dissertation can continuously vary PRR by 1Hz steps from 500Hz to 3kHz (refer to the appendix 1). Because the pulse energy is fixed as 14nJ/pulse, the input power is proportional to the PRR.

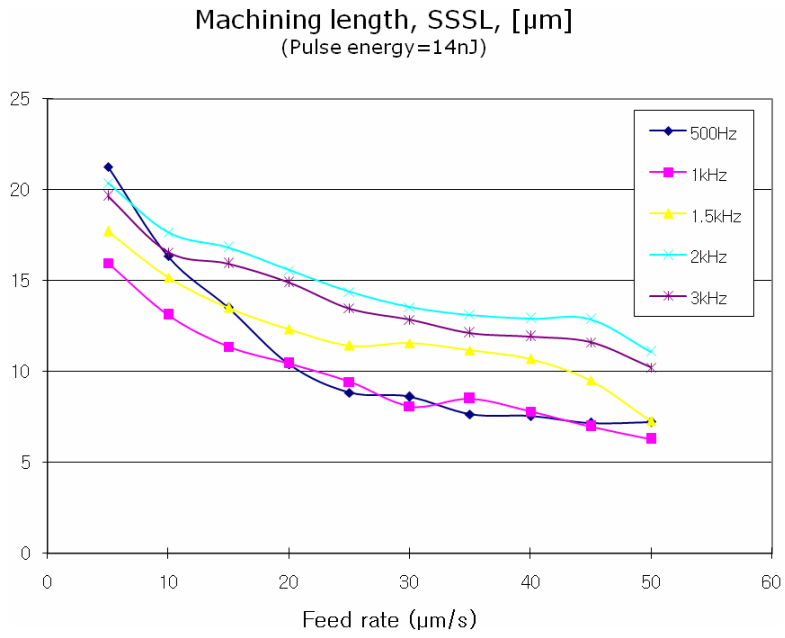

Fig. II. 7. Achievable machining lengths vs. feed-rate and PRR

Fig. II. 7 shows the results of measured capillary lengths machined with varying feed-rates and PRR. One strange but obvious finding is that machining with 500Hz PRR and 5μm/s feed-rate yields the longest capillary. Although the deviation becomes settled down as the feed-rate increases, any clear advantages of higher PRR are still not found.

The analyses based on machining efficiency and effectiveness clearly show that higher PRR does not contribute to improved machining performance, as shown in Fig. II. 8 and Fig. II. 9.

Fig. II. 8 clearly shows that machining efficiency decreases as the PRR increases. This means that lowering PRR increases the machining efficiency, whereas improved machining effectiveness generally requires higher power input. Considering that machining effectiveness is in general more important than the machining efficiency to improve the gross machining performance, maximizing the machining effectiveness is the first goal in the parametric studies. Therefore, the 2kHz PRR maximizing machining effectiveness becomes more important than the 500Hz PRR maximizing machining efficiency.

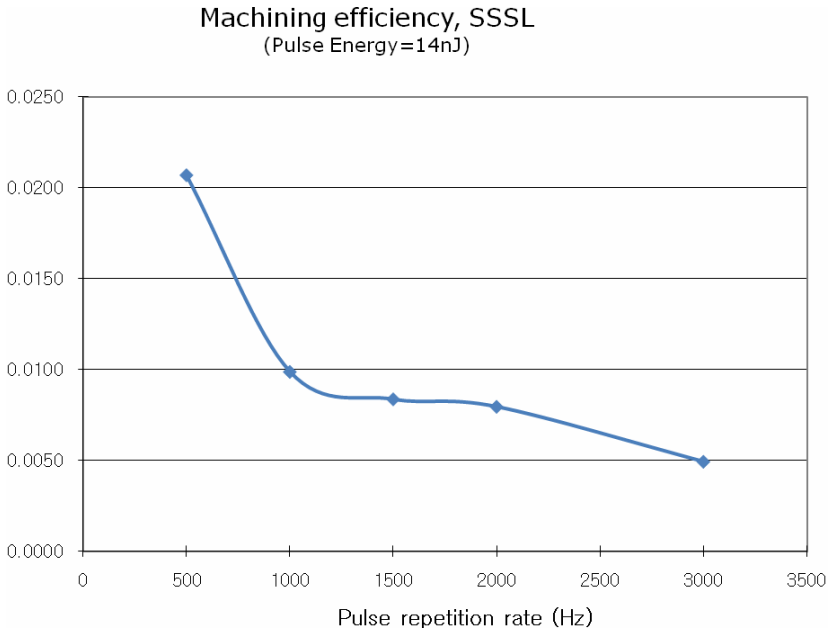

Fig. II. 8. Average machining efficiency vs. PRR

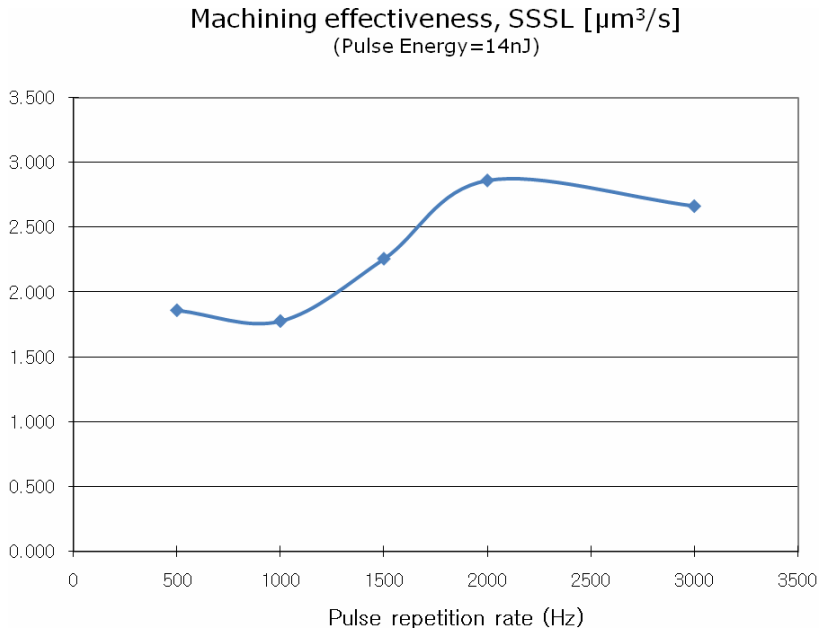

Fig. II. 9. Average machining effectiveness vs. PRR

The machining effectiveness generally increases with PRR until PRR = 2kHz, although it is somewhat irregular that 500Hz PRR shows better machining effectiveness

than 1000Hz PRR. However, the more important point is that machining effectiveness starts to decrease after 2kHz, implying that the optimum PRR for the maximum effectiveness exists around 2kHz. The major phenomenon explaining the optimum PRR is the dehydration of the machining site; the ablation dehydrates the machining site until it refills with water. So, the next pulse should come after the machining site is sufficiently hydrated, otherwise the water circulation significantly decreases and debris extrusion becomes very difficult.

3.3. Effect of feed-rate: MSSL method

The MSSL method is used to optimize primary parameters, especially when any specific length of subsurface capillary is set as a target. The MSSL method mainly focuses on the effect of feed-rate on machining performance with fixed PRR of 1.5kHz and 10nJ pulse energy.

As shown in Fig. II. 10, seven different capillaries, with target lengths ranging from 20μm to 50μm in 5μm increments, are machined with feed-rates varying from 5 to 45μm/s. Therefore machining efficiency and effectiveness vs. feed-rates are evaluated by resulting machining times. Fig. II. 10 shows that faster feed-rates require less machining time to achieve the target lengths, implying that faster feed-rates improve the machining efficiency and effectiveness. This result is more clearly shown by calculating machining efficiency and effectiveness, as shown in Fig. II. 11 and Fig. II. 12.

Although both the efficiency and the effectiveness increase with feed-rate, their improvements tend to flatten after 30μm/s. Considering that faster feed-rate can cause more inaccuracy in the motion of the linear nanostage, 30μm/s feed-rate can be considered the optimum. Also, it is found that longer channels take much more energy and time, decreasing the machining efficiency and effectiveness; for example, doubling the capillary length requires approximately 4 times longer machining time. This nonlinearity exists because water circulation becomes increasingly difficult as the length of the channel increases, requiring more pulses for the material subtraction and more back-scanning for debris extrusion.

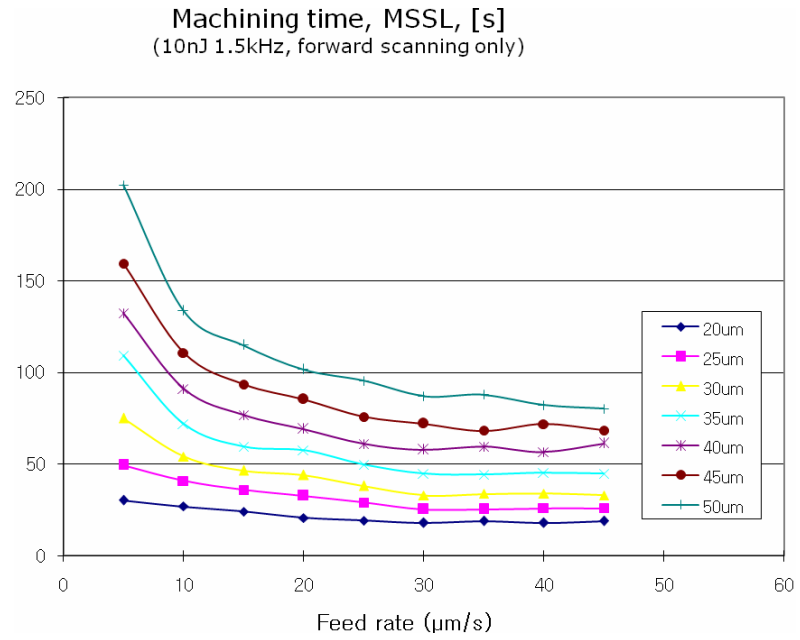

Fig. II. 10. Machining time vs. feed-rate

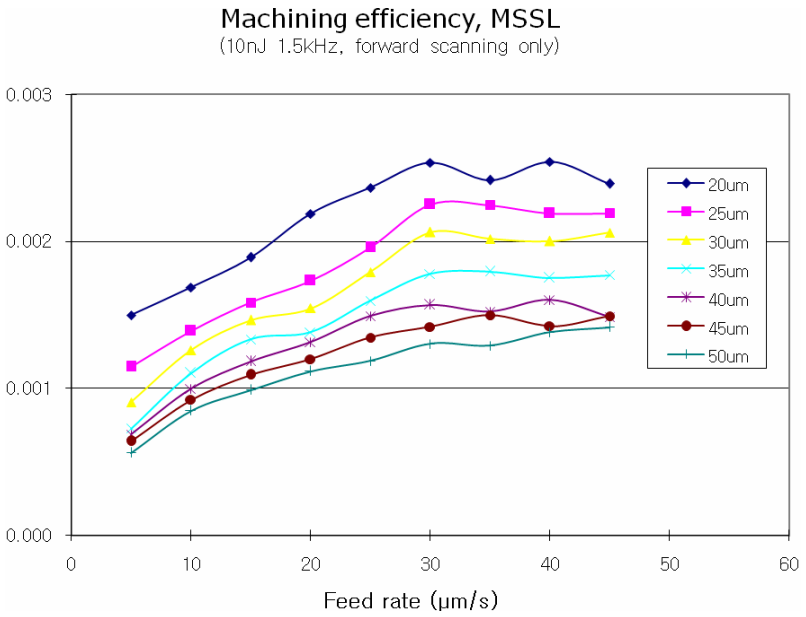

Fig. II. 11. Machining efficiency based on MSSL vs. feed-rate

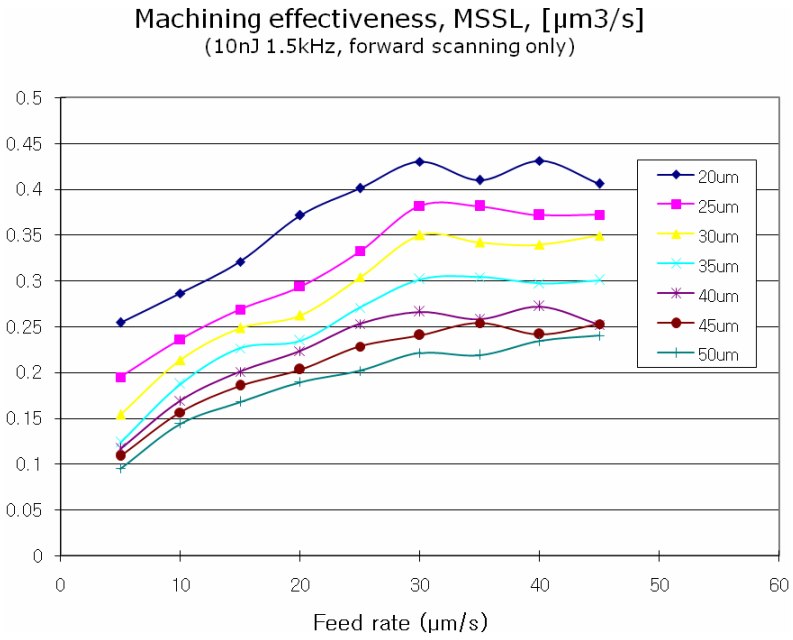

Fig. II. 12. Machining effectiveness based on MSSL vs. feed-rate

3.4. Laser chopping for high PRR lasers

The previous parametric studies determined that the optimum PRR and feed-rate are 2kHz and 30µm/s, respectively in the PRR range of 0.5-3kHz. Machining efficiency of 1% and machining effectiveness of 3µm^3/s can be achieved at 2kHz PRR.

However, a high PRR laser having a range of 100-200kHz (µJewel, IMRA; see appendix 1) exhibits worse machining effectiveness, despite machining with hundred times higher PRR with the same pulse energy transferring hundred times higher power input to the material. The dehydration problem at the ablation site is highly suspected.

To clearly elucidate the effect of the dehydration problem and to determine the optimum pulse control condition, a laser chopping method is applied. By changing the laser chopping frequency, the minimum time required for water to re-hydrate the ablation site can be estimated.

Fig. II. 13 shows the chopper wheel geometry that determines the chopping frequency and duty ratio.

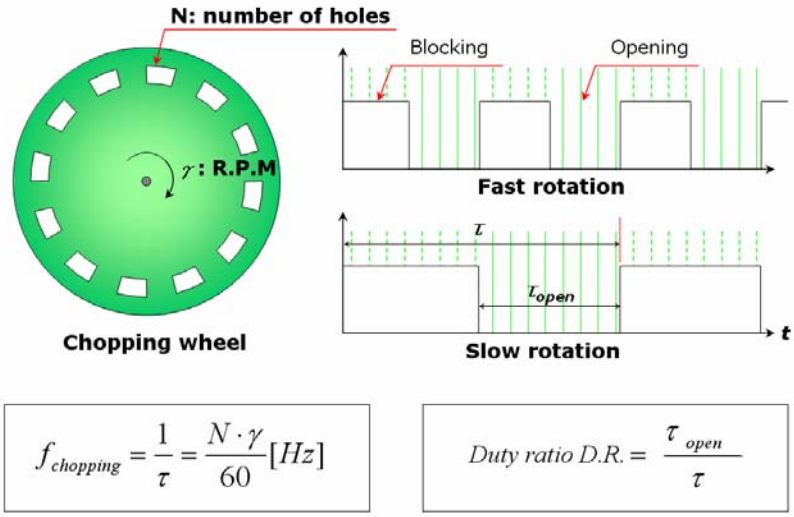

$$f_{chopping} = \frac{1}{\tau} = \frac{N \cdot \gamma}{60}[Hz]$$

$$Duty\ ratio\ D.R. = \frac{\tau_{open}}{\tau}$$

Fig. II. 13. Schematics of mechanical laser chopping

As shown in Fig. II. 14, although the application of laser chopping decreases the power input to 50%, the machining performance monotonically increases until the chopping frequency reaches 800Hz, which is its maximum in this setup. No pulses are blocked at 0 chopping frequency, implying the average power input is twice as high.

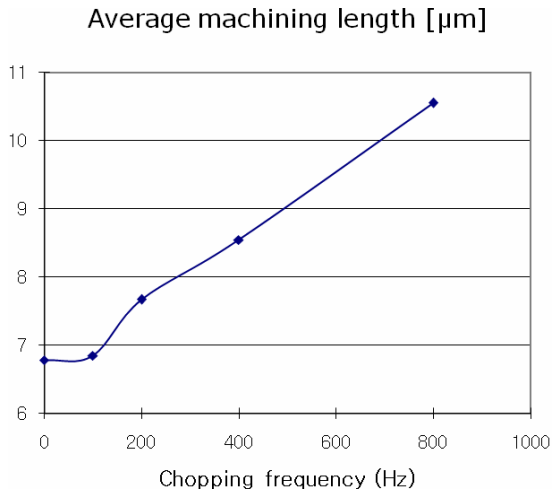

Fig. II. 14. Average machining length vs. pulse chopping frequency

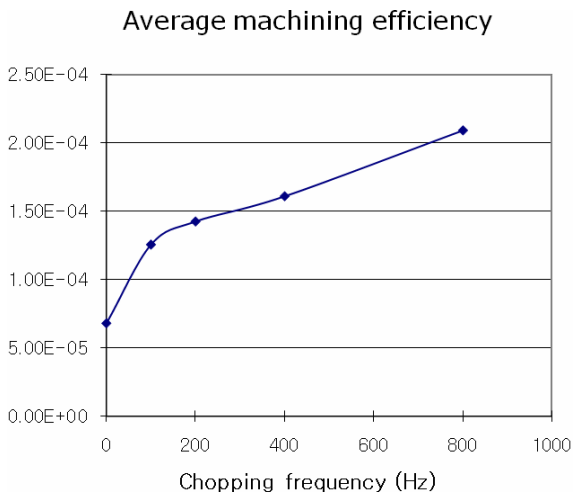

Fig. II. 15. Average machining efficiency vs. pulse chopping frequency

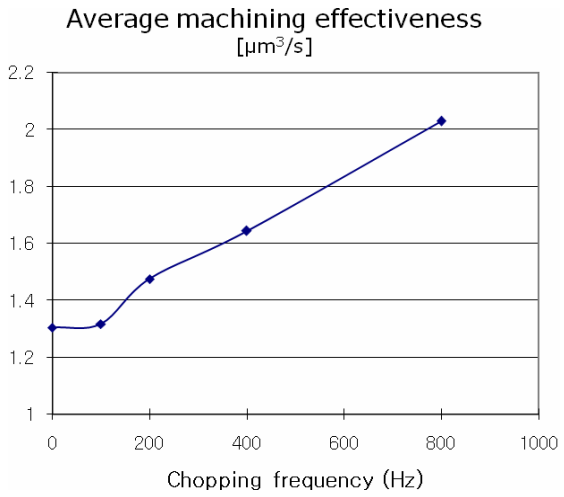

Fig. II. 16. Average machining effectiveness vs. pulse chopping frequency

As shown in the Fig. II. 15, the machining efficiency also monotonically increases, mainly because more subtractions are achieved with fewer pulses. At a chopping frequency of 100Hz, the same machining effectiveness is achieved with half as many pulses, doubling the machining efficiency. Finally, a chopping frequency of 800Hz achieves nearly 4 times machining efficiency and 2 times machining effectiveness compared with unchopped machining.

If the dehydration of the ablation site is the major phenomenon of interest, the machining performance should finally decrease again at a few kilohertz chopping

frequency, as it does for PRR.

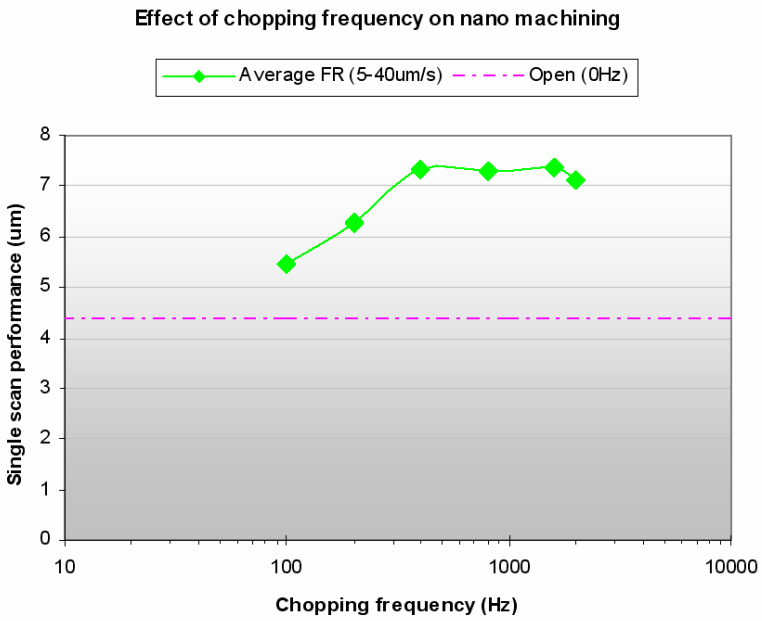

Fig. II. 17. Fast laser chopping shows local maxima

In order to test higher chopping frequencies, another chopper wheel having more apertures is applied. Geometrical duty ratio of the new chopper wheel is 50%, which equals that of the coarse aperture wheel, but the average power input after chopping with this wheel is measured as 43%; more numbers of apertures increase the diffraction at the aperture edges.

As shown in Fig. II. 17, it is confirmed that the optimum chopping frequency exists in the range from 800Hz to 1.6kHz, verifying that dehydration is the main problem attenuating the effect of higher power input via higher PRR on machining performance.

The optimum chopping frequency is somewhat slower than the optimum PRR. This is quite reasonable in that the refilling time of 1kHz chopping frequency is just 0.5ms, which is the same as the refilling time of 2kHz PRR. Thus the optimum chopping frequency is in general around half the optimum PRR.

4. Theoretical approaches on dehydration frequency

The dehydration theory well explains the adverse effect of high power input via high PRR on the machining performances. When a femtosecond laser pulse is applied, dehydration of the ablation site will be caused by three processes: 1) a direct ablation of water film on the wall, 2) sweeping of water film by pressure blasts during the ablation, and 3) water film evaporation on the heated capillary wall. As shown in Fig. II. 18, the water film evaporation will instantaneously progress up to a certain distance from the ablation site, at which point the surface tension begins to once again draw the thin water film to the ablation site.

Based on this refilling process, the dehydration frequency can be defined as the inverse of the refilling time or dehydration time. Experimentally, the dehydration frequency can be defined as the PRR at the maximum effectiveness. Above the dehydration frequency, the machining effectiveness decreases again.

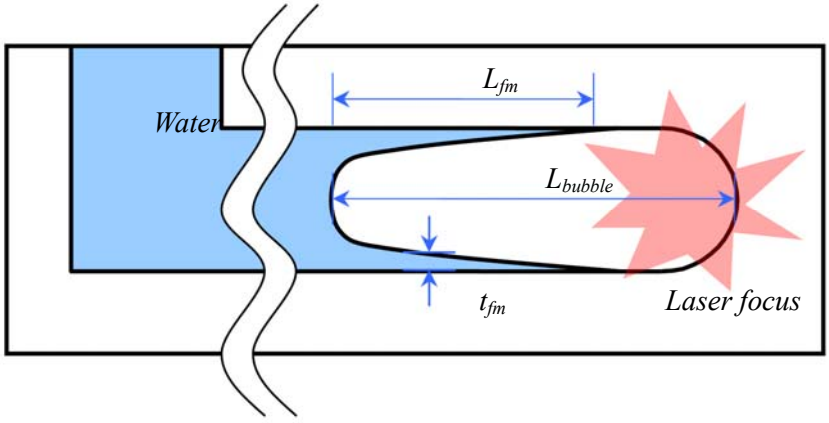

Fig. II. 18. Schematic of thin film formation at the nanocapillary wall

The dehydration frequency can be theoretically analyzed based on the dynamics of the thin water film forming on the wall surface. The refilling phenomenon can be simplified as the force balance between the capillary force and the viscous force acting on the wall, as shown in equation (2). Note that the thin water film is assumed to act as a Newtonian fluid.

$$2\pi r\sigma = 2\pi r L_{fm}\eta \frac{U_{fm}}{t_{fm}} \tag{2}$$

Where t_{fm} is film thickness [m], L_{fm} is film length [m], U_{fm} is film velocity [m/s], σ is surface tension (≈0.072 [N/m]), and η is dynamic viscosity of water (≈10^{-3} [Ns/m^2]).

Based on equation (2), the film velocity can be calculated as equation (3). Here, bubble length, L_{bubble}, assumes the overall travel length of the film [m]. And τ_{rf} is the refilling time [s].

$$U_{fm} = \frac{L_{travel}}{\tau_{rf}} \approx \frac{L_{bubble}}{\tau_{rf}} = \frac{\sigma t_{fm}}{\eta L_{fm}} \tag{3}$$

The inverse of the refilling time is the dehydration frequency. L_{fm} is assumed equal to the bubble length.

$$f_{dhy} = \frac{1}{\tau_{rf}} \approx \frac{\sigma t_{fm}}{\eta L_{fm} L_{bubble}} \approx \frac{\sigma t_{fm}}{\eta L_{bubble}^2} \tag{4}$$

Based on equation (4), which does not consider the effect of surface roughness, 10nm of film thickness and 5μm bubble length yield a dehydration frequency of 28kHz, which exceeds the optimum PRR.

The effect of surface roughness will increase the overall travel length of the film, because the film thickness will be similar or thinner than the surface roughness. Thus the surface roughness effectively increases the travel length. Also, the entrained debris in water is expected to increase the viscosity of the water, increasing the viscous force.

Considering all these additional effects, equation (4) can be modified as:

$$f_{dhy} \approx \frac{\sigma t_{fm}}{\varepsilon^2 \eta' L_{bubble}^2} \tag{5}$$

Where ε is the travel length modification constant and $\acute{\eta}$ is the effective viscosity of water entraining debris. Equation (5) will decrease the dehydration frequency below 28kHz; for example, with ε of 3 and $\acute{\eta}$ of 1.5×10^{-3} [Ns/m^2] the dehydration frequency becomes 2.13kHz.

Because these specific numbers are all assumed, an accurate calculation is impossible. However, considering the accuracy within at least 1 order of magnitude, the derived equation can be assessed to explain the correct physical mechanism. Additional parametric studies for testing the effect of water surface tension on the dehydration frequency can be performed to further validate the dehydration theory.

5. Discussions

Parametric researches suggest that the optimum PRR of 2kHz (or optimum pulse to pulse time interval of 0.5ms) and the optimum feed-rate of 30μm/s maximize the machining effectiveness as summarized in the TABLE I. Although the pulse energy increases the machining performances almost linearly, feature size of the target geometry should be first considered to determine the appropriate pulse energy. In addition, the maximum pulse energy is usually limited based on the optical setting, because too high pulse energy decreases machining quality and precision due to the presence of the collateral damages such as cracks.

	Low PRR laser (0.5-3kHz)		High PRR laser (100-200kHz)
	Opt. PRR	Opt. feed-rate	Opt. f_{chop}
	2kHz	30μm/s	0.8-1.6kHz
Effectiveness	$2.9\mu m^3/s$		$2\mu m^3/s$
Efficiency	0.8%		0.21%

TABLE I. The results of parametric measurements: the optimum laser parameters and the achieved maximum machining performances

The dehydration theory well explains why higher power input via higher PRR decreases machining performance, especially when water is used to assist femtosecond laser machining. The dehydration of the ablation site is not avoidable, although the strong surface tension of water quickly refills the ablation site in nanocapillaries.

Based on the equation for the dehydration frequency it can be expected that micron-scale optical machining may find the maximum machining performances at lower PRR point than the results. Thus, the specific numbers found in this dissertation will not be directly applicable to other scale machining regimes. However, the same concepts and the same protocols will be directly applicable to any scale machining regime.

Considering that increasing PRR for higher power inputs is desired to increase material subtraction rate with the same feature size, the dehydration problem will be the major issue in any scale optical machining regimes. As expected that larger scale machining regimes will make optimum machining condition at lower PRR, these regimes are expected to more significantly suffer from the dehydration problem, because much

higher pulse energy and much larger feature size will require much longer refilling time.

The protocols performed in the parametric researches and the theory on the dehydration of the ablation site are expected to improve the fabrication performances of more complicated subsurface nanogeometries and to be well applicable to the optimization of larger feature size regimes.

CHAPTER III

ACOUSTIC PHENOMENA IN LONG NANOCHANNEL MACHINING

1. Introduction

Micro total analysis systems (μTAS) endeavor to implement complex analytic processes on a chip for simplified analyses, decreased costs, and minimal sample volumes. This objective requires that complex micro/nanofluidic networks be integrated into a single chip, with increasing requirements for 3-dimensional geometries and submicron-scales, both of which are challenging to address through conventional planar lithography-etch-bond processes. Laser-induced optical ablation by femtosecond laser pulses constitutes a promising method for submicron-scale fabrication in dielectric materials [21-25], and owing to the development of the water-assisted fs-laser-machining [26,27], it is now possible to directly fabricate true 3-dimensional nanochannels in the subsurface of dielectrics using far-field nanoablation [28-31] without using cleanroom facilities or challenging multilayer lithography processes [34].

For femtosecond laser machining to reach its full potential, machining of sufficiently long nanochannels should be achieved to realize complex 3-dimensional micro/nanofluidic networks in μTAS [35] applications.

However, NCL's > 50 have not been achieved using laser or conventional drilling methods [36] due to debris extrusion difficulties; as the machining progresses far into the material, debris extrusion becomes more difficult, resulting in an accumulation of debris in the channel.

This NCL limitation can be improved to 200 by taking advantage of the efficient debris extrusion in water assisted femtosecond laser machining [29]. However, it is found that machining becomes extremely slow and difficult at channel NCL ≈ 300; internal circulation is severely attenuated as the bubbles become stationary. When the channel NCL approaches 300, the internal structure of fluid flow becomes stabilized into a meta-

stable water-gas-water (WGW) structure, with water plugs at the inlet port and dead-end of the channel, and a large gas plug in the middle. NCL = 300 is the point at which the resonance of the internal structure matches the pressure propagation in the channel, thereby effectively canceling out the pressure generation by bubble expansion. Thus the energy delivered to the ablation site may be readily transferred through the WGW structure. This is the formation of the first acoustic node, which is analogous to the nodes in standing waves, although they are physically distinct.

Acoustic node formation is a significant barrier to high NCL subsurface capillary fabrication, leading to a practical termination of machining. Acoustic nodes must be overcome for machining to continue as long as possible. It is found that substantial repetitive machining over the difficult area can possibly overcome acoustic nodes, and after a local barrier is overcome the machining is considerably restored until the emergence of the next node.

The second node formation is considered a practical NCL maximum of subsurface nanocapillaries, because the significantly weakened driving force (ΔP) due to the node formation can hardly overcome the increased hydrodynamic resistance to the circulation (R_{cir}) in such a long nanocapillary. Therefore, methods to delay the acoustic node formation or to radically prevent its formation are required to achieve high NCL channel fabrication.

In this chapter, a theoretical approach based on resonance of the WGW structure with the pressure wave oscillation elucidates strategies to delay acoustic node formation. These strategies include decreasing the pressure, increasing the temperature, and increasing the mole fraction of hydrogen in bubbles.

Among these strategies, degassing water, which considerably increases the mole fraction of hydrogen, is found to be very effective in delaying the first acoustic node formation up to an NCL of 600. Owing to this dramatic delay, the degassed-water-assisted fs-laser-machining could achieve high NCL subsurface nanocapillaries with NCL > 1000.

Also, as suggested by the resulting node equation from the analytical model, pressure experiments show that pressure can effectively control the node formation. Thus, the validity of the analytical model and the node equation is further solidified.

2. Acoustic node formation

2.1. Termination of subsurface capillary

Termination of machining can be practically determined when channel subtraction no longer follow the focused laser, as shown in Fig. III. 1. Two major reasons for machining termination can be suggested: faster machining speed than the actual subtraction rate, and debris accumulation hindering favorable water circulation.

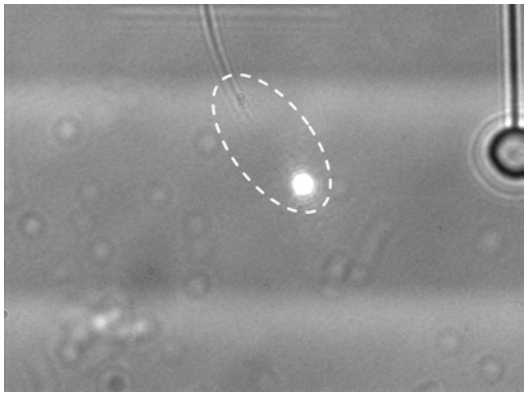

Fig. III. 1. Machining termination can be determined when material subtraction no longer follows the focused laser.

As the subtraction rate decreases with increasing channel length, debris extrusion becomes increasingly difficult. Thus the feed-rate needs to be properly decreased, and periodic full-back-scanning is essential for debris-free machining. In addition, narrow localized oscillatory scanning over the machining site is also very effective; for example, the repetition ratio between the number of the narrow localized oscillatory scanning and the full back-scanning is gradually increased from 5:1 to 10:1.

In water-assisted fs-laser-machining, optimizing these patterns of machining in terms of variable feed-rates and repetitive back-scanning can be used to achieve improved NCL's of up to 300.

2.2. Bubble retardation

Optimized machining can maintain very effective machining without debris accumulation until the NCL reaches 300. In this mode, channel subtraction always tracks the focused laser, and favorable bubble expansion and water circulation are preserved.

However, abrupt machining termination tends to occur near NCL of 300. Prior to the termination, abrupt bubble retardation is also observed. As shown in Fig. III. 2 (a), favorable bubble generation and its expansion is shown until the length of capillary becomes 220μm, with an equivalent NCL of ~320. However, as the machining progresses for several microns, severe bubble retardation becomes evident, eventually leading to the zero-bubble-growth as shown in Fig. III. 2 (b) and (c).

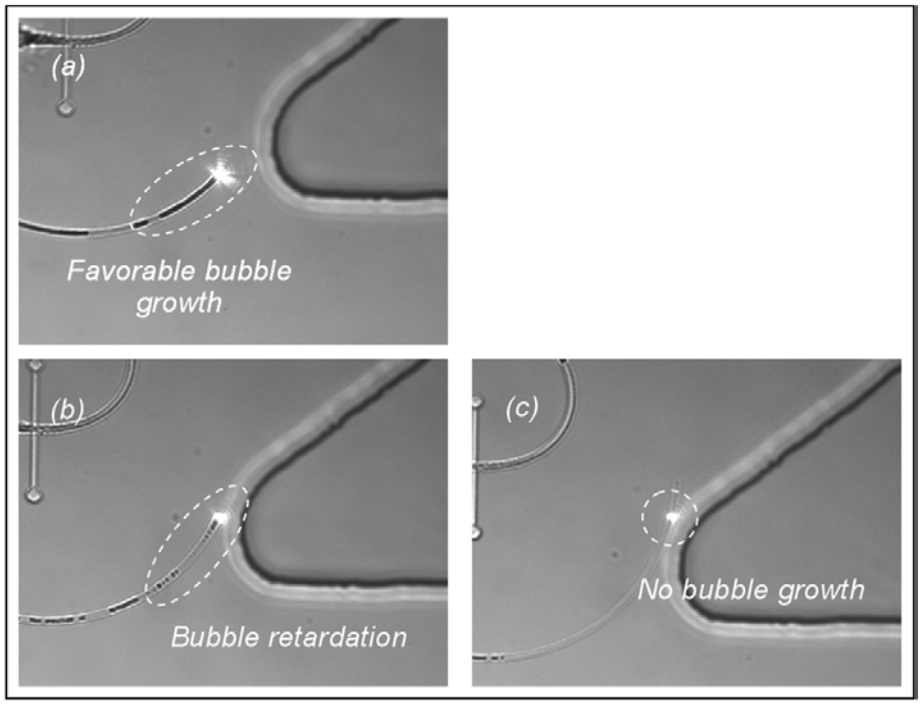

Fig. III. 2. Bubble retardation near acoustic nodes

Termination of machining occurs after the abrupt retardation and termination of bubble growth. Although the capillary length is far shorter than NCL of 300, it is observed that bubble retardation happens prior to the termination of machining.

Thus, bubble retardation is closely related to the termination of machining. As described in equation (1), water circulation should be sustained to keep machining with favorable bubble generation and expansion. So, once bubble growth is restricted for any reason, the water circulation is degraded, breaking the should-be-kept balance between debris generation and extrusion against debris accumulation. In turn, the accumulation of debris in the capillary further weakens the bubble expansion and water circulation, eventually resulting in the termination of machining.

Therefore, favorable bubble expansion is the key feature for water-assisted fs-laser-machining to be sustained.

2.3. Observation of the first acoustic node formation

As the NCL approaches 300, abrupt termination of machining can be no longer overcome by adjusting control parameters such as feed-rate. Channel elongation is severely diminished, even though the channel is free of debris. This machining retardation occurs due to acoustic node formation, which drastically diminishes bubble generation and expansion.

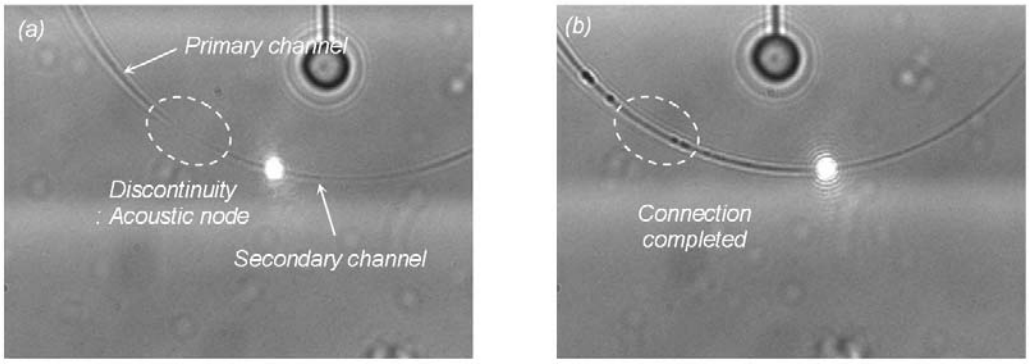

Fig. III. 3. First acoustic node formation

Repetitive machining over the difficult region starts to restore channel subtraction, however, this channel is visually discontinuous from the primary channel as shown in Fig. III. 3 (a). This discontinuity is taken to be the location of the first acoustic node. With further machining, the primary and secondary channels eventually unite, forming one longer channel as shown in Fig. III. 3 (b). The machining rate in the discontinuity is very slow compared with that of the primary or secondary channel.

The acoustic node is characterized by a local minimum of ΔP (refer to equation (1)) leading to severe attenuation of the channel circulation, as shown in Fig. III. 4; thus, excluding a simple assumption on the ΔP depends only on the pulse energy.

The first local minimum of ΔP (the first acoustic node) is the first critical barrier to channel machining; once it is overcome, machining rate is restored until encountering the second acoustic node.

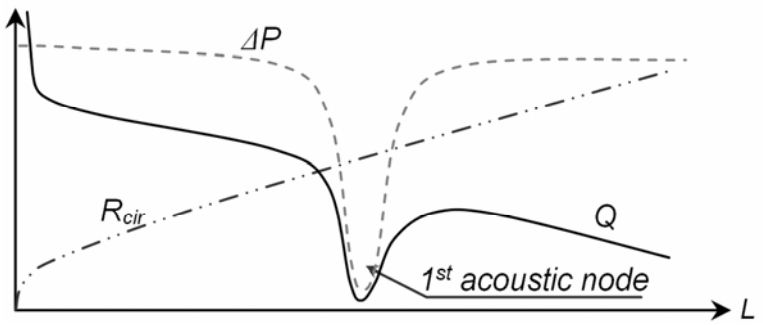

Fig. III. 4. Schematic illustration of the effect of the first acoustic node on channel circulation; the first local minimum of channel circulation is the location of the first acoustic node.

3. Analysis on the first acoustic node formation

3.1. Meta-stable water-gas-water structure

The first acoustic node formation is found to be induced by structural resonance. Upon encountering the initial site of inhibited machining, a two phase structure becomes evident within the channel; a large gas plug is formed in the middle of the channel while the inlet and terminal end of the channel are filled with water plugs, as shown in Fig. III. 5. This meta-stable WGW (water-gas-water) structure is readily visible by light microscopy in the experimental setup.

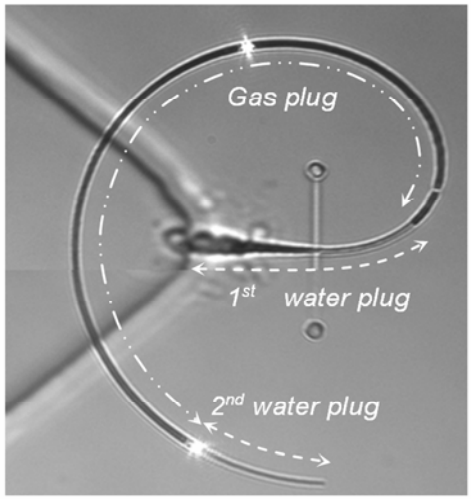

Fig. III. 5. Meta-stable WGW structure

Formation of the gas plug is ascribed to continuous bubble generation at the ablation site, where bubbles escaping from the ablation site to the outside of the channel

form a stable gas plug in the middle of the channel. However, if the channel length is very short (NCL< 50), a stable gas plug struggles to form as the flow of bubbles is too quick to form a stable gas plug due to very small hydrodynamic resistance acting on the bubbles.

As the channel grows, the internal configuration becomes more stable. When the nanocapillary NCL becomes greater than 200, a meta-stable WGW structure of internal configuration becomes more evident. This WGW formation is almost kept as quasi-steady-state until the machining overcomes the first acoustic node. The internal configuration becomes more complex, such as WGWGW, but is no longer as stable as the WGW structure for the first acoustic node.

3.2. Acoustic model based on resonance of WGW structure

The meta-stable WGW structure becomes increasingly stable as the machining encounters the first acoustic node, resulting in a structure that is no longer scattered or moved, even under ablation.

The stabilized WGW structure can be understood as a spring-mass system, whose vibration can be analyzed by assuming three components: the water plug acts as a mass, the gas plug as a spring, and viscosity as damping. Although the viscous effect would be considerable in nanoscale geometries, an undamped vibration model is taken into consideration for the first acoustic node analysis because the movement/velocity of the first water plug is assumed to be zero at the moment of resonance. Thus, the spring-mass model excluding damping would be effective only upon formation of the first acoustic node.

As shown in Fig. III. 6, the natural frequency of the WGW structure, f_n, can be evaluated. The spring constant of gas plug is derived based on the Boyle's Law.

$$PV = const \quad \rightarrow \quad VdP + PdV = 0 \tag{6}$$

P and V are the internal pressure and volume of the gas plug.

$$dP = -\frac{PdV}{V} = \frac{PAdx}{V} = \frac{Pdx}{L} \tag{7}$$

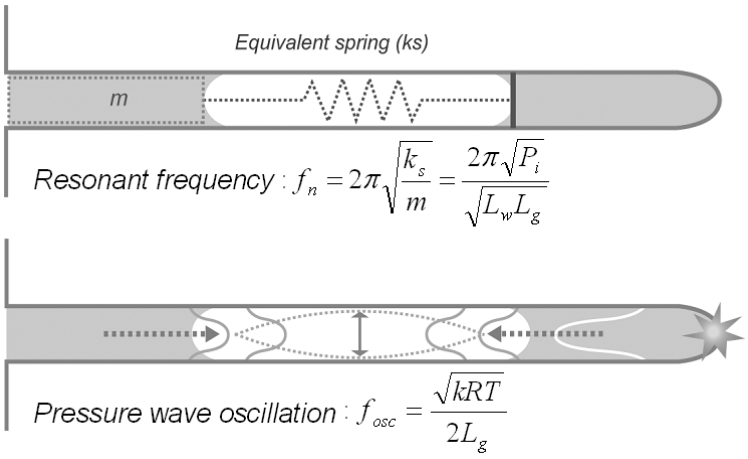

Fig. III. 6. Vibration model for the resonance of WGW structure with pressure wave oscillation.

The direction of x is in compression, so the sign of dx is opposite to dV. A is the cross-sectional area of the channel that is assumed to be constant.

$$k_s = \frac{dF}{dx} = \frac{AdP}{dx} = \frac{PA}{L} \tag{8}$$

Equation (7) is plugged into equation (8) to get the final form of k_s.

With the effect of viscosity is neglected, the natural frequency, f_n can be calculated with the mass of the first water plug ($\rho_w A L_{w1}$) as equation (9)

$$f_n = 2\pi\sqrt{\frac{k_s}{m}} = \frac{2\pi\sqrt{P_i}}{\sqrt{L_{w1} L_g \rho_w}} \tag{9}$$

k_s is the equivalent spring constant [N/m], m is the equivalent mass of 1st water plug [kg], P_i is the internal pressure of the gas plug [Pa], L_g and L_{w1} are the lengths of gas and water plug [m], and ρ_w is density of water. For further simplification, the dimension of internal pressure is replaced with kilopascals instead of pascals, which then cancels out the density of water, ρ_w=1000kg/m^3, yielding equation (10).

$$f_n = \frac{2\pi\sqrt{P_i}}{\sqrt{L_{w1} L_g}} \tag{10}$$

When new dimensions for P_i, L_g, and L_{w1} are defined as kilopascal and micrometer, the dimension of the natural frequency becomes megahertz: f_n [MHz], P_i [kPa], and L_g, and L_{w1} [μm].

The oscillation frequency of the pressure wave in the gas plug is much simpler;

the speed of sound in the gas plug is divided by its travel length, which is twice the length of the gas plug. As the speed of sound can be described by the temperature (T [K]), the specific gas constant (R [J/kgK]), and the ratio of specific heat constants (k [dimensionless]), the oscillation frequency, f_{osc} can be derived as the equation (11);

$$f_{osc} = \frac{\sqrt{kRT}}{2L_g} \tag{11}$$

For consistency, micrometer instead of meter is used as the dimension of L_g, then the dimension of f_{osc} also becomes megahertz.

When these two frequencies are matched, the first acoustic node forms;

$$\frac{2\pi\sqrt{P_i}}{\sqrt{L_{w1}L_g}} = \frac{\sqrt{kRT}}{2L_g} \tag{12}$$

$$L_g = \left(\frac{kRT}{16\pi^2 P_i}\right)L_{w1} \tag{13}$$

Therefore, the node position, which is sum of L_{w1}, L_g, and L_{w2}, can be derived to yield equation (14);

$$L_{node} = L_{w1}\left(1 + \frac{kRT}{16\pi^2 P_i}\right) + L_{w2} \tag{14}$$

Equation (14) describes the node position with several parameters. The length of the water plugs should be measured experimentally, and the other parameters (k, R, T, and P_i) need further study to be properly estimated.

First, the temperature of the gas plug is determined through a theoretical estimation based on the simplified model. Second, the pressure of the gas plug is accurately measured through an experiment of a nanobubble collapse in a nanocapillary; the theoretical estimation based on the Laplace's law is found to differ considerably from the actual pressure of nanobubbles. Finally, the gas constant and ratio of specific heats are analytically evaluated by a gas composition analysis of the nanobubbles comprising the gas plug. The gas composition is very difficult to directly determine through either experiments or numerical simulations, so a comparison analysis between node formation and gas composition yields the final solution.

4. Analysis of the node equation

4.1. Temperature analysis of gas plug

A simple model for femtosecond laser machining can be established based on spherical heat transfer. The overall thermal resistance of the substrate can be estimated by the radial heat transfer in a spherical geometry, as shown in the equation (15); k_g is the thermal conductivity of glass [W/mK], r_o is the outer boundary of the internal heat source [m], and R is the outer radius of the glass substrate [m].

$$R_{subst}^{cond} = \frac{1}{4\pi k_g}\left(\frac{1}{r_o} - \frac{1}{R}\right) \tag{15}$$

The convective heat resistance can be simply described with equation (16); A is the surface area [m^2] and h is the convection coefficient [W/m^2K].

$$R_{suf}^{conv} = \frac{1}{Ah} \tag{16}$$

These two resistances constitute the overall thermal resistance within equation (17). Moreover, although the exact values are not easy to estimate, the second and third terms i equation (17) are smaller than the first term by 2-3 orders of magnitude; thus, these two terms can be eliminated, further simplifying the equation as the final form.

$$R_{overall} = \frac{1}{4\pi k_g}\frac{1}{r_o} - \frac{1}{4\pi k_g}\frac{1}{R} + \frac{1}{Ah} \approx \frac{1}{4\pi k_g}\frac{1}{r_o} \tag{17}$$

The average temperature rise is calculated by dividing the average power input by the overall thermal resistance. η_{absp} is the absorption efficiency of the laser power into the material, e_p is the pulse energy [J], and f_{PRR} is PRR [Hz].

$$\Delta T \approx \frac{\eta_{absp} e_p f_{PRR}}{4\pi k_g r_o} \tag{18}$$

To solve equation (18), η_{absp} and r_o need to be specified. η_{absp} can be estimated as about 0.3 and r_o can be used as the radius of the focused laser under the assumption that the focused laser is stationary. However, because the focused laser moves with 40-50μm/s feed-rates, a much larger volume than that of the focused laser must be taken as the internal heat source. To consider more realistic situations, several estimates for r_o could be employed. For example, r_o could be estimated to have the same surface area or the same volume as the actual scanning, calculating r_o as about 2.95μm or 1.66μm.

A temperature rise of 0.95K, calculated using the radius of the focused laser, represents the maximum estimate and is the case only when the focused laser does not move. Using larger estimates of r_o of 2.95μm and 1.66μm yield temperature rise calculations of 0.11K and 0.2K.

Therefore, it can be concluded that the average temperature rise of the gas plug during machining will not exceed 1K, which is small enough to assume room temperature for the gas plug.

4.2. Internal pressure of gas plug

The internal pressure of the gas plug can be more directly and accurately evaluated by measuring bubble compression in nanocapillaries, where the actual internal pressure of the gas plug is found to be considerably different from its theoretical estimate based on Laplace's law. The difference is due primarily to the contact angle at the wall surface, where about 10% surface roughness confers the difficulties of theoretical evaluation on the contact angle.

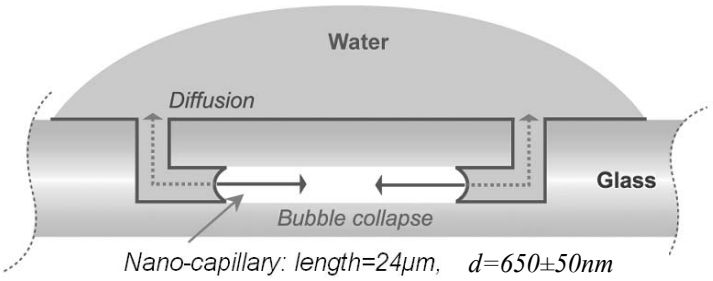

Fig. III. 7. Schematics of the bubble collapse in nanocapillaries.

Four nanocapillaries of length 24μm and of diameter 650±50nm are machined in a glass cover slip and allowed to dry. As shown in Fig. III. 7, when a water droplet is placed over the channel entrances, 63% of each nanocapillary (in terms of volume) is filled with water within 70ms by strong capillary force, compressing the air within into 9μm long bubbles. During the compression the rate of bubble collapse in length is greater than 214μm/s; thereafter, collapse is slow, averaging 1.8μm/s, as the gas diffuses into the liquid as shown in Fig. III. 8 and Fig. III. 9.

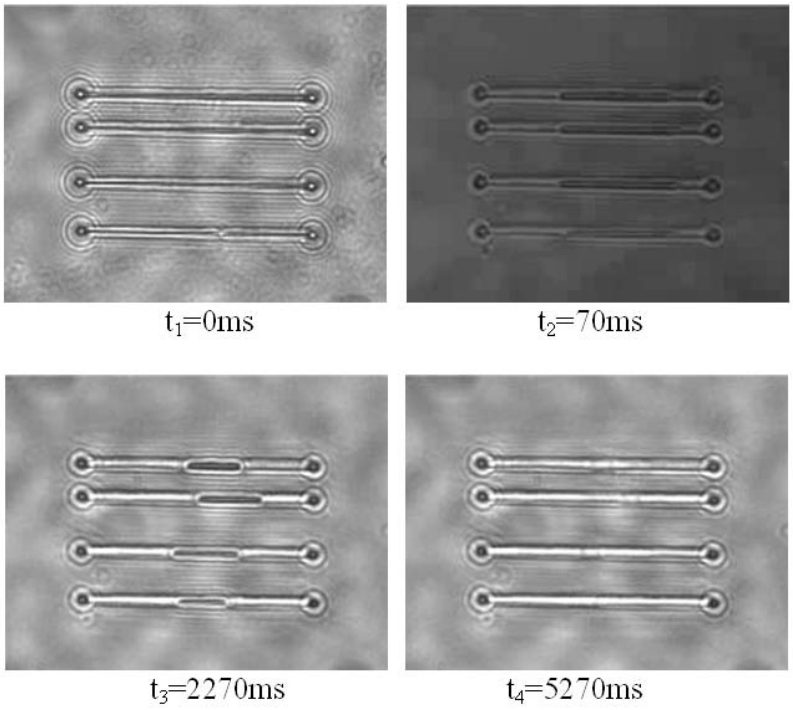

Fig. III. 8. Microscopic images showing fast compression of air into nanobubbles and resultant collapse due to diffusion.

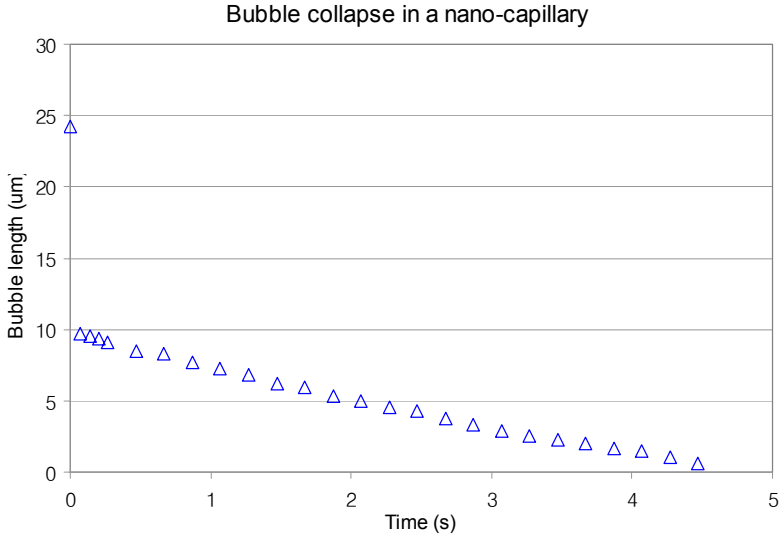

Fig. III. 9. Measured bubble collapse following the initial compression.

The internal pressure of the gas plug in the nanochannel is calculated from the extent of rapid compression, giving 260kPa based on a volume compression ratio of 2.5. Therefore, an empirical equation for the internal pressure of the gas plug can be found, as in equation (19):

$$P_i \approx P_o + 160 \tag{19}$$

P_i and P_o are the internal and external pressures of a bubble [kPa].

Internal pressure of the gas plug can be estimated according to Laplace's law;

$$P_i = P_o + 2\sigma\kappa\cos\theta \tag{20}$$

σ is surface tension of water [N/m], κ (=1/r) is the curvature at an end of the plug [1/m], and θ is the contact angle between the water-gas interface and channel wall.

Assuming that the radius of the gas plug is similar to the radius of the channel, the contact angle is zero and the external pressure is 100kPa. These approximations yield an internal pressure of 488±80 kPa for a channel with radius of 350±25nm. The difference between the experimental result and theoretical estimation indicate that the contact angle is greater than zero. In fact, based on the experimental result, the contact angle is calculated as 65±5°.

4.3. Analyses of gas composition of gas plug

The gas plug is composed of several gases due primarily to the ablation of water, which can be analyzed by three possible processes: 1) the dissociation of water molecules into hydrogen and oxygen, 2) diffusion of dissolved gases in water such as nitrogen and oxygen, and 3) water vaporization.

Those gases initially form nanobubbles, which grow and congregate together forming a relatively larger gas plug in the middle of the capillary. The speed of sound in the gas plug is, thus, dependent upon the mole fraction of these gases, which are nitrogen, oxygen, hydrogen, and steam. So, equation (14) can be modified into equation (21), which is the node equation.

$$L_{node} = L_{w1}\left(1 + \frac{k_{mix}R_{mix}T}{16\pi^2 P_i}\right) + L_{w2} \tag{21}$$

where k_{mix} is ratio of specific heats for the mixture (c_p^{mix}/c_v^{mix}) and $R_{mix} = R_{univ}/M_{mix}$ is the gas constant for the mixture; R_{univ} is universal gas constant (8314 [J/kmolK]) and M_{mix} is molecular weight for the mixture. When pure water is used for nanocapillary machining, the internal pressure of the gas plug can be substituted by equation (19), yielding

$$L_{node} = L_{w1}\left(1 + \frac{k_{mix} R_{mix} T}{16\pi^2 (P_o + 160)}\right) + L_{w2} \tag{22}$$

Based on the theoretical estimation described earlier, the average temperature rise during machining is less than 1K. However, the instant temperature rise could reach over 10,000K, which can be approximated using both a numerical analysis and a simple theoretical calculation. This means that sufficient amount of steam can be generated to saturate the, especially after the gas plug is cooled down to room temperature. Therefore, the mole fraction of water vapor would be about 1% assuming saturation at room temperature. Thus the gas composition of the gas plug can be expressed as TABLE II.

Machining type	Gas composition by mole fractions ($\alpha \leq 1$)
DWA, SWA	$\alpha(\frac{2}{3}H_2+\frac{1}{3}O_2) + (0.99-\alpha)(0.65N_2+0.35O_2) + (0.01)H_2O(g)$
Cpt. DWA	$0.99(\frac{2}{3}H_2+\frac{1}{3}O_2) + (0.01)H_2O(g)$

TABLE II. Gas composition of the gas plug according to the machining type/degree of degassing: DWA – degassed-water-assisted; SWA – saturated-water-assisted; Cpt. DWA – completely degassed-water-assisted.

In TABLE II, α is the fraction of gases from the water dissociation so that (0.99-α) becomes the other fraction of gases diffused from dissolved gases in water; the mole fractions of nitrogen and oxygen dissolved in water are calculated to be 0.65 and 0.35 based on their solubility and partial pressures. So, the gas composition of the gas plug for DWA (partially degassed) or SWA machining, can be expressed with only one unknown variable α, as shown in TABLE II. Also, if the water is completely degassed allowing no gas diffusion from water, the gas composition would be fixed to approximately ~2/3 H_2 and ~1/3 O_2, achieving maximum mole fraction of hydrogen of about 66%.

Because the node position and water plugs are experimentally measured, α is also the only unknown variable in the node equation; thus, α can be found by solving the node equation.

In order to determine α, the node equation is applied to and compared with three experiments: two degassed-water-assisted and one saturated-water-assisted machining as shown in TABLE III.

In the SWA machining experiment the first acoustic node formed at 181μm with L_{w1} and L_{w2} of 24 and 80μm. The node equation then finds that α=0.22 gives exact agreement to the measured node position. Also, in the two DWA experiments measuring (node; L_{w1}; L_{w2}) as (320;40;103) and (352;46;101), the node equation very accurately predicts the node positions of 321 and 351μm with α=0.63 at both cases, which is very close to the experimentally measured node positions. For completely degassed water (α=0.99), 413 and 458μm are predicted as theoretical maxima.

Machining		T (K)	P_i (kPa)	α	L_{w1} (μm)	L_g (μm)	L_{w2} (μm)	Node (μm)
DWA1	Exp.	295	260	N.A.	40	177	103	320
	Anal.	295	260	**0.63**	40	*178*	103	*321*
	Anal.	295	260	0.99	40	*270*	103	*413*
DWA2	Exp.	295	260	N.A.	46	205	101	352
	Anal.	295	260	**0.63**	46	*204*	101	*351*
	Anal.	295	260	0.99	46	*311*	101	*458*
SWA	Exp.	295	260	N.A.	24	77	80	181
	Anal.	295	260	**0.22**	24	*76*	80	*180*

TABLE III. Analytic solution for specific WGW structures and node positions in comparison with experimental measurements: *Italic texts* – calculated values by node equation; **bold texts** – assumed to match the node positions; plain texts - measured.

Based on the determined α, the mole fraction of the gases in the gas plug can be specified as shown in TABLE IV.

Machining	T (K)	P_i (kPa)	H_2	N_2	O_2	$H_2O_{(g)}$	α
DWA	295	260	0.42	0.234	0.336	0.01	0.63
SWA	295	260	0.147	0.501	0.343	0.01	0.22

TABLE IV**.** Gas composition of bubbles predicted from node position.

As shown in TABLE IV, degassing considerably increases the mole fraction of

hydrogen, which greatly contributes to delaying the acoustic node formation because the speed of sound in hydrogen is much faster than other gasses (H_2~1320m/s, N_2~350m/s, O_2~330 m/s). Therefore the higher mole fraction of hydrogen raises the speed of sound in the gas plug. So, as found in the node equation, faster speed of sound in the gas plug increases the resonant length of the gas plug, resulting in a same amount of delay in acoustic node formation.

Additionally, the lengths of water plugs are found to increase when the water is degassed, which is of crucial advantage in the acoustic node delay. Faster gas/bubble absorption of degassed water can potentially promote water plugs to occupy more space in the capillary, contributing to the elongation of L_{w1}. Not only can the decreased concentration of dissolved gases in degassed water improve the gas absorption rate, but also the increased mole fraction of hydrogen which has about twice the diffusivity of nitrogen and oxygen, thereby increasing the average solubility into the water.

5. The effect of pressure on acoustic node formation

5.1. Pressure control vs. temperature control

The node equation finds more strategies to delay node formation, such as pressure and temperature. Increasing temperature could contribute to additional delay of the acoustic node formation, however, the highest practical temperature rise would be limited to at most 20-30K. About 10% improvements could be achieved by increasing temperatures up to 50-60˚C. Temperature rising also causes additional effects on viscosity, surface tension, and mole fraction of steam, making its effect on the node formation much more complicated.

Compared with temperature, pressure is much more sensitive to the node formation and causes fewer side effects; decreasing pressure down to 50kPa would result in twice as long delays in node formation. Decreasing pressure, however, causes a crucial problem which significantly attenuates its advantage; decreasing pressure can cause a degassing effect which promotes the dissolved gases in water to diffuse out more spontaneously, weakening the water circulation and reducing the lengths of water plugs. These problems are very critical against achieving favorable machining and against delaying the node formation.

On the contrary, increasing pressure can be a very effective way to verify the node equation. Because increasing pressure does not suffer from the degassing effect, the changes of node formation according to the pressure increments can be compared with those calculated by the node equation.

To control the pressure of the gas plug, the glass substrate is sealed with an air-tight pressure chamber connected to a custom-built pressure controller. The control of the outside pressure of the nanocapillary directly affects the internal pressure of the gas plug based on equation (19).

5.2. Experimental setup for pressure control

Fig. III. 10 shows brief schematics of the pressure control experiment. The custom-built pressure controller automatically controls the preset pressure of the pressure chamber with less than 0.5% error by a feed-back control algorithm. The pressure sensor used in the control system has 20-250kPa measurement range with less than 100Pa

sensing error. A normal syringe is used for the pressure chamber, air-tightly glued on the microscope cover slip. In the syringe tip an oil plug is injected to form a protective layer, which decreases air diffusion into or out of water in the pressure chamber.

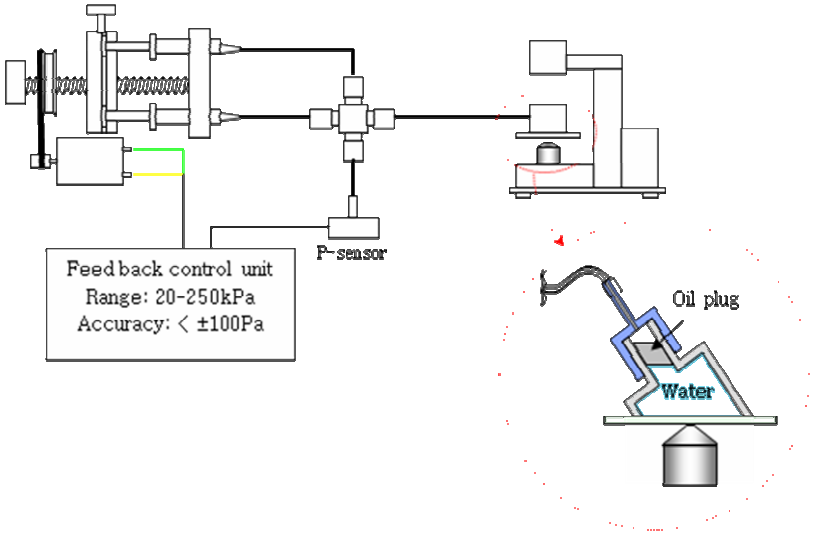

Fig. III. 10. Schematic of the pressure control experiment

5.3. Results

Although the pressure controller can cover a pressure range of 20 to 250kPa, the actual test range of pressure is set from 90 to 130kPa with 10kPa increments. Based on equation (19), the equivalent internal pressure of the gas plug varies from 250 to 290kPa.

With a 90kPa pressure setup, saturated water experienced a degassing problem which initiated ever-growing bubbles on the surface of the substrate and prevented the experiments from continuing. The experiments with degassed water could be performed without significant degassing problem. However, the pressure setups below 80kPa also caused similar degassing problems in the experiments using degassed water. The critical pressure causing the degassing problem will vary according to the degree of degassing.

The experimental results of pressure controls are shown in Fig. III. 11 along with the predictions of the node equation. In Fig. III. 11, it is clearly shown that the pressure increments cause the node to form earlier than that predicted by the node equation. Also, the magnitude of the change is in good agreement. The pressure control analyses further solidifies the validity and accuracy of the node equation.

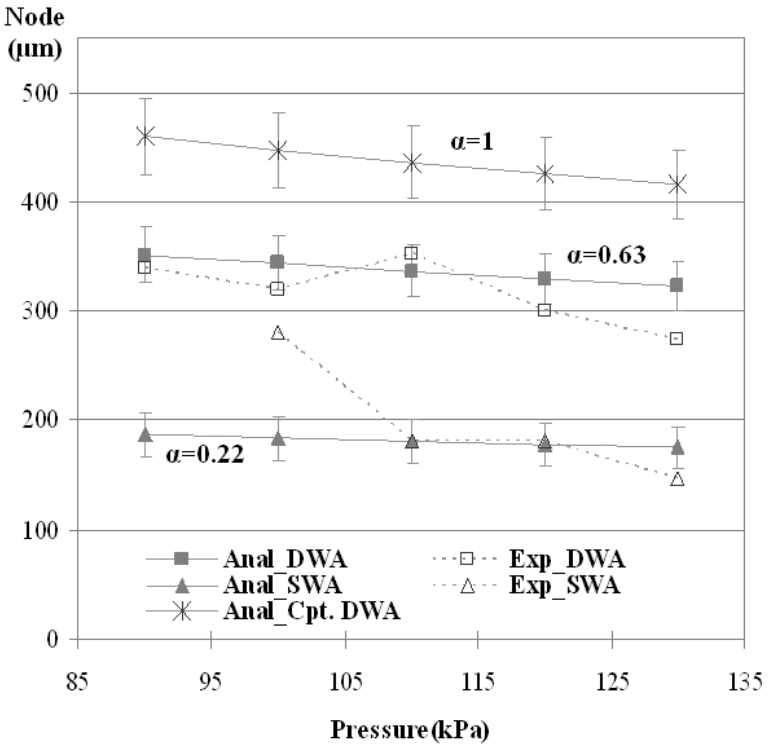

Fig. III. 11. Graphical results of pressure control

6. Discussion

A strong, previously unrecognized role of acoustic nodes during fs-laser-nanomachining has been characterized in chapter III. Experimental and theoretical description of these effects allows us to identify methods for machining high NCL channels, which are critical not only for fabricating a nanoscale separation column but also for developing complex lab-on-a-chip and micro-total analysis devices. Such devices are of broad interest for basic research and have far-reaching applications, but require 3-dimensional networks of high NCL channels to reach full potential for diagnostics, sensors, drug-discovery, microreactors, and chemical analyses such as capillary electrophoresis.

Understanding the role of acoustics during fs-laser-machining provides the basis to realize complex micro/nanofluidics with freedom to arbitrarily configure components in 3 dimensions. It also reveals the importance of parameters not generally considered in analyses of optical breakdown and laser machining, such as the pressure and resonant structures.

CHAPTER IV

3-DIMENSIONAL MICRO/NANOFLUIDIC DEVICES IN GLASS: NANO-CAPILLARY ELECTROPHORESIS

1. Introduction

Rapid chemical analyses using minimal sample volumes have broad implications for accelerating the development of drugs and other chemicals while minimizing costs, enabling new compact devices for diagnostics or field analyses, and enabling new capabilities in single cell analysis such as single cell proteomics using submicron-scale capillaries. In pharmaceutical biotechnology, speed, simplicity, and automation are key factors. Even in modern high-throughput screening (HTS) or high-content screening (HCS), brute-force analyses are essential to find "hits" or lead compounds out of millions of pharmaceutical tests, meaning that the drug-discovery process from lead compounds to pre-clinical tests can require very long times. Thus, rapid chemical analyses are of great importance to expedite the entire process. In biological samples, proteins, nucleic acids, and polysaccharides are often present in very small quantities and sample sizes are often limited, requiring that separation techniques be highly sensitive and selective while consuming very small sample volumes. Miniaturized, micro-column separation techniques, such as high performance liquid chromatography (HPLC), capillary gas chromatography (CGC), or capillary electrophoresis (CE), are particularly suitable for the detection of analytes in very small, submicroliter-size volumes. Small cross-sectional area capillaries are required for these currently available separation formats.

Although these modern separation techniques based on the capillary format achieve very high efficiency and resolution with great selectivity, multiple separation approaches are often required, especially for the analyses of complex biomolecules. For example, HPLC and CE, which are orthogonal in their separation mechanisms (hydrophobicity and charge-to-mass ratio, respectively), are often adopted in the analysis

of complex biomolecules. In addition, HPLC and CE share many important and advantageous features in their capillary formats in terms of fast analyses, minimal sample volumes, high resolution, and ease of (full) automation.

HPLC has undergone tremendous development in the past two decades, and CE technology is expected to achieve similar development. CE separation techniques were introduced in the 1960's with attention to the potential advantages of electrophoretic separations in the capillary format, such as fast analysis with high resolution. Moreover, electrophoretic techniques such as gel electrophoresis, micellar electrokinetic chromatography (MEKC), isoelectric focusing (IEF), and isotachophoresis (ITP), are all compatible with the capillary format. By simply filling gels, adding micelles, adding buffer additives, introducing special background electrolytes, or coating capillary walls, various modes of CE can be transferred to the capillary format, including capillary gel electrophoresis (CGE), micellar electrokinetic capillary chromatography (MECC), affinity capillary electrophoresis (ACE), capillary electrochromatography (CEC), capillary isoelectric focusing (CIEF), and capillary isotachophoresis (CITP). With these developments, separation power was expanded even to uncharged complex biomolecules with improved resolution and selectivity and CE became able to cover broad application fields including genomics, proteomics, drug-discovery, and carbohydrate analyses. Also, commercial CE instrumentation has been available since the 1980's, achieving automated DNA sequencing and genotyping for genome-level analyses [37-39].

CE can potentially exceed the efficiency and resolution of HPLC, which achieves plate numbers of several hundred thousand, by exploiting electrokinetically driven flows that form plug-like flat velocity profiles, minimize zone broadening, and achieve separation efficiencies close to that predicted theoretically. However, the electric fields driving CE separations are practically limited in strength due to Joule heating, whose adverse effects are: 1) increased zone broadening that diminishes separation efficiency and resolution, 2) bubble formation and/or boiling of the electrolytes, 3) changes of biological and electrochemical properties of the analytes, and 4) degradation of the analysis accuracy and reproducibility. Thus, modern CE instruments are designed to strictly regulate temperature changes with additional cooling devices that quickly

dissipate Joule heating in CE columns.

The Joule heating-induced temperature changes can be specified as both the temperature rise of the capillary (the average temperature of the capillary relative to the surroundings) and its internal radial temperature gradient (the temperature variation inside the capillary: capillary center is high and surface is low). Although external cooling is very effective in preventing temperature rises, it cannot regulate the radial temperature gradient. Thus, the maximum electric field strength is still limited. In addition, as heat generation increases, more massive cooling devices are needed to properly regulate the temperature rise.

Therefore, reducing heat generation is the radical solution to the Joule heating problem and has been one of the most important issues in CE techniques. One very effective way to reduce heat generation is introducing less conductive zwitterionic buffer solutions. However, salt-based highly conductive buffer solutions are sometimes essential. Reducing the cross-sectional area of the capillary column is a more fundamental method to reduce heat generation, as it is well known that heat generation is proportional to the cross-sectional area of the capillary bore. The main problem is that there are no commercially available submicron-scale capillaries, because reducing capillary bore size smaller than 10μm is technically limited. Another issue is that smaller capillaries are more prone to clogging.

This research uses optical machining by fs laser pulses to achieve submicron-scale separation columns (d=650±50nm) for a nanocapillary electrophoresis (nCE) device. After it was discovered that fs-laser-machining could perform far-field nanoablations [21-22], there has been significant progress in fabricating 3-dimensional subsurface nano-geometries using fs laser pulses [21-31]. Thereafter, 3-dimensional subsurface geometries were successfully fabricated with water-assisted fs-laser-nanomachining [28-31].

However, the major obstacle in fabricating submicron-scale separation columns was the challenge of increasing the capillary length. Direct fabrication of subsurface capillaries and channels is intrinsically limited in increasing NCL due to difficulties of debris extrusion. The NCL of any direct boring methods, including microdrilling and previous micron-scale fs-laser-machining, had been limited to 50 [36] despite NCL's of at

least several hundreds being essential for analytical separations. The newly discovered degassed-water-assisted fs-laser-machining method, along with an optimized repetitive machining algorithm [31], improved the achievable NCL of subsurface capillaries to higher than 1000. Thus, a submicron-scale separation column (d=650±50nm, L=804μm) for the nCE device could be successfully machined without using a cleanroom, complex bonding processes, or challenging multilayer lithography processes [34].

In theory, submicron-scale capillaries, with diameters more than 10 times smaller than those available commercially, can withstand electric field strengths up to 100kV/cm due to far less heat generation and faster heat dissipation. Such high electric fields approach the critical strength that can cause a dielectric breakdown of aqueous electrolytes. Thus, extremely high electric field strengths in the submicron-scale separation regime become one of the most discriminating features from the micron-scale separation regime.

The first result of extremely high electric field strength achieves is fast separations on the order of milliseconds. As described previously, the fast separations within the submicron-scale separation regime has huge potential to impact many fields including biotechnology, drug-discovery, and chemical analysis.

In addition, because the heating is nearly instantaneous during fast separations, the CE column temperature cannot significantly rise as it does for slow separations, which typically run at maximum equilibrium temperatures. Based on computer simulation of the transient heat transfer process, it is found that the heating for 1 second just raises the temperature of the capillary less than 20% of the maximum. Another advantage of fast separations is that external cooling devices are not necessary because the penetration depth of the thermal energy is shorter than the thickness of the device or the capillary. If miniaturized cooling devices can be provided, enhanced heat dissipation may decrease the waiting time between runs. This property is very advantageous for device simplicity and portability, and improves separation performance by reducing degradative processes, such as biomolecule denaturization.

The instantaneous heating advantage can also be exploited in the micron-scale separation regime, enabling the application of very high electric field strengths to micron-

scale separation columns as long as the heating time is sufficiently short. Millisecond-order fast separations using high electric field strengths up to 53kV/cm and very short separation lengths of 2mm have been successfully demonstrated with microchip-based separation columns [40-42].

Fast separations using micron-scale capillaries, however, have limited separation efficiencies, because very short separation columns must be used to sufficiently reduce the heating time. Considering that the electric field strength cannot be further increased due to the dielectric breakdown of the aqueous electrolytes, the only way to improve the separation efficiency is to increase the overall length of the separation column, which is substantially limited due to huge heat generation in the micron-scale separation column. Therefore, in the submicron-scale separation regime, where heat generation is at least 100 times less than that in the micron-scale separation regime, the separation efficiency can be further improved to achieve highly efficient, fast separations.

Downscaling to the submicron-scale separation regime also greatly reduces the required sample volumes by more than 4-5 orders of magnitude compared with the micron-scale regime. The injection volumes range from 1 to 10fl, where the number of analytes can be as small as zeptomoles (10^{-21} moles). The direct separation of 1fl sample volumes demonstrates unprecedented ability, with potentially huge impact, especially in single cell analysis. However, to achieve a complete 1fl separation, an appropriate loading mechanism capable of loading exactly 1fl without sample waste is required. Continuous flow sample loading mechanisms, which are widely used in the microfluidic separation devices, are not appropriate for loading such small volumes without waste. To achieve precise loading of the 1fl sample volume, a zero-flow sample loading method is developed based on the dielectric breakdown of a thin nano-glass layer, which works like an electrode and generates pressure driven sample loading. This method achieves direct sample loading of femtoliter volumes without additional sample waste because there is no continuous sample flow to the waste reservoir. Also, the volume or length of a sample plug can be continuously controlled by loading time (14fl/s sample loading rate), which is very important in precisely loading diverse samples, such as organelles in the cell, and to achieve optimal injection volumes according to the separation conditions. Sample

volumes that are too small can lose signal intensity, making detection very difficult. Likewise, volumes that are too large diminish the separation efficiency and resolution.

These discriminating features of the submicron-scale separation regime can be demonstrated with a test separation using the developed nCE device, and numerical calculation of the transient heat transfer characteristics of the separation column. The expected performance of submicron-scale separation with the nCE device can be extrapolated from operation with relatively low electric field strength of 440V/cm. For example, if an electric field of 53kV/cm is used, extrapolation predicts an average migration time of 6.3ms, a plate number of 85,000, and a maximum local temperature rise of 8.4K. While the injection sample volume of 9fl is already very small (equivalent to about 400 zepto-moles or 240,000 molecules with 40μM concentrations), 1-2fl sample volumes are found to be more appropriate for the application of higher electric field strengths up to 100kV/cm.

The submicron-scale separation regime is not meant to include all current CE applications, but instead focuses on new application fields where either the sample volumes are much too limited for current separation techniques like single cell analysis, or extremely fast separations are of great importance. While clogging and solute adsorption in the extremely small capillary bore size are potential problems, developing processes such as pre-filtrations will be important.

Nevertheless, the discriminating advantages of the submicron-scale separation regime are highly expected to accelerate the development of new application fields such as single cell analysis and other technologies related to lab-in-a-cell (LIC) methodology. The developed submicron-scale separation column will best achieve 1fl sample analysis of intracellular cytoplasm, single organelle lysate, ion channel proteins, signaling biomolecules and nucleic acids. Also, a continuous flow cytometry based on the submicron-scale capillary might be combined with CE separation to analyze the structure of individual proteins following separations. The newly found phenomenon of current-controlled dielectric breakdown of a thin nanoscale glass wall can be exploited to perform liquid control based on pressure driven flows. As shown in the zero-flow sample

loading method, a submicron-size EK pump for extracting intracellular materials such as cytoplasm, organelles, and nucleic acids is expected to play the key role where electric fields are not appropriate to drive these intracellular materials.

2. Principal parameters for capillary electrophoresis

Primary parameters for characterizing CE separations are resolution, migration time, and efficiency; for an in-depth discussion see [43, 44]. Assuming Gaussian concentration distributions, zone broadening (W) can be characterized by the variance σ^2, as shown in Fig. IV. 1.

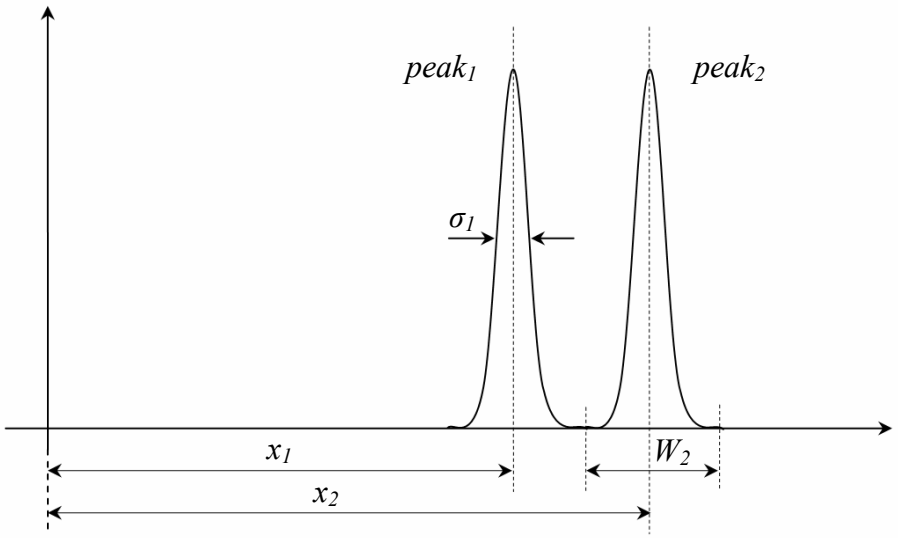

Fig. IV. 1. Two neighboring concentration peaks on electropherogram.

Diffusion and the initial length of the sample plug are two main contributors to zone broadening in CE separations. For simplicity, the other minor factors are neglected, as shown in equation (23). Here, l_{inj} is the injection length.

$$\sigma^2 = \sigma_{diff}^2 + \sigma_{inj}^2 + \sigma_{geo}^2 + \sigma_{th}^2 + \cdots \approx \sigma_{diff}^2 + \sigma_{inj}^2 = 2Dt + \frac{l_{inj}^2}{16} \tag{23}$$

$$W \approx 4\sigma \approx 4\sqrt{2Dt + \frac{l_{inj}^2}{16}} \tag{24}$$

Resolution (R_s) is a measure of sample zone separation (x_2-x_1) relative to the zone widths (W); it can be defined either for the time or spatial domain. The spatially defined resolution is shown in equation (25); $\Delta\mu_{ep}$ is the difference in electrophoretic mobility of two separated bands, E is the electric field strength, and N is the plate number.

$$R_s = \frac{x_2 - x_1}{\overline{W}} = \frac{\Delta\mu_{ep} E}{(W_1 + W_2)/2} t \approx \frac{1}{4} \frac{\Delta\mu_{ep}}{\overline{\mu_{ep}}} \sqrt{N} \tag{25}$$

As shown in equation (25), resolution is also related to efficiency, which is measured by the plate number (N). Here, L is the length of the separation column to the detection area.

$$N = \frac{L^2}{\sigma^2} \approx \frac{L^2}{2Dt + l_{inj}^2 / 16} \tag{26}$$

The theoretically achievable maximum plate number (N_t) considers zone broadening only by diffusion.

$$N_t = \frac{L^2}{2Dt} = \frac{\mu V}{2D} \tag{27}$$

The efficiency can also be expressed by the plate height (H);

$$H = \frac{L}{N} = \frac{\sigma^2}{L} \tag{28}$$

The number of resolvable peaks (n_c), which is also related to the plate number, measures how many peaks can be resolved with the capillary.

$$n_c = \frac{L}{W} \approx \frac{\sqrt{N}}{4} \tag{29}$$

The separation time (t_{sp}) measures how long any two concentration peaks take to become resolvable (R_s=0.5), whereas the migration time (t_m) is the average time required for analytes to reach the detector; $\bar{U}$ is the average migration speed of the analytes. The migration time is analogous to the retention time, which is a fundamental term in chromatography.

$$t_{sp} = \frac{8D}{(\Delta\mu_{ep})^2 E^2} \tag{30}$$

$$t_m = \frac{L}{\bar{U}} = \frac{L}{\bar{\mu} E} \tag{31}$$

3. Design and fabrication of nCE device

3.1. nCE separation column design

The separation column geometry of the nCE device is an outer-weighted spiral, as shown in Fig. IV. 2. A 804μm long capillary with 650±50nm diameter is fabricated using degassed-water-assisted fs-laser-machining. A rectilinear separation column would best minimize the zone broadening, however the spiral shape separation column also has several advantages: 1) longer capillaries than the travel range of the linear nanostage can be fabricated, 2) higher device density can be achieved, and 3) the entire separation process, including sample loading, sample migration, and detection, can be more easily observed with the same view.

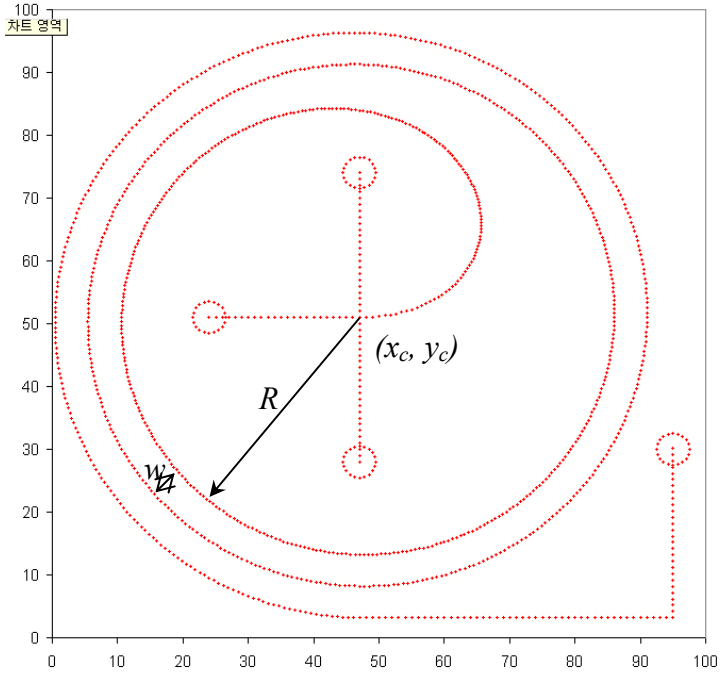

Fig. IV. 2. nCE separation column design.

$$x = 10^3(1-A^t)(R+0.002792wt)\cos(\pi t/180)+x_c$$
$$y = 10^3(1-A^t)(R+0.002792wt)\sin(\pi t/180)+y_c \quad (32)$$

The linear nanostage, which has a travel range of 100μm at each axis, can successfully fabricate the 804μm long separation column by incorporating 2.75 turns of the spiral shape column design, as shown in Fig. IV. 2. The exact equation for the spiral is

given in equation (32); A is a shape factor determining the curvature of the initial part of the column (A=0.97), R is the initial radius of the spiral (R=32μm), w is the distance between tracks (w=5μm), (x_c, y_c) is the center of the spiral where the loading and the separation columns cross each other, and t is the angle varying from 0˚to 990˚.

The essence and convenience of 3-dimensional configurations are evident with a schematic of the nCE nano-capillaries, shown in Fig. IV. 3. With 2-dimensional configurations, it would be almost impossible to cross the loading and the separation columns only at the center.

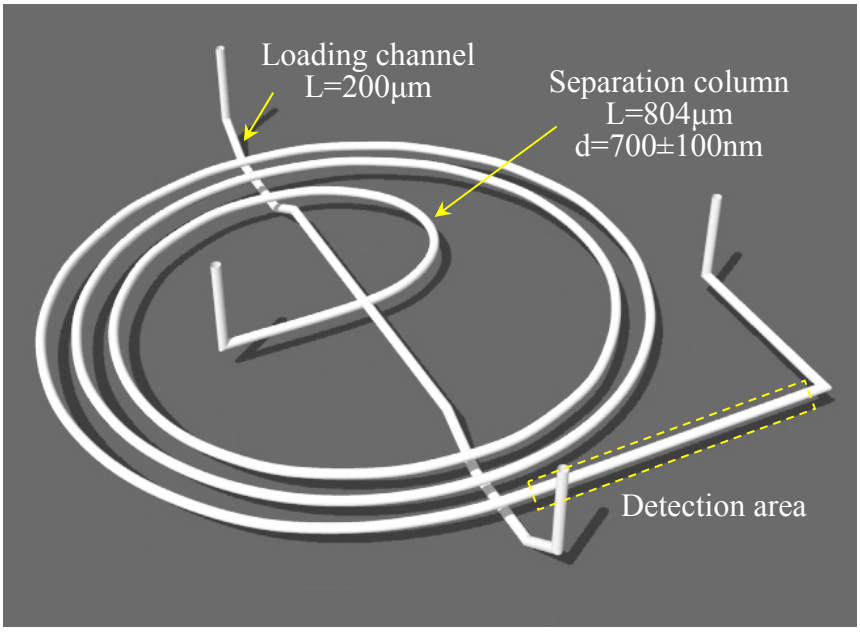

Fig. IV. 3. Three-dimensional schematic of the nCE separation column and loading channel.

The actual nCE separation column and loading channel are shown in Fig. IV. 4, and compared with a scanning electron microscopy (SEM) image of human hair. The upper and lower parts of the loading channel appear thicker than other parts, because they are 5μm deeper.

The machining time of the separation column is on average 4 hours. The average yield-rate is about 50%, with 3-4 successful fabrications out of 7 trials.

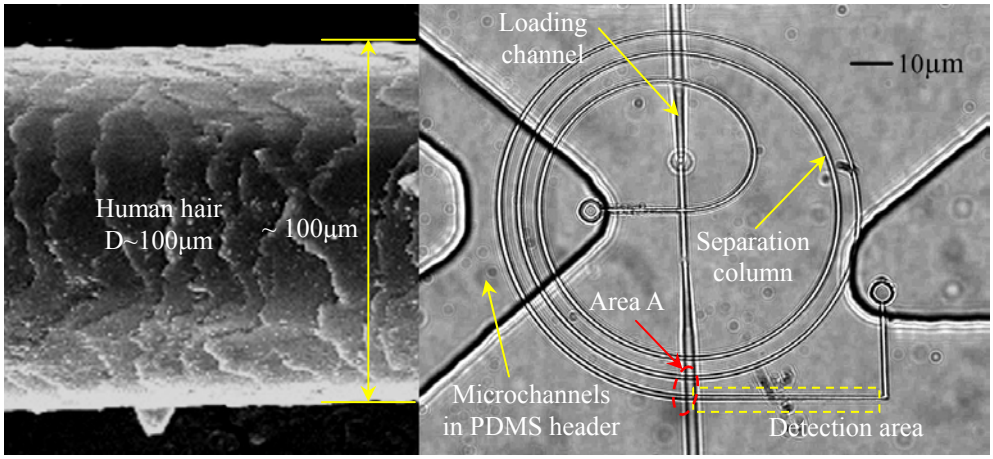

Fig. IV. 4. Microscopic image of nCE device and SEM image of human hair.

The yield-rate of the separation column is primarily affected by z-axis drifts and laser instabilities. First, mechanical back-lash of the objective lens elevator in the microscope can cause z-axis drift, especially for extended-duration processing. Also, the daily atmospheric pressure fluctuations are found to deform the air-tight sealed substrate up to 2μm, which is enough to induce machining failure. Finally, the instability of the laser beams also becomes critical, especially while processing for an extended time.

3.2. PDMS header design

The nCE device is composed of two layers: 1) a PDMS header layer and 2) a glass layer (microscope cover slip) containing the separation column and loading channel. The function of the PDMS header is to introduce fluids and sample solutions to the nanocapillaries, which are too small and too closely located to each other for direct sample fluid introduction.

Although glass is better for the header layer (as far as the material for the prototype nCE device is concerned), PDMS is also sufficient and has many advantages. PDMS is much easier to duplicate and assemble than glass, and is also able to withstand relatively low electrical field strengths and internal pressures.

The mask for the PDMS header layer is designed using the commercial software, “CleWin” (WieWeb software, www.wieweb.com), as shown in Fig. IV. 5. The vertexes of the four V-shaped microchannels are connected to the four outlets of the separation and the loading columns, which ensures bubble-free fluid introduction.

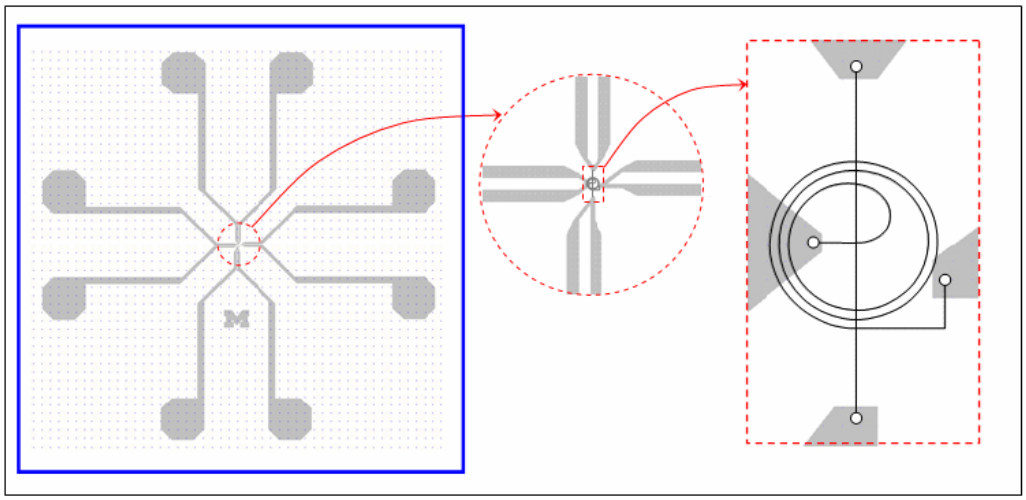

Fig. IV. 5. Mask design of PDMS header layer and magnified center area where the nanocapillaries are machined.

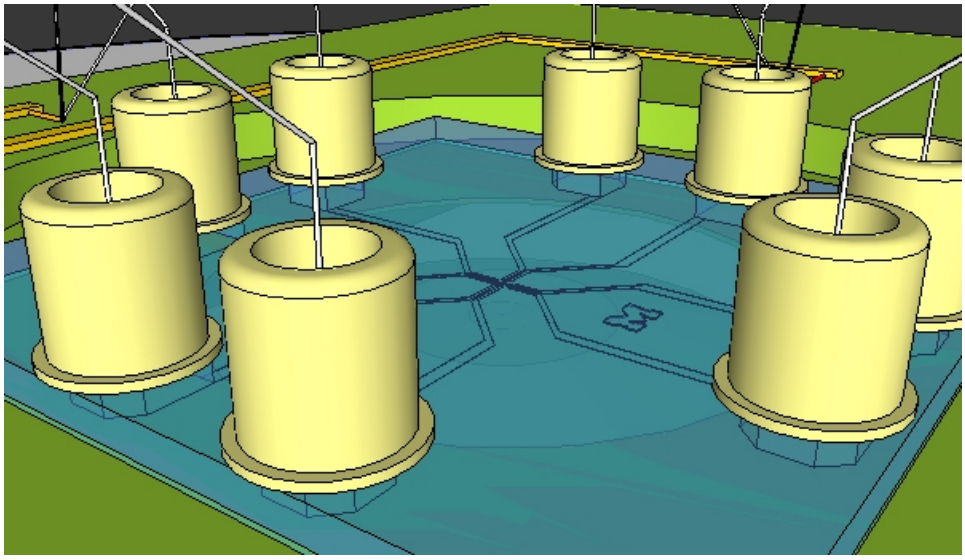

Fig. IV. 6. PDMS header layer with sample reservoirs and electrodes.

As shown in Fig. IV. 6, external reservoirs are placed at the upper part of the PDMS header layer with the electrode configuration. The cross-sectional area of the microchannels in the PDMS header is on average 1000 times larger than that of the nano-capillaries, resulting in more than 99% of the total potential being applied to the nano-capillaries. Thus, voltage drops at the microchannels in the PDMS header are almost negligible.

3.3. Electrokinetic operation

From the equivalent circuit of the nCE device (Fig. IV. 7) the electric field along the separation column is given by equation (33);

$$E = \left(0.995 \times \frac{13}{14} \times (V_T - 1.2) \right) \times \frac{1}{L} \tag{33}$$

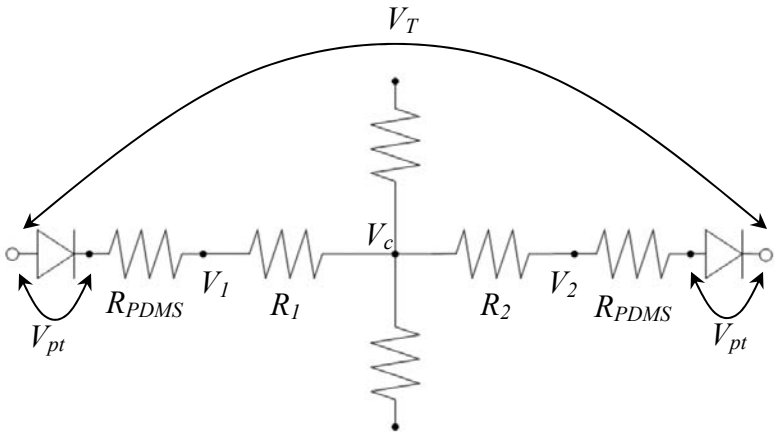

Fig. IV. 7. Equivalent circuit diagram for the nCE device.

The electric field in the separation column is calculated based on the potential over R_2 (=V_c-V_2) and the length of the separation column (L=780μm). Due to a voltage drop of 0.6V at each platinum electrode (V_{pt}), V_T-1.2 is actually applied to the nCE device. The electrical resistance of the separation column (R_1 + R_2) is about 200 times larger than that of the microchannels in the PDMS header ($2R_{PDMS}$); thus, 99.5% of the potential (V_T-1.2) is applied to the separation column. Finally, the voltage ratio between R_1 and R_2 is found to be 1:13, which yields equation (33).

4. Sample loading in submicron-scale separation column

4.1. Zero-flow sample loading method for minimum sample waste

In microchip-based separation devices, sample loading using continuous sample flow from a sample reservoir to a waste chamber is widely used to generate small injection plugs to the separation column, as shown in Fig. IV. 8. This loading mechanism achieves very accurately sized injection plugs and minimizes contamination of the separation column. However, this injection method is wasteful due to continuous sample flow to the waste reservoir.

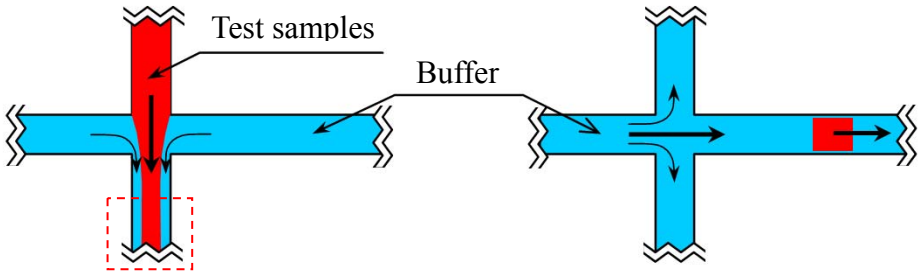

(a) Control of loading (b) Control of separation

Fig. IV. 8. Loading mechanism based on continuous sample flows.

These small sample waste volumes (~ μl/s) would be negligible in many cases and acceptable when sufficient quantity of test sample is available. However, minimizing the sample waste can enable analysis of very small volumes and very sparse samples, including applications for individual cell analysis and drug-discovery.

In this research, the zero-flow sample loading mechanism ("zero-flow" refers to no continuous sample flow to the waste reservoir) is developed and used to successfully load 9fl test sample volumes in nCE separation experiments without additional sample waste. The sample injection volume can be controlled by varying the loading time. The measured sample loading rate is 14fl/s, which is also controllable.

The zero-flow sample loading mechanism is analogous to that used in electrokinetic pumping. The key feature in this loading method is the dielectric breakdown of a thin nanoscale glass wall, causing the glass wall to act like an electrode. Dielectric breakdown can happen when the electric field strength exceeds a critical value, which for glass is about 14MV/m. Considering a 1μm thick glass wall requires only 14V to reach the critical electric field strength, the dielectric breakdown of the thin glass wall

in area B (as shown in Fig. IV. 9), which is thinner than 1 μm, can be induced by potentials smaller than 14V.

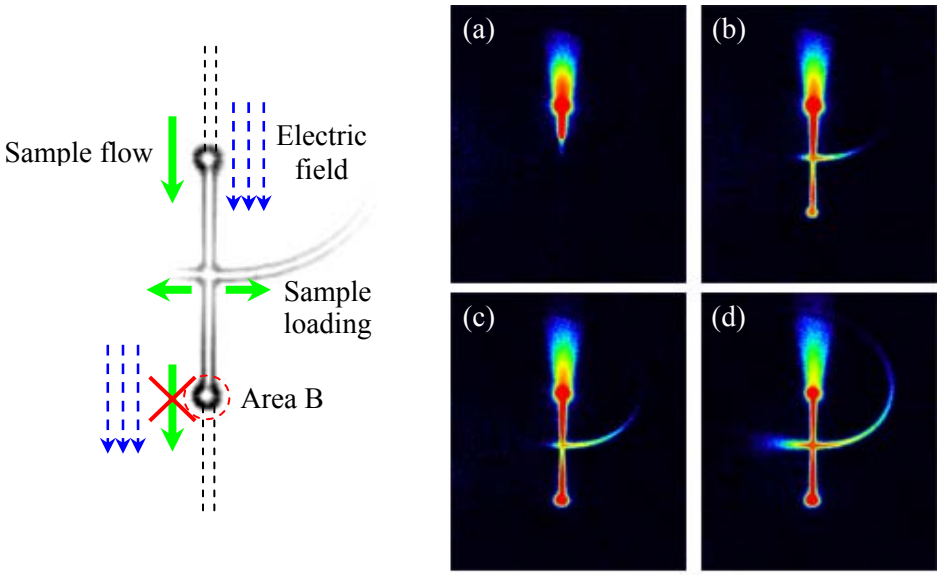

Fig. IV. 9. Zero-flow sample loading mechanism.

As shown in Fig. IV. 9 (a), the sample solution does not initially migrate downstream because area B is the dead-end of the loading channel. After about 1.5 seconds, the analytes start to quickly migrate downstream, filling the center part of the loading channel as shown in part (b) of the figure. This indicates that the electric fields are suddenly present, driving the analytes toward the closed cathode (the dead-end glass wall). Because of the blockage, electroosmotic flow (EOF) builds up pressure, which induces back-flow upstream; in this situation EOF runs along the wall surface and pressure driven flow (PDF) runs along the center of the channel.

The pressure buildup pushes most of the sample to the separation column, where the counter flow due to EOF is weaker than that in the loading channel. As illustrated in the Fig. IV. 8 (a), relatively weak EOF downstream of the loading channel is configured to prevent contamination of the separation column during the loading process. In parts (c) and (d) of the figure, it is evident that the sample flowing along the separation column is driven by pressure; the sharp leading edge shows the flow is stronger at the center of the channel.

The zero-flow sample loading mechanism also indicates that the dielectric

breakdown does not cause material damage of the thin glass wall, but simply converts the glass wall to a conductor. Material damage occurs when the dielectric breakdown strips off valence electrons, resulting in instantaneous bursts of electric currents. However, this is very difficult to achieve in the submicron-scale loading channel because the nanocapillaries have gigaohm-range electrical resistances, thereby allowing electrical current of merely a few nanoamperes. A large resistor can be used to regulate currents and limit current bursts. Likewise, the huge internal electrical resistance of the nanocapillary controls the current, preventing current bursts. Thus, current-controlled dielectric breakdown (CCDB) at the thin glass wall can successfully generate electric fields without significant material damage, leading to EOF and pressure driven sample loading during the zero-flow sample loading process.

4.2. Effect of initial sample plug length on separation speed

The length of the injected sample plug, along with diffusion, are the major parameters affecting zone broadening (see equation (24)). Thus, longer injection lengths diminish separation efficiency, while increasing the signal intensity measured at the detection area. So, careful control of the injection length is very important, especially in fast separations.

Generally, slow separations (>1s) require more fluorophores because diffusion broadens the sample plug, weakening signal intensity at the detection area. Therefore, slow separations require either higher solute concentrations or longer injection plugs. Interestingly, in slow separations the injection length has less effect on zone broadening or efficiency than in fast separations, diminishing the importance of optimizing the injection length.

This does not mean that slow separations do not require injection length optimization, but implies that control of the injection length for optimum loading conditions becomes more critical for fast separations

Zone broadening of two different length injection plugs (1μm and 10μm; 1s migration) can be compared using equation (24). Assuming a 1μm long injection plug has 10 times higher solute concentration than the 10μm long injection plug, the lengths

become 178.8μm and 179.1μm, respectively due to zone broadening after 1 second. Zone broadening after 1s reduces the length difference from initially 9μm to 0.3μm, such that these two bands are nearly identical. For times > 1 second, these two bands become identical, and the effect of injection length is negligible.

Mathematically, zone broadening is the square root of the sum of each factor shown in equation (24). These characteristics are considered to work positively toward a Gaussian distribution of the zone.

Fig. IV. 10 shows more detailed effect of injection length on zone broadening, and the corresponding plate number as a function of migration time.

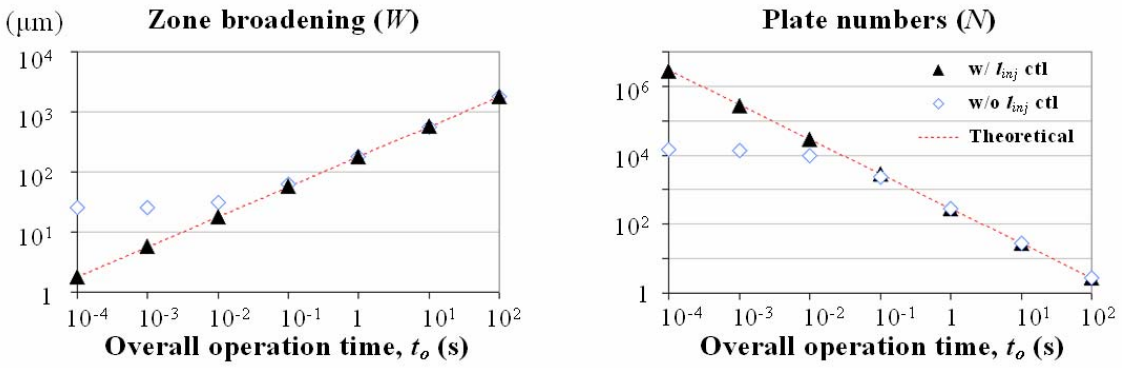

Fig. IV. 10. The effects of injection plug length on zone broadening and the corresponding plate number as a function of migration time.

As shown with empty diamonds in Fig. IV. 10, a 25μm long injection plug prevents further increases in separation efficiency and further reductions in zone broadening for separation times < 1s. Therefore, in the fast separation regime (<1s), the injection length needs to be reduced. The solid triangles represent reduced injection lengths based on the control rules, which are explained in detail in the next section (4.3.).

Although in the slow separation regime the effect of the injection length becomes negligible, this observation does not necessarily imply that slow separation is more advantageous in reducing zone broadening, but rather signifies that the effect of diffusion becomes substantial enough such that injection length effects can be ignored. This is clearly shown in Fig. IV. 10, where the plate number proportionally decreases with increased migration time, and the uncontrolled injection length merely prevents the plate number from further increasing in the fast separation regime.

In addition, slow separations require either longer sample injection lengths or higher solute concentrations to maintain sufficient detection intensity due to a weakening signal. Thus, ultimately any loading processes require control over the injection length to achieve optimum loading conditions.

4.3. Control of initial length of injection sample plug

Too small of an injection plug causes problems at the detection due to significant signal weakening; thus, the injection plug should be larger than a minimum length, which varies according to several parameters including the concentration of the sample solution, diffusivity, and migration time. Equation (34) uses fluorescent intensity instead of the sample concentration; I_o is the initial signal intensity of the injection sample plug, I_{min} is a minimum signal intensity for detection, t_m is migration time and D' is the newly formulated constant simplifying the equation

$$l_{inj} \geq 4\sqrt{\frac{2Dt_m}{\left(I_o / I_{\min}\right)^2 - 1}} = 4\sqrt{2D't_m} \tag{34}$$

In equation (34), the minimum l_{inj} is proportional to the square root of the migration time. Thus, a 100x electric field can reduce l_{inj} 10 times without signal weakening. Also, the I_o/I_{min} or D' terms reveal that the sensitivity of a detector contributes to further minimization of l_{inj}. Based on equation (24) and (34), the minimum band broadening can be calculated as shown in equation (35);

$$W \geq 4\sqrt{2(D + D')t_m} \tag{35}$$

Also, the effects of l_{inj} on band broadening directly affect the efficiency and resolution. Calculating N for fast separations should also consider l_{inj} based on equation (26) and (34), yielding equation (36).

$$N \leq \frac{L^2}{2(D + D')t_m} \tag{36}$$

Equation (36) indicates that the maximum separation efficiency is dependent upon the injection length, and its effect increases with decreasing separation time. Therefore, the ability to continuously control the injection length of the sample plug is highly

requested, especially for fast separations. Thus, the developed zero-flow sample loading method is important not only in minimizing sample waste, but also in achieving higher resolution and efficiency based on the ability to continuously control l_{inj}.

5. Heat transfer analysis of fast separations

5.1. Advantages of submicron-scale fast separations

The three major advantages of submicron-scale fast separations, with regard to heat transfer, are less heat generation, fast heat dissipation, and instantaneous heating. Under the same electric field strength, smaller bore capillaries generate less heat and dissipate it faster; as a result, higher electric field strength can be withstood. In theory, the submicron-scale separation column can withstand electric field strengths up to 100kV/cm, which is extremely high and approaches the critical strength that causes dielectric breakdown of the electrolytes. Therefore, regardless of the Joule heating, further increasing of the electric field strength is limited.

The effects of Joule heating and heat dissipation rate on the temperature of the separation column can be specified with the temperature rise (the average temperature rise of the capillary relative to the surroundings), and the radial temperature gradient in the capillary (the temperature difference between the center and surface of the capillary). Either measure does not necessarily determine the other.

The temperature rise and radial temperature gradient are both proportional to heat generation, and are determined by the external and internal thermal resistances, respectively. The external thermal resistance can be reduced by increasing the external cooling rate, as liquid cooling devices are used in many commercial CE instruments. Decreasing the temperature rise is very important in diminishing adverse effects such as boiling of the electrolyte solution, bubble formation, and increasing diffusivity. In addition, although external cooling devices complicate the system, they remain necessary for precise CE analysis because uncontrolled temperature changes degrade analysis accuracy and reproducibility.

The radial temperature gradient, which causes biological and electrochemical property changes of the analytes and an increase in zone broadening due to the velocity gradient, is determined by the internal thermal resistance of the capillary, as shown in equation (37). W is power, r is the capillary radius, and k_{th} is the thermal conductivity.

$$\Delta T \approx 0.06 \frac{W r^2}{k_{th}} \propto \frac{r^4}{k_{th}} \tag{37}$$

As shown in equation (37), the radial temperature gradient can be reduced by

reducing Joule heating, introducing a buffer solution with higher thermal conductivity, or reducing capillary bore size. Note that external cooling has no effect on the radial temperature gradient. Among these methods, reducing capillary bore size is by far the most effective means because the temperature gradient is proportional to the square of the bore size. Reducing bore size also reduces Joule heating under the same electric field strength. In all the radial temperature gradient is proportional to the 4^{th} power of the bore radius.

Another critical feature of submicron-scale fast separations is instantaneous heating. During millisecond-order fast separations, temperature increases are substantially limited. In this research, theoretical and numerical approaches are performed to evaluate the actual temperature rise (ΔT_{act}) and the gradient (T'_{act}) during instantaneous heating; experimental measurements are practically very difficult to obtain.

To distinguish instantaneous heating from steady state heating, the characteristic time constant of the system (the capillary) should be evaluated. A numerical analysis is performed not only to calculate the temperature rise and gradient, but also to evaluate the characteristic time constant of the system. Also, the theoretical approach, which is limited in accurately evaluating any practical numbers, elucidates how the major parameters such as heat generation, heat capacitance, and thermal resistance affect the temperature rise and the characteristic time constant of the system.

The numerical analysis finds another advantage of submicron-scale fast separations in that the thermal penetration depth is shorter than or comparable with the device thickness. As a result of the instantaneous heating, the thermal energy dissipation does not yet reach the device surface. This observation is very advantageous in that external cooling devices are not necessary. However, with minimally-sized external cooling devices, the waiting time between runs can be reduced.

5.2. Simple theoretical approach

Based on a simplified heat transfer model using the lumped capacitance method [46: chapter 5, page 226-355] for transient heat transfer in a CE separation column, a simple first order differential equation for the transient heat transfer can be established, as shown in equation (38):

$$C_{th}\frac{dT}{dt} = \dot{Q} - \frac{\Delta T}{R_{th}} \tag{38}$$

where C_{th} is the thermal capacitance of the separation column, $\dot{Q}$ is the total heat generation, and R_{th} is the thermal resistance across the substrate. This method assumes the temperature gradient across the separation column is negligible, although it could be substantial.

The simple first order ordinary differential equation yields the general solution given in equation (39):

$$\Delta T = R_{th}\dot{Q}(1 - e^{-\frac{t}{R_{th}C_{th}}}) \tag{39}$$

As shown in the general solution, the maximum steady state temperature rise (ΔT_{max}) is $R_{th}\dot{Q}$ and the characteristic time constant of the temperature rise (τ) of the system is $R_{th}C_{th}$; thus, the heat transfer characteristics can be described by these three parameters of R_{th}, C_{th}, and $\dot{Q}$. Also, the actual temperature rise (ΔT_{act}) can be described by ΔT_{max}, t_m and τ, as shown in equation (40).

$$\Delta T_{act} = \Delta T_{\max}(1 - e^{-\frac{t_m}{\tau}}) \tag{40}$$

$$\frac{\Delta T_{act}}{\Delta T_{\max}} = 1 - e^{-\frac{t_m}{\tau}} \tag{41}$$

Here, the ratio of $\Delta T_{act}/\Delta T_{max}$ or t_m/τ can be specified to determine the temporal behavior of the heat transfer, as shown in equation (41). This term determines the effect of separation speed on temperature rise. So, finding τ of the device is very important to evaluate the heat transfer characteristics of the system.

While the theoretical analysis is useful to characterize the heat transfer of the system, a numerical analysis is needed to quantify the transient heat transfer characteristics of fast separations with reasonable accuracy.

5.3. Numerical analysis

A numerical analysis of transient heat transfer within the nCE device was performed using commercial software (FlexPDE: linear and nonlinear PDE solver using finite element analysis), assuming an infinite rectilinear separation column. The infinite rectilinear column shape further simplifies the calculation of 3-dimensional structures such that they are performed in the 2-dimensional domain because of symmetry. This assumption leads to the calculation of numerical results that are slightly higher than the actual temperature due to 3-dimensional effects at the ends of the actual finite separation column.

The governing equation for the numerical analysis is shown in equation (42);

$$\rho c_p \frac{\partial T}{\partial t} - \vec{\nabla} \cdot (k \vec{\nabla} T) = q \tag{42}$$

This equation eliminates the convective heat transfer term for simplifying the calculation, however this simplification does not mean the convective term is negligible. Because the fluid convection is assumed to be 1-dimensional flow from the inlet to the exit of the separation column, the actual temperature profile of the capillary, including the convective heat transfer term, can be approximately conjectured. The temperature of the capillary is different at every axial location, and increases almost linearly from the inlet to the detection area. The temperature of the inlet will remain equivalent to the initial temperature, and the numerically calculated temperature based on equation (42) is the temperature at the detection area (the local maximum). Thus, the average temperature of the capillary is approximately half the temperature calculated numerically with equation (42).

The entire domain (one fourth of the substrate) is divided into three parts to further analyze the effects of high conductivity substrates such as quartz and diamond, as shown in Fig. IV. 11 with the separation column at the center (yellow), the core substrate next to the separation column (green), and the outer substrate (blue). Because the geometry is symmetric, one fourth of the entire cross-section is numerically calculated.

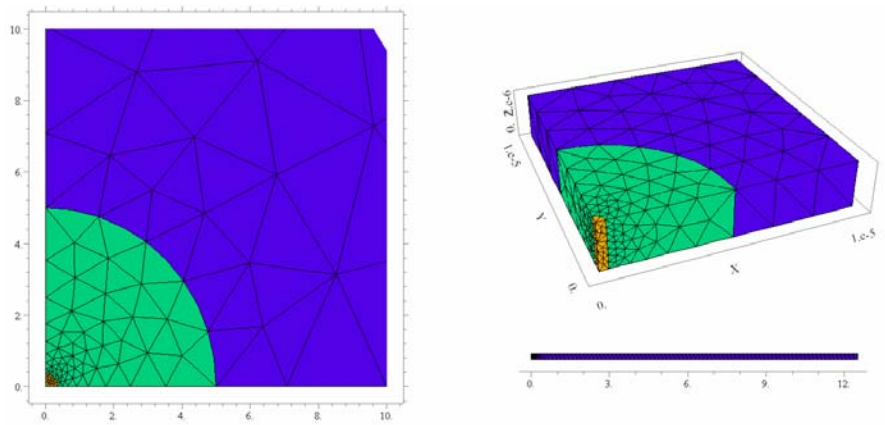

Fig. IV. 11. Mesh design of one fourth of microscope cover slip substrate cross section.

The entire thermal resistance, R_{th} can be specified with three terms: the thermal resistance in the capillary, the thermal resistance of the substrate, and the thermal resistance of the external convection, as shown in equation (43).

$$R_{th} = R_{th}^{capillary} + R_{th\_conduction}^{substrate} + R_{th\_convection}^{external} \tag{43}$$

The thermal resistance in the capillary determines the radial temperature gradient (see equation (37)), whereas the other two terms primarily determine the temperature rise. The latter resistances are governed by the thermal conductivity of the substrate (k_{th}) and convection coefficient (h) of external cooling.

Without an external cooling device, cooling depends on natural convection and the external thermal resistance is the most significant term. Thus, regardless of the system complexity, external cooling is required for precise CE instruments. However, the numerical analysis found that, in the fast separation regime, the instantaneously localized heat transfer is not affected by the external thermal resistance. Because of the short penetration depth, the temperature rise is localized within the substrate. Thus, this instantaneously localized heat transfer in the fast separation regime does not require external cooling, and the total thermal resistance without external cooling is smaller than that in the steady state separation regime with external cooling.

To decrease the instantaneously localized thermal resistance in the fast separation regime, other transparent substrates having higher thermal conductivity could be used. Among the transparent materials, diamond (k_{th}=2300W/mK, type II-a) and quartz (k_{th}=6-10W/mK, crystalline) have much higher k_{th} than glass (k_{th}=1.4W/mK). So, based on the

divided mesh domain, composite substrates made out of these materials are also numerically evaluated so as to optimize the material property.

Numerical results for transient heat transfer characteristics of the nCE device are shown in Fig. IV. 12.

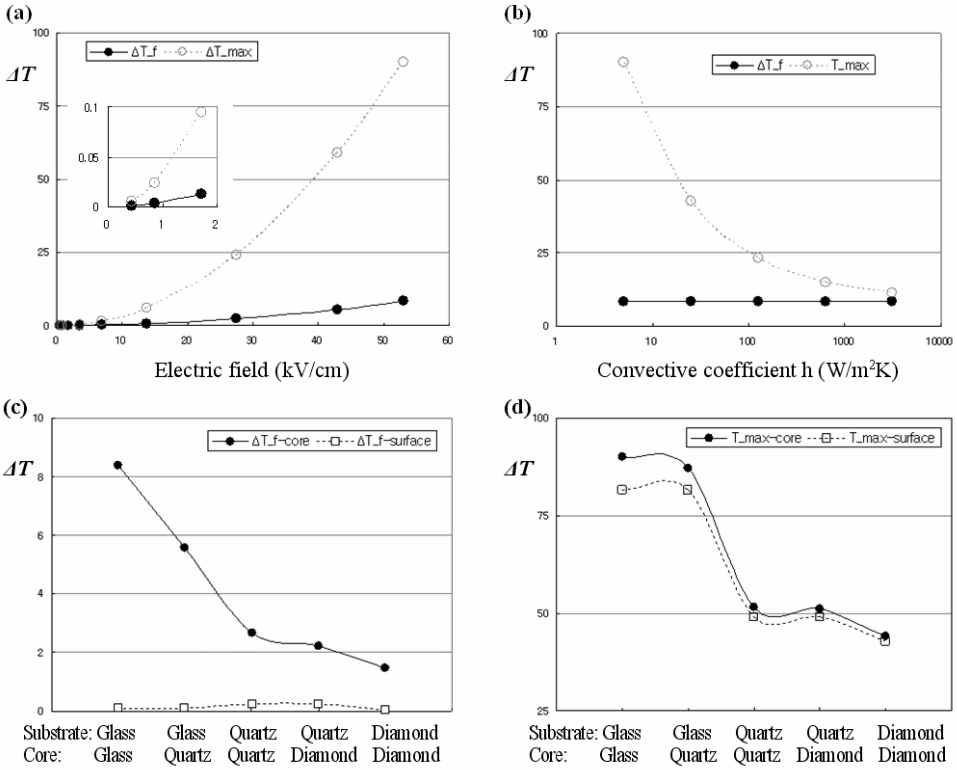

Fig. IV. 12. Numerical results of the transient heat transfer characteristics in the nCE device.

Fig. IV. 12 (a) shows that the actual temperature rise of the fast separation is far smaller than the steady-state maxima; $\Delta T_{act}/\Delta T_{max}$ decreases from 0.2 to 0.09 as the electric field increases from 430V/cm to 53kV/cm. Graph (b) shows the behavior of the instantaneously localized temperature rise. Because the temperature of the device surface is still nearly the same as the surroundings, which also means the external thermal resistance is nearly zero, the external cooling is neither effective nor necessary at all. After the separation is done, the external cooling, however, can more quickly dissipate this instantaneously localized thermal energy, reducing the waiting time between each run.

Fig. IV. 12 (c) and (d) show that high conductivity materials are very effective on both the transient (c) and the steady state heat transfer (d). An interesting result is that diamond achieves only slight improvements compared with quartz, whereas quartz makes distinguishable improvements over the glass as shown in Fig. IV. 12 (c). Although diamond has about 200 times higher k_{th} than quartz, the thermal resistance of the solution in the capillary becomes dominant, significantly limiting further improvements made by the diamond. Thus, quartz is the optimum substrate considering cost and effectiveness.

The numerically calculated τ of the temperature rise in the nCE device is about 30s, and that of the commercial capillary having outer diameter of 500μm is about 50s under natural convection. However, the characteristic time constant of the temperature gradient in the nCE separation column is on the order of microseconds. This result implies that the heat dissipation inside the submicron-scale capillary is very fast, minimizing the radial temperature gradient; the steady state temperature difference across the nCE separation column radius under 53kV/cm electric field strength is 1.43K.

Based on this numerical analysis, the thermal penetration depth becomes 1mm for 1s separation time. So, a device having 1mm thickness can instantaneously localize the thermal energy within the device for 1s, eliminating the need for external cooling. Therefore, based on the criterion of the fast separation (<1s), it is suggested that the device for the fast separation have 2mm overall thickness, with the separation column placed at the center.

6. Preliminary results of nCE separation and performance extrapolation

6.1. Analysis of nCE separation

Fig. IV. 13 shows color-mapped images of nCE separation results; t=0ms is the time when the separation is started, so negative times are for loading processes.

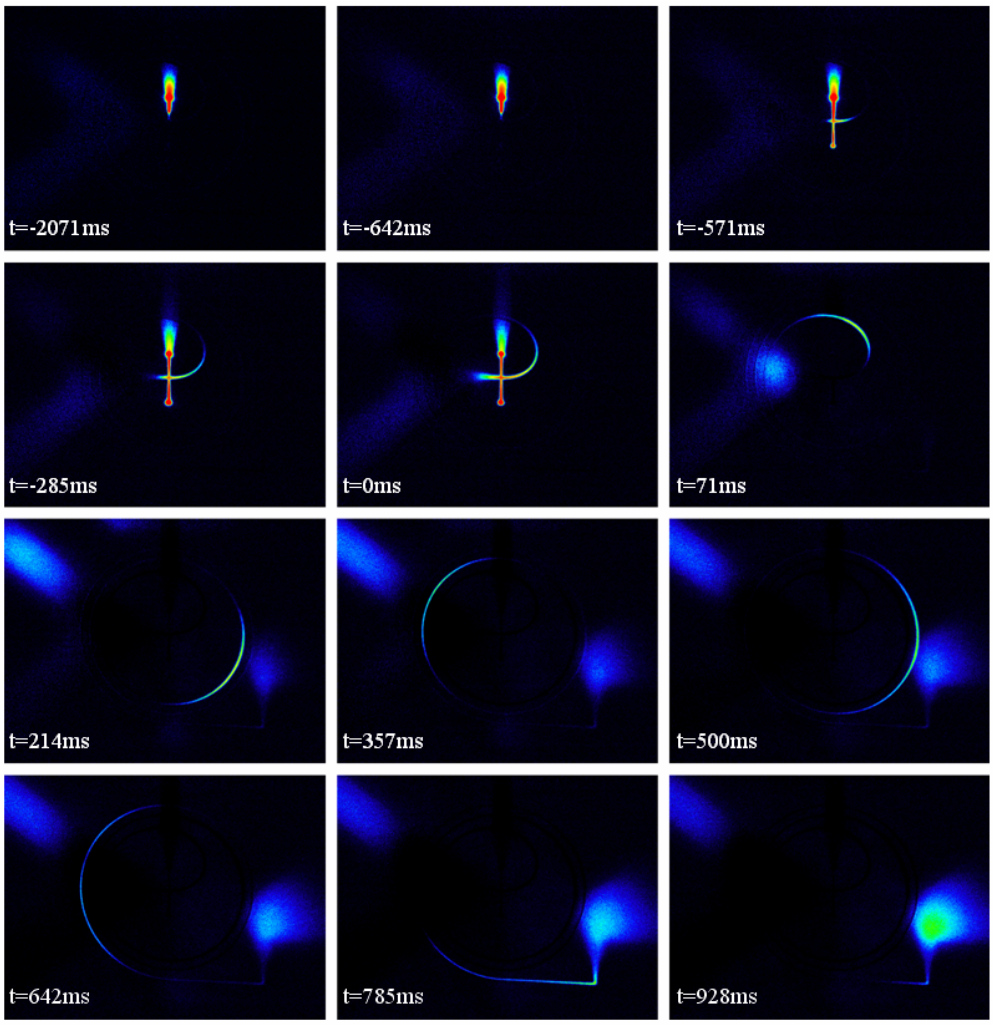

Fig. IV. 13. Color-mapped fluorescent images of nCE separation of Rhodamine110 and Fluorescein.

To generate an electropherogram (Fig. IV. 14) of the nCE separation from the fluorescent data (Fig. IV. 13; grey scale images before the color-mapping), 5 steps of image processing were carried out; 1) background subtraction, 2) cropping of detection area, 3) intensity reading, 4) compensation of uneven illumination, and 5) integration of data taken from each image.

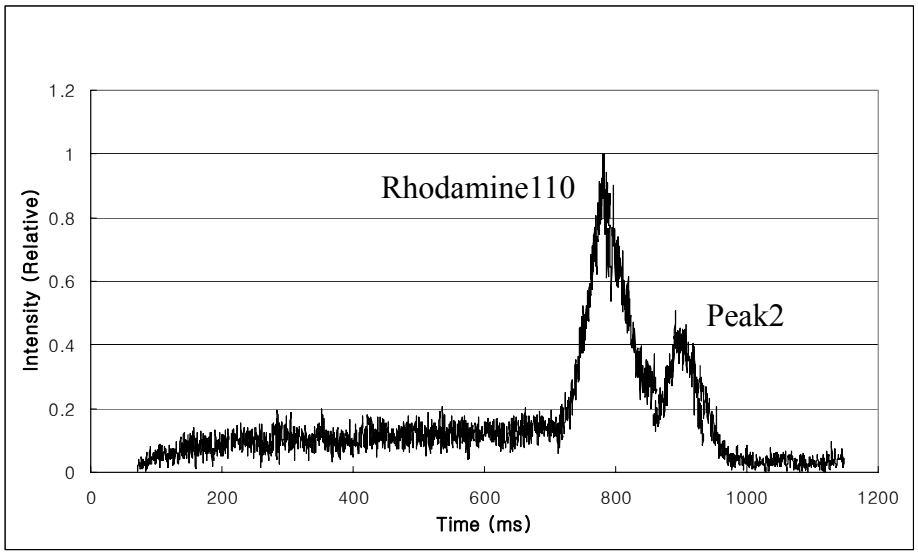

Fig. IV. 14. Electropherogram of nCE separation of Rhodamine110.

Rhodamine110 and Fluorescein are well separable using capillary electrophoresis because the difference of electrophoretic mobility ($\Delta\mu_{ep}$) of these analytes is substantial, even when both analytes are negatively charged in basic solution. In alkaline buffer solution (pH of 9.0), $\Delta\mu_{ep}$ of these two analytes is about $1.7\times10^{-8}m^2/Vs$, and $\Delta\mu_{ep}$ increases up to $3.5\times10^{-8}m^2/Vs$, when the pH of the buffer decreases to 7.0 [47, 48]. In neutral solution (pH~7.0), Rhodamine110 is neutral, whereas Fluorescein is still negatively charged; the dissociated carboxyl group ($–COO^-$) and the protonated amino group ($–NH_3^+$) in Rhodamine110 form a dipole, making net charge neutral, whereas Fluorescein is negatively charged because of the dissociated carboxyl group [45]. As described, the ionization state of Rhodamine110 varies according to pH of the buffer solution, similar to other zwitterionic analytes such as amino acids, proteins, and peptides. Thus, $\Delta\mu_{ep}$ of Rhodamine110 and Fluorescein accordingly varies.

In the separation of Rhodamine110 and Fluorescein in neutral phosphate buffer, the migration of Rhodamine110 directly represents the electroosmosis. The concentration peak of Rhodamine110 in the electropherogram (the first peak in Fig. IV. 14) corresponds to an apparent mobility of 2.25×10^{-8} m^2/Vs, which also represents the electroosmotic mobility of the fs-laser-machined glass nanocapillary.

Electroosmosis in the glass capillary with a buffer solution of ionic strength 10-

100mM and pH of 6-9 is usually much stronger than the electrophoresis of most anionic analytes, including Fluorescein, resulting in the migration of all the ions toward the cathode in the order of cations, neutrals, and anions. However, the calculated electroosmotic mobility in the nCE separation column ($2.25\times10^{-8}m^2/Vs$) is about 1.5 times smaller than the electrophoretic mobility of Fluorescein ($-3.5\times10^{-8}m^2/Vs$; neutral solution) [47]. Therefore as long as the measured electroosmosis is accurate, the migration of Fluorescein should be opposite to Rhodamine110.

This is well shown in Fig. IV. 15. As indicated with white dotted circles, it is evident that Fluorescein in the sample immediately separates and migrates toward the anode, whereas Rhodamine110 migrates with electroosmosis toward the cathode. When considering that the migration velocity of the analyte should be faster than 0.7mm/s to completely escape the separation column (the analyte should travel at least 48μm within 71ms) as shown in Fig. IV. 15 (a) and (b), the magnitude of the electrophoretic mobility should be larger than $3.05\times10^{-8}m^2/Vs$, which is in great agreement with the reference value of Fluorescein ($-3.5\times10^{-8}m^2/Vs$).

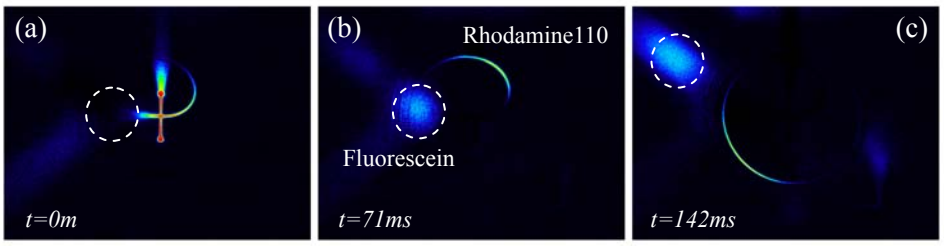

Fig. IV. 15. Migration of Fluorescein toward anode.

The electroosmosis can also be theoretically analyzed by the Helmholtz-Smoluchowski equation, shown in equation (44); ε is the permittivity of the solution, ζ is the zeta potential, η is the viscosity and E is the electric field strength [45].

$$U_{EO} = \frac{\varepsilon\zeta}{\eta}E = \mu_{eo}E \tag{44}$$

Standard parameters such as ε and η of water and ζ of 0.1V for a typical glass surface [45] calculate the electroosmotic mobility of $7.08\times10^{-8}m^2/Vs$, which is about 3 times higher than that of the fs-laser-machined glass surface ($2.25\times10^{-8}m^2/Vs$). Provided that the error of ε and η are trivial, three times smaller zeta potential of the fs-laser-

machined glass surface accounts for the decreased electroosmotic mobility; the zeta potential of the fs-laser-machined separation column can be calculated as 31mV in the buffer solution having pH of 7.0 and 10mM ionic strength.

The decreased zeta potential of the fs-laser-machined glass surface is caused by the reduced surface charge density, presumably due to reduced ionization of the silanol group on the glass surface. In the case of the fs-laser-machined glass surface, the ionization of the silanol groups seems to be more significantly suppressed when the wall is exposed to fs-laser pulses for a longer duration. This conjecture is supported by the experimental results showing that the sample loading channels whose machining time is less than a half hour successfully transport Fluorescein and Rhodamine110 in the same direction, whereas the separation column requiring 4 hour processing shows significant reduction of electroosmosis, resulting in the opposite migration of anions (Fluorescein) and neutrals (Rhodamine110).

So, it would be evident that the analyte migrating toward the cathode is Rhodamine110; however, it is eventually separated into two peaks as resolved in the electropherogram (Fig. IV. 14). Although the difference of their mobility is very small, the substantial difference in the measured diffusion coefficients implies that they are different in their molecular weights, and have varying electrostatic properties. Considering additional dispersion due to the spiral shape of the separation column and the potential concentration gradients in the radial direction, only the first peak in the electropherogram, which measures somewhat higher diffusion coefficient ($7.1\times10^{-10}m^2/s$) than that of the reference Rhodamine110 ($4.37\times10^{-10}m^2/s$) [48], can be the reference Rhodamine110.

Based on the zone broadening of the peaks, the second peak has a 2.4 times smaller diffusion coefficient than that of the first peak (reference Rhodamine110). Although it could be from impurities such as Rhodamine110-based bis-peptides, the aggregated Rhodamine110 molecules forming apparently larger molecules would better explain the second peak. In this case, based on the diffusion coefficient estimation method by William A. Tucker and Leslie H. Nelken [49], the molecular weight of the second peak (~1620) can be estimated to be 4.4 times larger than that of reference Rhodamine110 (366.8); thus, the aggregation of 4-5 Rhodamine110 molecules can

explain the slow zone broadening of the second peak. However, the ionic property of the second peak should be different from the Rhodamine110 so as to show even a slight difference in electrophoretic mobility, because neutrals are not separable with capillary electrophoresis. The slower migration of the second peak can be satisfied when these two peaks are positively charged; however, this is excluded because the buffer solution should be sufficiently acidic to make Rhodaime110 cationic. Therefore, the aggregated Rhodamine110 molecules most likely become negative under these conditions, while the Rhodamine110 remains neutral, causing the difference in electrophoretic mobility to be $0.29\times10^{-8}m^2/Vs$.

	W [μm]	$D^*\times10^{10}$ [m^2/s]	U_{peak} [mm/s]	$\mu_{app}\times10^8$ [m^2/Vs]	$\Delta\mu_{12}\times10^8$ [m^2/Vs]	MW	Ionic Prop.
R110	135	7.1	0.96	2.25	0.29	366.8	Neutral
Peak2 ($[R110]_{4-5}$)	88	2.9	0.84	1.94		1621	Negative

TABLE V. Electrokinetic flow characteristics along the nCE separation column.

The reduced electroosmosis can be advantageous, because 1) the same resolution can be achieved with shorter overall separation lengths, 2) the additional dispersion due to fast electroosmosis is reduced, and 3) fast electroosmosis can be sometimes problematic where a high pH buffer solution is required for the separation of specific analytes, such as proteins. However, a more compelling issue would be the ability to eliminate solute adsorption due to electrostatic binding of cationic substances to the walls of the tubing.

Solute adsorption to capillary walls is a common problem for capillary electrophoresis, especially for separating proteins. Solute adsorption is proportional to the residence time of analytes in the capillary and the surface charge density attracting analytes to the wall. Thus, fast separations that minimize the residence time and surface treatments suppressing surface charge density are extensively applied to reduce adsorption problems. The fs-laser machined nanocapillary not only achieves very fast separations, but the suppressed surface charge density of the fs-laser-machined capillary walls is also expected to reduce electrostatic binding of counterionic solutes.

To best exploit the surface-modifying aspects of the fs-laser pulses, the

mechanism by which the fs-laser pulses suppress the ionization of the silanol group on glass surface should be identified. In addition, based on parametric research, quantitative relationships between exposure to the fs-laser pulses and the change of surface charge density should be determined.

6.2. nCE separation measurements

Based on the measured electrokinetic properties of the electrolyte, analytes, and the nCE separation column, the separation performance of the nCE device under higher electric field strengths than 440V/cm can be extrapolated as shown in **TABLE VI**.

E-field [V/cm]	Potential [V]	t_m [ms]	t_{sp} [ms]	$\bar{U}$ [mm/s]	l_{inj} [μm]	N	n_c	H [μm]	ΔT_{act} [K]
429	38.5	780	290	0.97	25	683	6.5	1.102	0.0011
42,900	*3,735*	*7.8*	*0.029*	*96.6*	*2.5*	*68,451*	*65.4*	*0.011*	*5.55*
53,000	*4,614*	*6.3*	*0.019*	*119*	*2.25*	*84,582*	*72.7*	*0.009*	*8.34*

TABLE VI. Evaluation of the separation performance under higher electric field strengths.

The calculation of the plate number is performed based on actual zone broadening; the electric field strength of 53kV/cm improves the efficiency up to 84,000. Considering that increasing the electric field strength is mostly limited due to the dielectric breakdown of the electrolytes, longer separation columns should be incorporated to increase the separation efficiency. Resolution can also be enhanced by improving selectivity. As the efficiency improves the separation resolution, the selectivity, which increases the difference of the electrophoretic mobility of any specific target molecules, can very effectively improve the separation resolution (see equation (25)).

Thus, diverse modes of CE separations possible with this technology can expand the selectivity to a wide range of biomolecules. For example, MECC would be a very effective CE mode for the separation of proteins, polypeptides, and nucleic acids. In addition, a proper surface coating is highly suggested as a solution to the potential solute

adsorption. Submicron-scale separation columns would suffer from solute adsorption more significantly due to the increased the ratio of surface area to volume.

The electrical potential required to generate 53kV/cm electric fields along the nCE separation column is only about 4.6kV, because the overall length of the nCE separation column is yet very short. Considering that commercially available high voltage power supplies can generate electric potential up to 40kV, even portable systems can operate under this extremely high electric field strength.

7. Discussion

3-dimensional nano-capillaries have many potential applications that are very difficult to realize with micron-scale capillaries. Among the potential applications, fields dealing with individual cells, such as single cell analysis and lab-in-a-cell, are the most significant applications. In these fields, nano-capillaries are expected to assume many functions, such as sensors to measure the electrical property changes of a cell, syringes to extract intracellular materials or inject reagents into a cell, or even separation tools to directly analyze intracellular materials or organelles.

This chapter, which analyzes the nCE separation, is meant to initiate the submicron-scale separation regime and to assess its separation performance, especially for single cell proteomics. Preliminary nCE separation results are very important achievements in that the submicron-scale separation regime is realized using fs-laser-machined 3-dimensional nano-capillaries. Although the reproducibility and stability of nCE separations are not yet sufficiently assessed, and the separation of Fluorescein and Rhodamine110 are not recorded at the same detection window due to their opposite migration directions in the fs-laser-machined capillary having reduced electroosmosis, it is proved that all the main processes in CE separation, such as sample loading to the nanoscale capillary, electrophoretic migration of the analytes for separation, and analyte detection, are successfully performed.

No current separation technique can separate all molecules, i.e. CZE cannot separate neutrals and test samples in CITP should have the same charge polarity. Likewise, the fs-laser-machined capillary with reduced electroosmosis is not well suited to separating samples with highly mobile anions, because they will migrate opposite the electroosmosis, whereas slow anions, neutrals and cations will migrate with the electroosmosis.

The developed nCE separation device is highly suitable to single cell proteomics, and even to single-organelle proteomics, considering that the 3-dimensional nanocapillary is directly carved in glass allowing maximum freedom to configure the device platform. The volume of the test sample is 3 orders of magnitude smaller than the average cell volume and can be directly loaded without additional waste using the zero-flow sample loading method. Additionally, the weak fluorescence of a sparse sample is

proved to be easily detectable.

The nCE submicron-scale separation device still needs to exhibit reproducible and stable operation to assess the separation performance of proteins, peptides, and nucleic acids. In addition, the zero-flow sample loading method also needs to be optimized to ensure exact femtoliter sample loading, and the current-controlled dielectric breakdown mechanism, which is thought to be the mechanism driving the zero-flow sample loading method, needs further analysis to be applied to many important micro/nanofluidic components such as nano-sensors and submicron-scale EK pumps.

The successful adaptation of diverse CE modes with the nCE separation column will improve the resolving power, effectively performing the separation of diverse biomolecules. Successful development of the nCE separation device not only initiate a new submicron-scale separation regime for faster, safer, highly resolvable, and less consuming analyses, but also invites new biological ventures including single cell analysis and lab-in-a-cell technology.

CHAPTER V

FUTURE APPLICATIONS

1. Micro/nanofluidic 3-dimensional module developments

1.1. Nanosensors based on current-controlled dielectric breakdown

Based on the newly found current-controlled dielectric breakdown (CCDB) at the thin glass-wall, nanosensors can be directly developed that sense the electric field interference of charged species. Moreover, because this sensor is machined by fs-laser-nanomachining, the shape and the location of the sensor are not virtually limited. The sensor size can vary from 600nm to several microns.

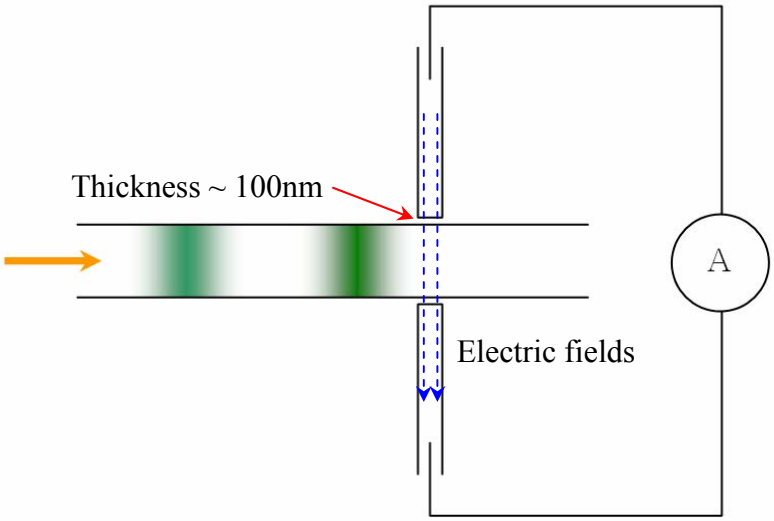

Fig.V. 1. Schematic of a nanosensor for CE detection

As shown in Fig.V. 1, two nanocapillaries are machined at the detection area of the separation column; the sensor capillaries do not penetrate the separation column, but approach it as close as possible (~100nm). The electric field crossing the separation column can be affected by the analytes, resulting in changes in current.

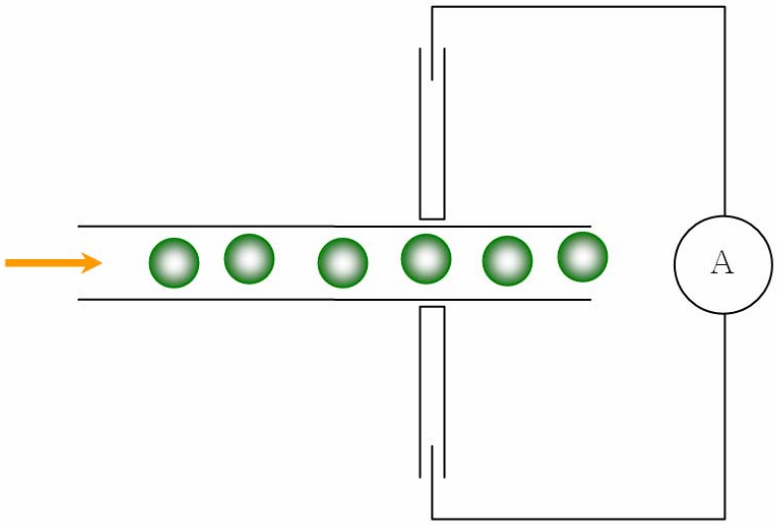

Fig.V. 2. Electrical cell configuration using glass nanosensors.

This sensing mechanism can be directly used in continuous flow electrical cell configurations, as shown in Fig.V. 2. Also, this technique can be applied to bioelectric recognition assays (BERA) [50] combined with molecular identification through membrane engineering (MIME).

1.2. EK actuator based on electrokinetic pressure generation

It is very advantageous if pressure can be easily generated in a microfluidic chip. EK pumps are usually very small, but it is not yet feasible to integrate EK pumps in microchips. If a pair of electrodes can be installed in the middle of a capillary, then pressure can be generated for PDF, as shown in Fig.V. 3. Currently, micron-scale porous media is used in an EK pump to generate strong EOF. Smaller pores can build up higher pressure because back flow along the center of the pore is diminished. However, more pores are then needed to support the flow rate; thus, porous media is suitable to high flow rate EK pumping.

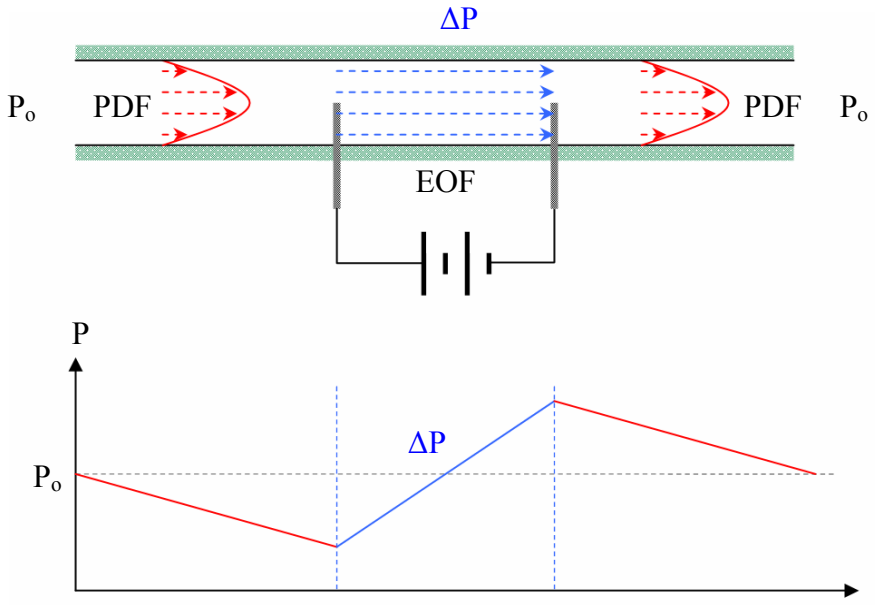

Fig.V. 3. Mechanism of electrokinetic pressure generation.

This concept can be directly applied to generate electrokinetic pressure employing the novel CCDB electrodes, as shown in Fig.V. 4. More than one channel can be embedded for enhanced fluid flow and control.

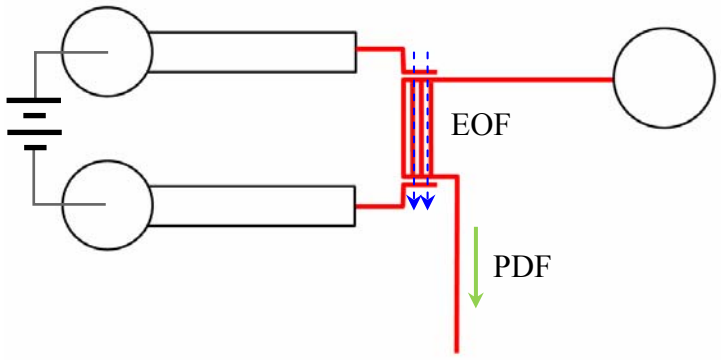

Fig.V. 4. Schematic of EK pump employing CCDB electrodes.

This EK pressure actuator has many applications, e.g. intracellular extraction, pressure driven sample loading, post-driving mechanism of a CIEF microchip, and driving mechanisms of bubble compartments.

1.3. Surface tension valve for bubble compartments

Valves are considered one of the most important microfluidic modules, in that they regulate flows to achieve more complicated flow manipulations in a highly predictable and controllable manner. Installing valve systems in microchips, however, is a somewhat complicated process. Valve installation is difficult in all-glass microchips, whereas soft polymer materials such as PDMS enable much easier valve system incorporation. However, multiple-layer configurations are still required to achieve valving in polymeric substrates.

A valving system driven by surface tension can be used in glass microchips for the bubble compartment, because no moving parts are needed. As shown in the Fig.V. 5 (a) and (b), the pressure gap made by surface tension at the liquid-air interface can be used as a valve in (a) locations where the capillary surface changes from hydrophilic to hydrophobic, or (b) locations where the capillary geometry undergoes a sudden expansion. To drive flows toward the air, the internal pressure of the liquid should be higher than the pressure gap (ΔP).

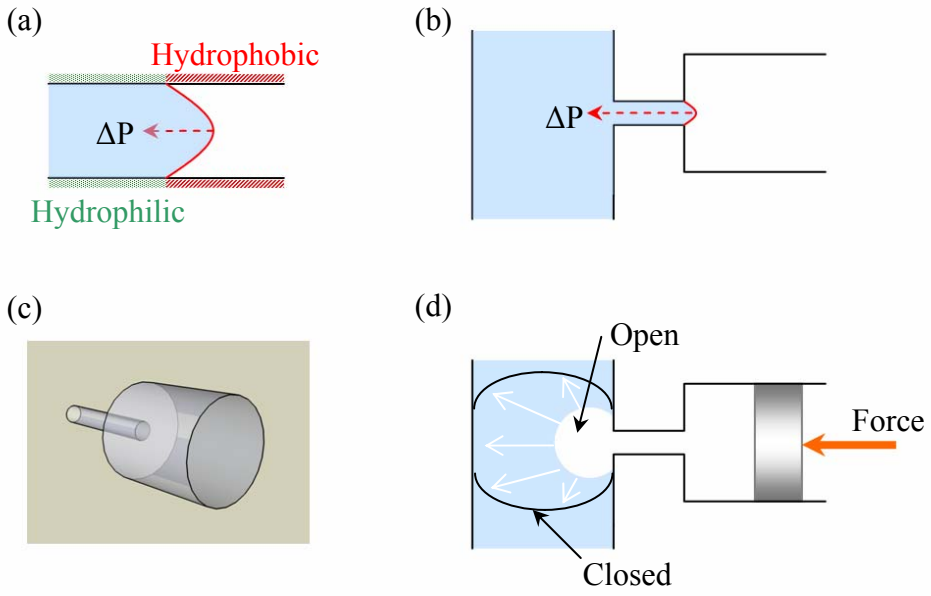

Fig.V. 5. Schematic of surface tension valve and bubble compartments.

As shown in Fig.V. 5 (c), fs-laser-machining can easily fabricate the valve geometry. Larger parts can be configured through lithography-etch processes before the fs-laser-machining, then, just one simple and quick scanning of laser pulses can finalize complete valve configurations. Moreover, the submicron-scale capillaries achieve higher pressure gaps of at least 160kPa, because the pressure gap is inversely proportional to the capillary radius. When higher flow rates are required, simply adding more capillaries can achieve higher flow rates yet equivalent pressure gaps.

Figure (d) shows the valving mechanism. The surface tension valve uses the pressure gap to prevent the liquid from flowing toward the air channel as long as the local pressure of the liquid channel does not exceed the pressure gap. Pressurizing the air starts to form a bubble in the liquid channel, forming a bubble compartment. After a bubble is formed, the flow can be controlled by changing the bubble volume size. The bubble generally has higher internal pressure, which promotes gas diffusion into the liquid; thus, feed-back control of the air pressure will be necessary to regulate the bubble size.

Combining this system with an EK pump can significantly simplify the device configuration by eliminating the need for external pressure supplies and pressure valve controls. However, because gas diffusion will decrease the total gas volume in the air channel, the valve will have a finite runtime. So, the runtime of the bubble compartment valve will need to be extended longer than the lifetime of the cell. This problem can also be permanently solved by adding an additional access channel for air refill.

1.4. 3-dimensional fast diffusion mixer

Mixing of micron-scale fluid flows suffers from lack of turbulence; thus, mixing in microfluidic devices typically depends on diffusion. Improving mixing performance is closely related to reducing diffusion length, i.e. the herringbone mixer [51] and the topologic mixer [52]. Reducing the diffusion length N times reduces the mixing time by N^2 times.

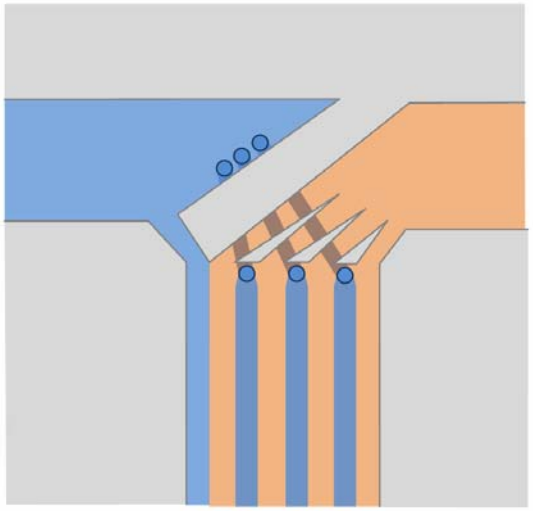

Fig.V. 6. Schematic of 3-dimensional fast diffusion mixer

3-dimensional capillaries can reduce the diffusion length very easily, as shown in Fig.V. 6; the number of capillaries directly affects the diffusion length. Thus, the number of 3-dimensional capillaries can be easily controlled to achieve appropriate mixing times.

The fast diffusion mixer is relatively simple and small. Also, the 3-dimensional capillaries of low NCL are relatively quick and easy to fabricate by fs-laser-machining.

2. Single cell analysis using submicron-scale 3-dimensional capillary

2.1. Cell manipulation and immobilization

Cell manipulation techniques are central to cell biology, and many approaches have been developed so far. Among them, optical tweezers and dielectrophoresis (DEP) are well-developed and versatile in handling individual cells.

When individual cells are manipulated in a microchip, the cell manipulations are often very specific; the microchip channel size can limit the analyzable target cells. Such is also the case for the cell manipulation and immobilization technique suggested here, because the hypotonic cell immobilization technique exploits changes in the cell membrane volume.

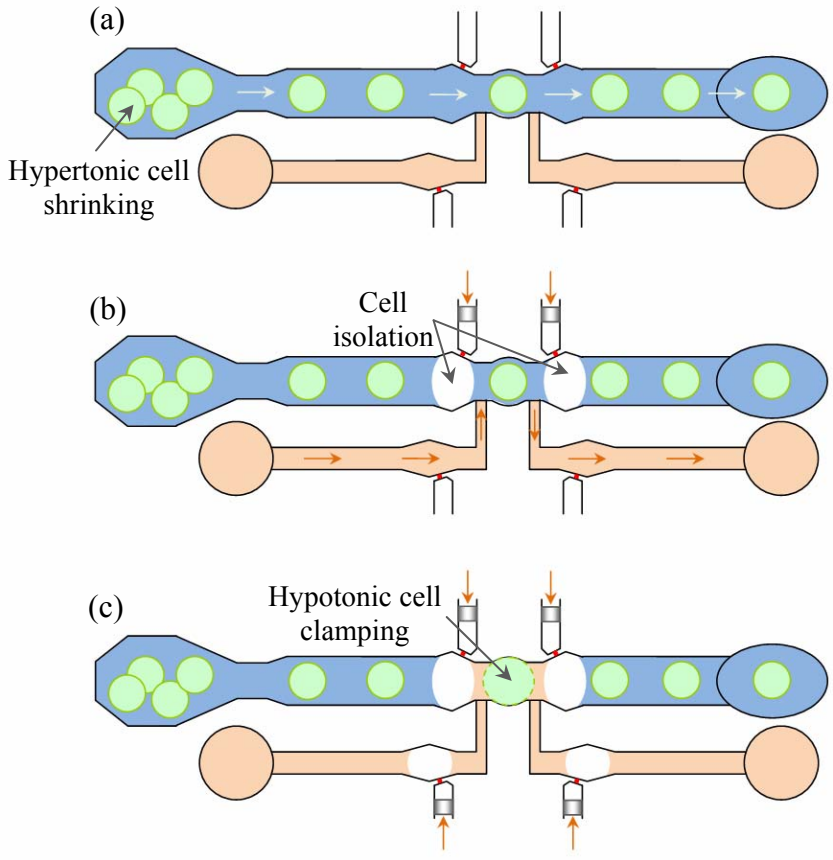

Fig.V. 7. Single cell isolation and hypotonic immobilization

As shown in Fig.V. 7, cells are prepared in a slightly hypertonic solution (indicated with blue color), slightly shrinking the cells. During cell analysis, isotonic or

slightly hypotonic solution (indicated with orange) will reverse the cell size such that it fits in the test compartment. The single cell isolation and immobilization processes can be explained in three steps: (a) the flow of cells can be continued until a specific target cell is loaded in the test compartment at the center, then (b) the surface tension valve injects bubbles for cell isolation, and the isotonic or slightly hypotonic solution replaces the test compartment to swell the cell, and finally (c) the other valves inject bubbles to completely isolate the cell test compartment.

Step (c) might not be necessary to continuously supply nutrition to the cell, which may be critical for cell viability. So, the complete isolation may require only electrical cell characterization and communication experiment.

2.2. Cell characterization

Once a cell is immobilized in the test compartment, cell characterization can be performed. Because the contact area with cell membrane can be several times broader than the cross-sectional area of the submicron-scale capillary, a sensor array can be installed at the contact area, enabling multiple sensing of local spots on the cell membrane. The nanosensors installed in the non-contact area of the test compartment are for measuring the entire electrical resistance and potential of the cell.

CCDB nanosensors and open-ended capillaries will be compatible as cell membrane sensors and electrical stimulators; the open-ended capillaries will be more sensitive than CCDB sensors, but the accuracy or reliability might be worse because the solution in the test compartment will diffuse in the open-ended capillary, changing the electrical characteristics of the electrolytes.

In addition, the open-ended capillaries will perform electroporation to transfer reagents into the cell and to extract cell materials such as cytoplasm, organelles, and nucleic acids through the submicron-scale hole on the cell membrane.

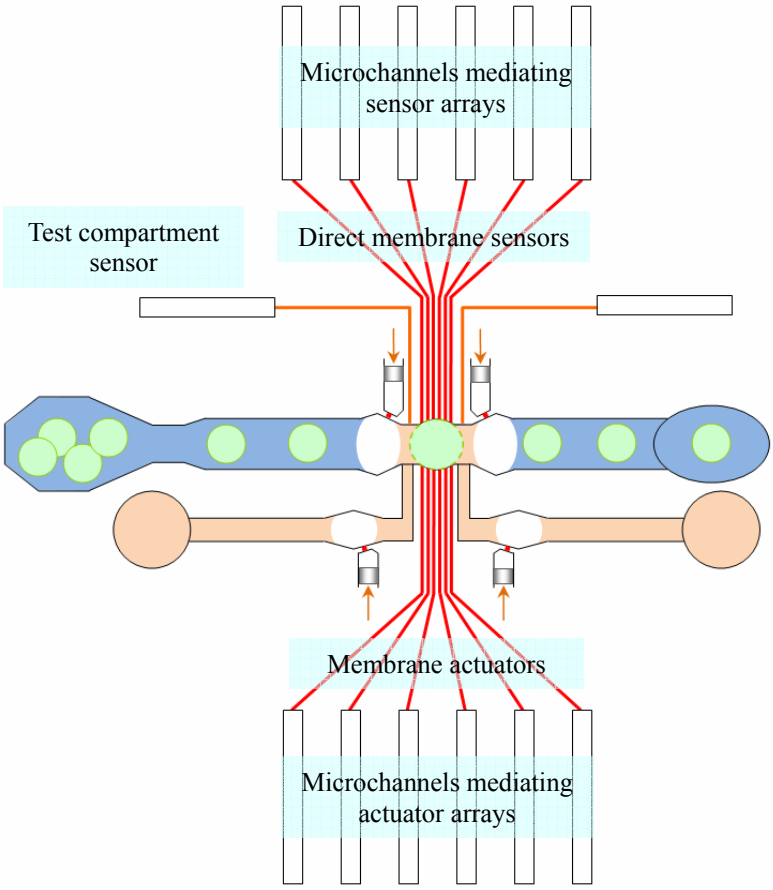

Fig.V. 8. Electrical single cell characterization.

As shown in Fig.V. 8, arrays of direct membrane sensors and membrane actuators or stimulators can be installed on the test compartment walls. The test compartment sensors are for measuring changes of the electrical resistance and potential of the cell.

2.3. Single cell proteomics

Single cell proteomics can be performed in two different modes. The first mode is a single cell lysate via an entire lysis of the cell in the test compartment, and the second mode is direct extraction of the cell material using electroporation. Electrokinetic loading might be available in the first mode, however, pressure driven loading will be better in both modes. Intracellular materials are in general sensitive to electric fields, and pressure driven flow can be equally effective in loading uncharged molecules.

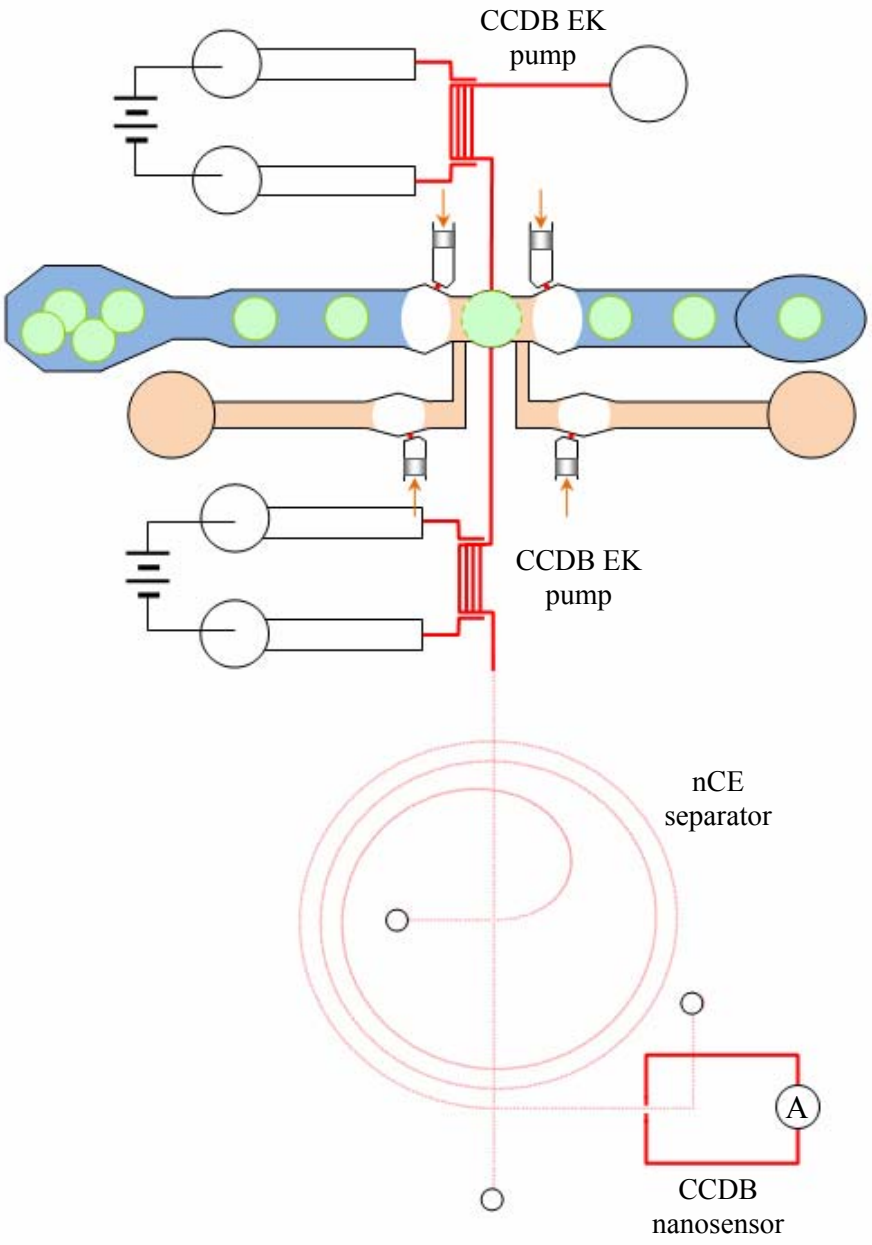

Fig.V. 9. Schematic of single cell proteomics using the nCE separation method.

As shown in Fig.V. 9, two EK pumps based on CCDB can work together to extract intracellular materials and transfer reagents into the cell. To completely lyse the cell, special reagents dissembling the cell membrane can be used instead of the hypotonic solution.

3. Biomedical assays: micro-ELISA device

3.1. Introduction

Enzyme-linked immunosorbent assay (ELISA) is a biochemical technique used primarily in immunology to detect the presence of an antibody (indirect ELISA) or an antigen (sandwich ELISA) in a sample. ELISA has been used as a diagnostic tool in medicine and plant pathology, as well as a quality control check in various industries. Because ELISA can be performed to evaluate either the presence of antigen or the presence of antibody in a sample, it is a useful tool both for determining serum antibody concentrations (such as with HIV or West Nile Virus tests) and also for detecting the presence of antigen.

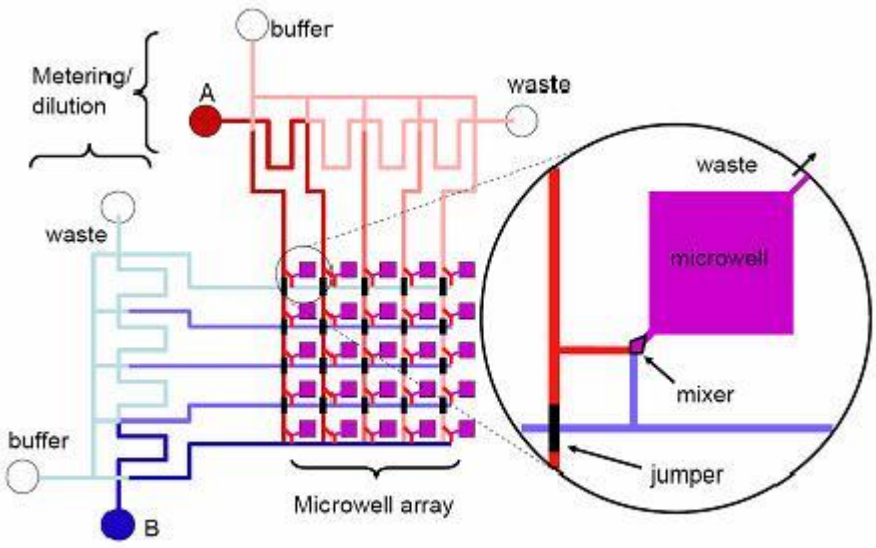

Fig.V. 10. Typical serial dilution-mixing arrays for micro-ELISA

To realize biological assays such as ELISA in a microchip format, complex mixing arrays (combinations of serial mixing arrays [53]) are very important, as shown in Fig.V. 10. Because ELISA requires many dilution/mixing steps of antigen and antibody, substituting conventional ELISA processes with microfluidic devices using continuous serial dilution-mixing-detection processes can have great advantages in terms of speed, simplicity, cost and accuracy. Continuous monitoring of antibody-antigen conjugates can be achieved using rapid diffusion in a T-sensor [54].

The fs-laser-machining method can best achieve the complex configuration of these mixing array networks through 3-dimensional connections made with U-jumper channels. The jumper configuration can be combined with a single layer glass plate to reconfigure 3-dimensional complex geometries. In addition, because fs-laser-machining can be performed during assay operation, post processing for precisely tuning the hydrodynamics of the assay is possible.

3.2. Constructing complex networks with fundamental components

Microfluidic networks are analogous to electric circuits. Whether it is complex or simple, any microfluidic network can be represented with a matrix form. Fig.V. 11 shows the way to express a Y channel with an equivalent circuit, which can be directly solved.

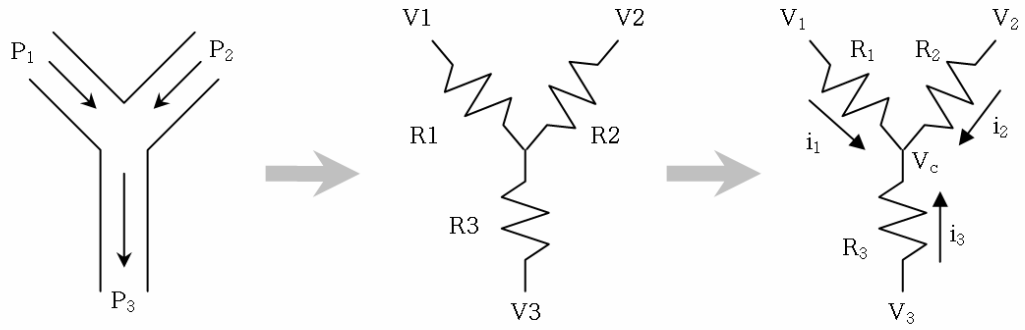

Fig.V. 11. Equivalent circuit diagram of Y junction on the basis of the analogy between hydrodynamic or electrokinetic channel flow and electric current.

The Y channel, which has 3 branches and 1 node, can be directly solved to get a general solution for flow rate, as shown in equations (45) and (46).

$$\begin{pmatrix} V_1 - V_3 \\ V_2 - V_3 \end{pmatrix} = \begin{pmatrix} R_1 + R_3 & R_3 \\ R_3 & R_2 + R_3 \end{pmatrix} \begin{pmatrix} i_1 \\ i_2 \end{pmatrix} \tag{45}$$

$$\begin{pmatrix} i_1 \\ i_2 \end{pmatrix} = \frac{1}{R_1R_2 + R_2R_3 + R_3R_1} \begin{pmatrix} R_2 + R_3 & -R_3 \\ -R_3 & R_1 + R_3 \end{pmatrix} \begin{pmatrix} V_1 - V_3 \\ V_2 - V_3 \end{pmatrix} \tag{46}$$

If a junction had N input branches and 1 output branch with 1 node, then the solution would be expressed as equations (47) and (48).

$$\begin{pmatrix} V_1 - V_{N+1} \\ V_2 - V_{N+1} \\ \vdots \\ V_N - V_{N+1} \end{pmatrix} = \begin{pmatrix} R_1 + R_{N+1} & R_{N+1} & \cdots & R_{N+1} \\ R_{N+1} & R_2 + R_{N+1} & \cdots & R_{N+1} \\ \vdots & \vdots & \ddots & \vdots \\ R_{N+1} & R_{N+1} & \cdots & R_N + R_{N+1} \end{pmatrix} \begin{pmatrix} i_1 \\ i_2 \\ \vdots \\ i_N \end{pmatrix} \tag{47}$$

$$\begin{pmatrix} i_1 \\ i_2 \\ \vdots \\ i_N \end{pmatrix} = \begin{pmatrix} R_1 + R_{N+1} & R_{N+1} & \cdots & R_{N+1} \\ R_{N+1} & R_2 + R_{N+1} & \cdots & R_{N+1} \\ \vdots & \vdots & \ddots & \vdots \\ R_{N+1} & R_{N+1} & \cdots & R_N + R_{N+1} \end{pmatrix}^{-1} \begin{pmatrix} V_1 - V_{N+1} \\ V_2 - V_{N+1} \\ \vdots \\ V_N - V_{N+1} \end{pmatrix} \tag{48}$$

For a general microfluidic network composed of n branches and m nodes, the resistance matrix becomes much more complicated. Composing and solving these matrices, however, become more and more difficult as the network becomes increasingly complicated. Moreover, every time the network needs to be modified, the whole process should be repeated.

Those difficulties can be solved by decomposing the network into a few fundamental components such as Y, T, L and I channels. Most complex microfluidic networks functioning as mixing/dilution processes can be constructed with these fundamental components. After the entire network is constructed with those components, it is solved using an iteration method.

3.3. Substrate layer/mask design for micro-ELISA

The hydrodynamic resistance of each branch is very important because it determines the mixing ratio and flow rates. The wet etching process has a problem in that the hydrodynamic resistance of a wet etched channel is not easy to predict, because the depth and cross-sectional area are not easy to precisely predict. Therefore, the mask for wet etching the substrate should be designed with great care.

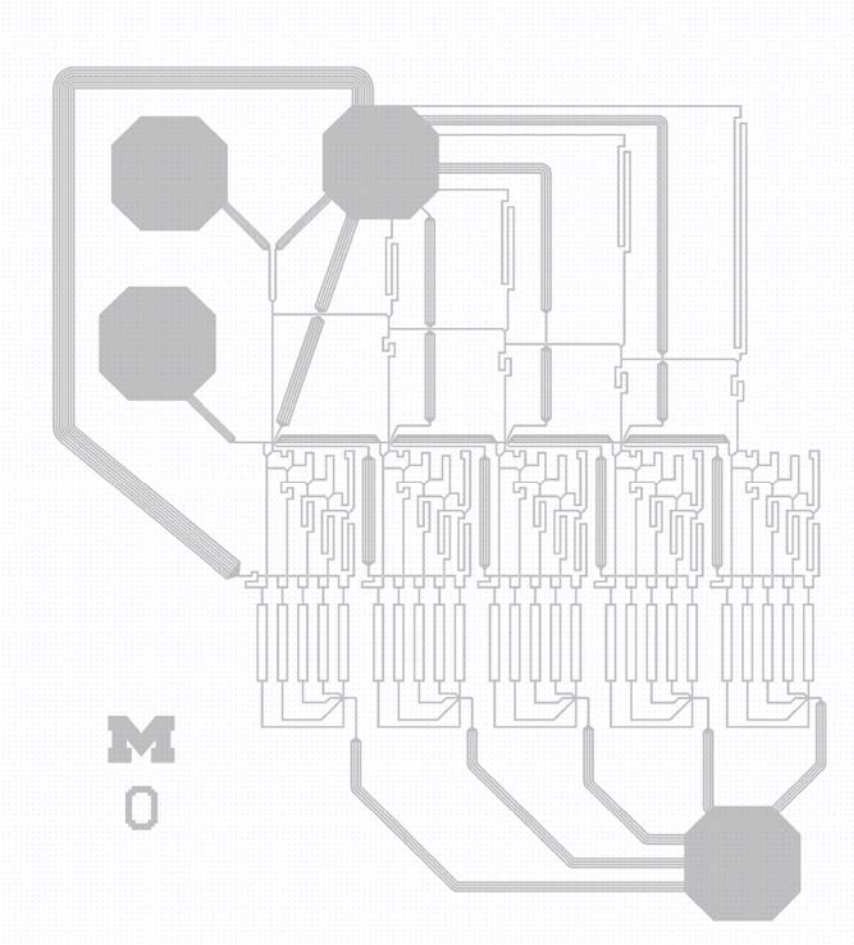

Fig.V. 12. Sample mask design for micro-ELISA substrate

An important design point is that the ratios of the hydrodynamic resistances of all the branches should be guaranteed. To accurately predict the ratios of the hydrodynamic resistances of all the branches, the channel width of all the branches should be the same, allowing only the channel length to be changed. So, when a wider channel is required for low hydrodynamic resistance, a parallel configuration can be used.

After the substrate is ready, fs-laser-machining connects the branches with jumpers. Following microchip assembly, post processing will be required to finely adjust the flow rates.

CHAPTER VI

CONCLUSIONS

Since femtosecond laser pulses were first used in the field of femtochemistry, impacting the world with the enormous potential for ultrafast science, application fields of ultrafast science have been expanded to many cutting edge fields. Micro/nanofluidics will require 3-dimensional configurations more and more for complex and high density device integration, similar to the evolution of integrated circuits. In addition, effective yet versatile methods for the fabrication of nanogeometries must be established to support special fields, such as biomedical and biological sciences.

Femtosecond laser machining is a method that achieves both 3-dimensional configurations and nanoscale fabrication. Although a few drawbacks should be overcome to successfully establish femtosecond laser machining as a micro/nanofluidic fabrication tool, femtosecond laser machining can realize many novel micro/nanofluidic devices which cannot be achieved using lithography-etch-bond processes. Also, it is very advantageous that femtosecond laser machining and planar lithography-etch-bond process are easily combined, enabling planar single-layered substrates to be reconfigured as complex 3-dimensional devices.

The major accomplishments in this dissertation are 1) improving the maximum normalized length of nanocapillaries to longer than 1000, 2) discovering the acoustic node theory, 3) explaining the complex effects of the laser parameters on machining performance based on the dehydration theory, 4) discovering the current-controlled dielectric breakdown at the thin glass wall, and 5) initiating the submicron-scale separation regime by successfully developing the nCE device. The improved normalized lengths of subsurface capillaries made it possible to perform analytical separations with submicron-scale capillaries. This technique is expected to be applied to single cell proteomics; 1 femtoliter injection volume is about 1000 times smaller than that of a

single cell. Glass electrodes based on current-controlled dielectric breakdown can be exploited in many application fields. Among them, nanosensors are highly expected to contribute to cell characterization and electrophysiology. The new concept of EK pumps based on current-controlled dielectric breakdown will be very important to extract intracellular materials and to transfer reagents into the cell, so-called the nano-syringe.

For now, femtosecond laser machining is relatively expensive and is not suitable to mass production. The extremely small submicron-scale devices are not easy to manipulate and detect. All these drawbacks can be exploited as advantages in some specific application fields dealing with individual cells. Discovering new application fields requiring 3-dimensional complex nanogeometries is also a very important task. The current-controlled dielectric breakdown might be applicable to pre-concentrators [55] and nanoscale electro-optical sensors, which are very important and fundamental micro/nanofluidic modules in complex lab-on-a-chip and micro-total analysis devices [35].

Femtosecond laser machining and its application to the development of new micro/nanofluidic devices and modules will be very powerful tools to pioneer many novel investigations in cell biology, drug-discovery, diagnostics, point-of-care products, separations, and biological assays.

APPENDICES

1. Experimental configuration of femtosecond laser machining

A schematic of femtosecond laser machining is shown in Fig. A. 1. 600-800fs pulses from a diode-pumped Nd:glass CPA (chirped pulse amplification) laser system (Intralase Corp., Irvine, CA) are frequency doubled by KTP crystal (potassium titanyl phosphate; type I crystal, Cleveland Crystals, HighlandHeights, OH) to generate 527 nm pulses with 10-20 nJ pulse energies. They are then brought into the epifluorescence path of an inverted microscope (Axiovert 200, Carl Zeiss Inc., Thornwood, NY) and focused through an objective lens (Zeiss "Plan-Neofluar": 100×, N.A. 1.3, working distance=200μm, oil emersion) to the glass substrate (microscope cover slip: Corning 0211, 25×25×0.17 mm^3) with PRR's of 1.5-2kHz. The thickness of the glass substrate is limited by the working distance of the objective lens; typical glass cover slips (170μm thickness) are well-suitable in most cases. The observation of the machining process is performed either using the naked eye or by a CCD camera (ORCA-ER: HAMAMATSU Photonics K.K., 16fps at 2×2 binning). The substrate is placed on a three-axis (100×100×100μm^3, ±1nm) linear nano-stage (Mad City Labs, Inc., Madison, WI) for true 3-dimensional nanomachining.

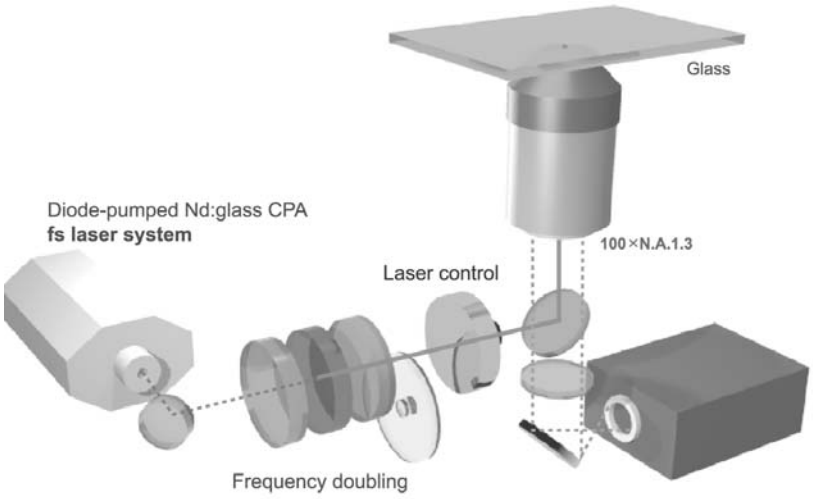

Fig. A. 1. Schematic of femtosecond laser machining setup.

2. Preparation of water for machining

Water is placed on top of the substrate where the machining starts. Without the presence of a header layer, a droplet of water is enough for 1-2 hours of processing. As the machining progresses from the surface to the inside, water is supplied to the ablation site based on the capillary effect and extruded out of the subsurface geometry entraining debris by bubble expansion and/or laser back-scanning.

Ordinary tap water is adequate for machining. However, a new approach based on degassed water has been developed for high NCL subsurface capillary fabrication [31]. To apply the degassed-water-assisted fs-laser-nanomachining, water is degassed by a vacuum pump (Fisher Scientific, Maxima C plus Model M2C, Pittsburgh, PA) for 30 minutes, while being agitated in the ultrasonic bath (Cole-Parmer ultrasonic cleaner, Cole-parmer instrument co., vernon hills, IL) where the temperature is kept at 50°C.

3. nCE substrate preparation

The nCE separation column and the loading channel are fabricated after the PDMS header layer is bonded to the glass substrate, eliminating any alignment difficulties during assembly. To apply the degassed-water-assisted fs-laser-nanomachining, water is degassed and fills the nCE substrate (the PDMS header and the glass plate assembly). Water is degassed by a vacuum pump (Fisher Scientific, Maxima C plus Model M2C, Pittsburgh, PA) for 30 minutes, while agitated in an ultrasonic bath (Cole-Parmer ultrasonic cleaner, Cole-Parmer Instrument Co., Vernon Hills, IL) at 50°C. After degassed water fills the nCE substrate, the upper surface of PDMS layer is temporarily sealed with another microscope cover slip to prevent the water from drying out.

Before the nCE substrate assembly, the PDMS header and glass plate are treated for 30 seconds in a plasma oxidizer (Plasma Prep II: SPI, West Chester, PA) to change the surface characteristics of PDMS to hydrophilic and to strengthen the bonding between the two substrates. Note that over-treating the substrates can cause poor bonding due to SiO_2 formation on the surface of the PDMS. Immediately after nCE substrate assembly, the device is filled with water to maintain hydrophilicity.

4. Test sample preparation

Capillary electrophoresis is an electrokinetically driven separation process, where the average migration speed depends on electroosmosis, and the separation depends on the differences between the electrophoretic mobility. The buffer solution serving as the electrolytes is 10mM phosphate buffer with pH 7.0, where the electric double layer is expected to be 3nm thick [45]. Compared with the 700nm bore size of the nanocapillary, electroneutrality is thought to be satisfied. The test solutes are Rhodamine110 ($C_{20}H_{15}ClN_2O_3$: Molecular Probes, Cat # R6479, CAS # 13558-31-1) and Fluorescein ($C_{20}H_{12}O_5$: Sigma-Aldrich, CAS # 2321-07-5); each solute was initially dissolved in ethanol, and then diluted with phosphate buffer (pH=7.0) for a 40μM final concentration. These solutes are mixed 1:1 for final test sample solutions.

5. Pseudo-color mapping of grey images

For better visualization, the grey scale images are converted to pseudo-color images using black-blue-green-yellow-red conversion scales with custom software; here, red represents the highest fluorescent intensity and black the lowest intensity.

6. General equations in heat transfer analysis

Conduction heat transfer

$$Q = -Ak_{th}\frac{dT}{dx} \tag{A1}$$

$$R_{th\_cond} = \frac{L}{Ak_{th}} \tag{A2}$$

$$R_{th\_cond} = \frac{1}{4\pi k_{th}}\left(\frac{1}{r_i} - \frac{1}{r_o}\right) \tag{A3}$$

$$R_{th\_cond} = \frac{\ln(r_o / r_i)}{2\pi L k_{th}} \tag{A4}$$

Convection heat transfer

$$Q = Ah(T_{surface} - T_{\infty}) \tag{A5}$$

$$R_{th\_conv} = \frac{1}{Ah} \tag{A6}$$

REFERENCES

1. M. G. Pollack, R. B. Fair and A. D. Shenderov, “Electrowetting-based actuation of liquid droplets for microfluidic applications,” Appl. Phys. Lett., 77, 1725-1726, 2000.
2. M. Washizu, “Electrostatic actuation of liquid droplets for microreactor applications,” IEEE Trans. Ind. Appl., 34, 732-737, 1998.
3. T. B. Jones et al., “Dielectrophoretic liquid actuation and nanodroplet formation,” J. Appl. Phys., 89, 1441-1448, 2001.
4. J. Vykoukal et al., “A programmable dielectric fluid processor for droplet-based chemistry,” Micro Total Analysis Systems 2001, 72-74, 2001.
5. T. B. Jones, K. L. Wang, and D. J. Yao, “Frequencydependent electromechanics of aqueous liquids: electrowetting and dielectrophoresis,” Langmuir, 20, 2813-2818, 2004.
6. K. Chakrabarty and J. Zeng, “Design automation for microfluidics-based biochips,” ACM Journal on Emerging Technologies in Computing Systems, 1, 186-223, 2005.
7. BCC Research, “Microfluidics technology,” WA1391278, Marketresearch.com, 2006.
8. Frost & Sullivan, “Advances in lab on chip/microfluidics for drug discovery and clinical diagnostics,” MC1474829, Marketresearch.com, 2007.
9. Yole Developpement, “Emerging markets for microfluidic applications,” YOLD1505556, Marketresearch.com, 2007.
10. W. E. Lamb Jr., “Theory of an optical laser,” Phys. Rev. 134, A1429, 1964.
11. M. H. Crowell, “Characteristics of mode-coupled lasers,” IEEE J. Quantum Electron. 1, 12, 1965.
12. H. A. Haus, “Mode locking of lasers,” IEEE J. Sel. Optics Quantum Electron. 6, 1173, 2000.
13. L. E. Hargrove, R. L. Fork, and M. A. Pollack, “Locking of He-Ne laser modes induced by synchronous intracavity modulation,” Appl. Phys. Lett., 5, 4, 1964.
14. A. J. DeMaria, D. A. Stetser, and H. Heynau, “Self mode-locking of lasers with saturable absorbers,” Appl. Phys. Lett., 8, 174, 1966.
15. E. P. Ippen, C. V. Shank, and A. Dienes, “Passive mode locking of the cw dye laser,” Appl. Phys. Lett., 21, 348, 1972.
16. R. Trebino, “Frequency-resolved optical gating: the measurement of ultrashort laser pulses,” Springer, ISBN 1-4020-7066-7, 2002.
17. Iaconis and I. A. Walmsley, “Spectral phase interferometry for direct electric-field reconstruction of ultrashort optical pulses,” Opt. Lett. 23(10), 792-794, 1998.
18. V. V. Lozovoy, I. Pastirk, and M. Dantus, “Multiphoton intrapulse interference 4: Characterization and compensation of the spectral phase of ultrashort laser pulses,” Opt. Lett. 29, 775-777, 2004.
19. N. Bloembergen, “Laser-induced electric breakdown in solids,” IEEE J. Quantum Electron. QE-10, 375, 1974.
20. D. Du, X. Liu, G. Korn, J. Squier, G.Mourou, “Laser-induced breakdown by impact ionization in SiO_2 with pulse widths from 7ns to 150fs,” Appl. Phys. Lett., 64, 3071, 1994.
21. A. P. Joglekar, H. Liu, E. Meyhöfer, G. Mourou, and A. J. Hunt, “Optics at critical intensity: applications to nanomorphing,” Proc. Nat. Acad. Sci. USA 101, 5856-5861, 2004.
22. A. J. Joglekar, H. Liu, E. Meyhöfer, G. Mourou, and A. J. Hunt, “A study of the

deterministic character of optical damage by femtosecond laser pulses and applications to nanomachining," Appl. Phys. B-Lasers and Optics 77, 25-30, 2003.
23. A. Vogel, J. Noack, G. Hüttman, and G. Paltauf, "Mechanisms of femtosecond laser nanosurgery of cells and tissues**,"** Appl. Phys. B-Lasers and Optics 81, 1015-1047, 2005.
24. J. P. Mcdonald, V. R. Mistry, K. E. Ray, and S. M. Yalisove, "Femtosecond pulsed laser direct write production of nano- and microfluidic channels," Appl. Phys. Lett. 88, 183113, 2006.
25. C. B. Schaffer, A. Brodeur, J. F. García, and E. Mazur, "Micromachining bulk glass by use of femtosecond laser pulses with nanojoule energy," Opt. Lett. 26, 93-95, 2001.
26. Y. Li et al., "Three-dimensional hole drilling of silica glass from the rear surface with femtosecond laser pulses," Opt. Lett. 26, 1912-1914, 2001.
27. R. An, Y. Li, Y. Dou, D. Liu, H. Yang, and Q. Gong, "Water-assisted drilling of microfluidic chambers inside silica glass with femtosecond laser pulses," Appl. Phys. A: Solids Surf. 83, 27-29, 2006.
28. T. N. Kim, K. Campbell, A. Groisman, D. Kleinfeld, and C. B. Schaffer, "Femtosecond laser-drilled capillary integrated into a microfluidic device," Appl. Phys. Lett. 86, 201106, 2005.
29. K. Ke, E. F. Hasselbrink, and A. J. Hunt, "Rapidly prototyped three-dimensional nanofluidic channel networks in glass substrates," Anal. Chem. 77, 5083-5088, 2005.
30. S. Lee, A. J. Hunt, and E. F. Hasselbrink, "Rapidly-prototyped 3D nanofluidics in glass," Proc. of MicroTAS 2005 Conf., Boston, 2005.
31. S. Lee, J. L. Bull, and A. J. Hunt, "Acoustic limitations on the efficiency of machining by femtosecond laser-induced optical breakdown**,"** Appl. Phys. Lett., 91, 023111, 2007.
32. S.Y. Chou, P. R. Krauss, and P. J. Renstrom, "Imprint Lithography with 25-Nanometer Resolution," Science 272, 85, 1996.
33. M. A. Unger, H. P. Chou, T. Thorsen, A. Scherer, S. R. Quake, "Monolithic microfabricated valves and pumps by multilayer soft lithography," Science, 288, 113-6, 2000.
34. T. Thorsen, S. J. Maerkl, and S. R. Quake, "Microfluidic large-scale integration," Science 298, 580-584, 2002.
35. P. S. Dittrich, K. Tachikawa, and A. Manz, "Micro total analysis systems. Latest advancements and trends," Anal. Chem. 78, 3887-3907, 2006.
36. D. J. Hwang, T. Y. Choi and C. P. Grigoropoulos, "Liquid-assisted femtosecond laser drilling of straight and three-dimensional microchannels in glass," Appl. Phys. A 79, 605-612, 2004.
37. P. Sudbery, "Human molecular genetics," 2nd edition, Prentice Hall, ISBN 0-130-42811-6, 2002.
38. W. S. Klug and M. R. Cummings, "Essentials of genetics," 4th ed. Prentice Hall, ISBN 0-13-091264-6, 2001.
39. Beckman Coulter Genomic Analysis systems, Beckman Coulter, Inc., Fullerton, CA 92834 USA, URL http://www.beckmancoulter.com.
40. S. C. Jacobson and J. M. Ramsey, "Microchip structures for submillisecond electrophoresis," Anal. Chem., 70, 3476, 1998.
41. Z. D. Sandlin, M. S. Shou, J. G. Shackman, and R. T. Kennedy, "Microfluidic

electrophoresis chip coupled to microdialysis for in vivo monitoring of amino acid neurotransmitters." Anal. Chem., 77, 7702-7708, 2005.
42. N. A. Celllar and R. T. Kennedy, "A capillary-PDMS hybrid chip for separations-based sensing of neurotransmitters in vivo," Lab On A Chip, 6, 1205-1212, 2006.
43. M. T. Blom, "On-chip separation and sensing systems for hydrodynamic chromatography," Twente University Press, ISBN 9-036-51841-5, 2002.
44. P. Camilleri, "Capillary electrophoresis: theory and practice," 2nd edition, CRC Press Boca Raton, 1998.
45. R. F. Probstein, "Physicochemical hydrodynamics," 2nd edition, Wiley-Interscience, ISBN 0-471-45830-9, 2003.
46. F. P. Incropera and D. P. De Witt, "Introduction to heat transfer," 2nd edition, John Wiley & Sons, Inc., ISBN 0-471-51728-3, 1990.
47. T. Perez-Ruiz, C. Martinez-Lonano, A. Sanz, and E. Bravo, "Separation of fluorescein dyes by capillary electrophoresis using β-cyclodextrin," Chromatographia, 48, 263-267, 1998.
48. C. L. Ren and D. Li, "Electrokinetic sample transport in a microchannel with spatial electrical conductivity gradients," J. of Coll. and Int. Sci., 294, 482-491, 2006.
49. Warren J. Lyman, William F. Reehl and David H. Rosenblatt, "Handbook of Chemical Property Estimation Methods," American Chemical Society, 1982.
50. S. Kintzios, et al., "Study on the mechanism of Bioelectric Recognition Assay: evidence for immobilized cell membrane interactions with viral fragments." Biosensors and Bioelectronics, 20, 907-916, 2004.
51. A. D. Stroock and G. J. McGraw, "Investigation of the staggered herringbone mixer with a simple analytical model," Phil. Trans. R. Soc. A, 362, 971-986, 2004.
52. H. Chen and J. C. Meiners, "Topologic mixing on a microfluidic chip." Appl. Phys. Lett., 84, 2193, 2004.
53. Stephen C. Jacobson, Timothy E. McKnight, and J. Michael Ramsey, "Microfluidic Devices for Electrokinetically Driven Parallel and Serial Mixing," Anal. Chem., 71, 4455-4459, 1999.
54. Anson Hatch, et al, "A rapid diffusion immunoassay in a T-sensor," Nature Biotechnology, 19, 461-465, 2001.
55. Y. C. Wang, A. L. Stevens, and J. Han. "Million-fold preconcentration of proteins and peptides by nanofluidic filter," Anal. Chem. 77, 4293-4299, 2005.